W&M ScholarWorks

Dissertations, Theses, and Masters Projects

Theses, Dissertations, & Master Projects

Spring 2016

Molecular and Performance Properties of Poly(Amides & Imides) and the Use of Graphene Oxide Nano-Particles for Improvement

John-andrew Samuel Hocker
College of William and Mary, jshock@email.wm.edu

Follow this and additional works at: https://scholarworks.wm.edu/etd

Part of the Physical Sciences and Mathematics Commons

Recommended Citation

Hocker, John-andrew Samuel, "Molecular and Performance Properties of Poly(Amides & Imides) and the Use of Graphene Oxide Nano-Particles for Improvement" (2016). *Dissertations, Theses, and Masters Projects*. Paper 1477068376.
http://doi.org/10.21220/S2PK51

This Dissertation is brought to you for free and open access by the Theses, Dissertations, & Master Projects at W&M ScholarWorks. It has been accepted for inclusion in Dissertations, Theses, and Masters Projects by an authorized administrator of W&M ScholarWorks. For more information, please contact scholarworks@wm.edu.

Molecular and Performance Properties of Poly(amides & imides) and The Use of Graphene Oxide Nano-particles for Improvement

John-Andrew Samuel Hocker

Greenville, VA

M.S., Chemistry

B.S., Chemistry

A Dissertation presented to the Graduate Faculty
of the College of William and Mary in Candidacy for the Degree of
Doctor of Philosophy

Applied Science

The College of William and Mary
August 2016

© Copyright by John-Andrew Samuel Hocker 2016

APPROVAL PAGE

This Dissertation is submitted in partial fulfillment of
the requirements for the degree of

Doctor of Philosophy

John-Andrew Samuel Hocker

Approved by the Committee, July 2016

Committee Chair
Professor David E. Kranbuehl, Chemistry
The College of William and Mary

Professor Mark K. Hinders, Applied Science
The College of William and Mary

Professor Hannes C. Schniepp, Applied Science
The College of William and Mary

Professor John C. Poutsma, Chemistry
The College of William and Mary

Dr. Catharine C. Fay, Langley Research Center
NASA

Dr. Cheol Park, Langley Research Center
NASA

ABSTRACT

Macroscopic properties of polymers are innately related to their molecular structure and intermolecular properties. This dissertation demonstrates how the molecular structure, chain properties, and inter-molecular chain interactions can be used to explain and predict macro level performance properties, and how the addition of graphene oxide nanosheets enhances the performance properties of polyamide-11 (PA11) and polyimide through those same intermolecular interactions. Polyamides are frequently used in everyday life and are the preferred polymer in critical applications involving hydrocarbons. Chapter 3 describes the unexpected result that weak small organic acids at low concentrations hydrolyze a polyamide at rates approximately twice that of a water hydrochloric acid solution of the same pH at 100 ˚C and 120 ˚C under anaerobic conditions. Chapter 4 discusses how by varying the rate of molecular weight (M_m) degradation with small organic acids the correlated effects of M_m and crystallinity upon the ultimate strain of PA11 were decoupled. The result demonstrates the need for both crystallinity and molecular weight knowledge to monitor and predict the ductile to brittle transition and when embrittlement occurs. Chapter 5 explores the elevated resistance to hydrolytic degradation and molecular properties that a graphene oxide (GO) loaded PA11 has compared with neat PA11 at 100 and 120 ˚C. The decreased rate of degradation and resulting 50 % increased equilibrium molecular weight of PA11 was attributed to the highly asymmetric planar GO nano-sheets that inhibited the molecular mobility of water and the polymer chain. The crystallinity of the polymer matrix was similarly affected by a reduction in chain mobility during annealing due to the GO nanoparticles' chemistry and highly asymmetric nano-planar sheet structure. Chapter 6 extends the experimental work to effects on polyimides. GO and ODAGO (functionalized with 4-4' oxydianiline) are incorporated at 0.01 to 0.10 wt% into a polyimide (PI) made from 3,3'-benzophenonetetracarboxylic dianhydride (BTDA) and 4-4' oxydianiline (ODA). The performance properties of these two systems GO-PI and ODAGO-PI at extremely low GO concentrations of 1 part per 10,000 are comparable to previous results citing concentrations 10 times higher and displayed significantly greater improvement than unfunctionalized GO-PI films. The results suggest that the improved barrier properties are due a toruosity effect of the GO sheets and to a stabilizing effect of the flakes on the polymer matrix, where reduced mobility of the PI chain reduces diffusion through the polymer matrix. attenuated total reflectance fourier transform infrared spectroscopy, wide angle x-ray spectroscopy, raman and glass transition results support this view.

TABLE OF CONTENTS

Acknowledgements		ii
Dedications		iii
List of Tables		iv
List of Figures		vi
Chapter 1	Introduction	1
Chapter 2	Modeling and Instrumentation	13
Chapter 3	Polyamide hydrolysis accelerated by small weak organic acids	34
Chapter 4	The Ductile-Brittle Transition of Polyamide-11 as Determined by Molecular Weight and Crystallinity	63
Chapter 5	The Reduction of Hydrolytic Degradation in Polyamide-11 by the Addition of Graphene Oxide	96
Chapter 6	Enhancing Polyimide's Water Barrier Properties through Addition of Functionalized Graphene Oxide	158
Chapter 7	Conclusion and Future Directions	202
VITA		208

ACKNOWLEDGEMENTS

The author wishes to express acknowledgement and appreciation to Professor David E. Kranbuehl, under whose guidance this investigation was conducted; for his patience, support, and constructive criticism throughout the investigation. The author is also grateful to Professor Hannes C. Schniepp, Professor Mark K. Hinders, Professor John C. Poutsma, Dr. Catharine C. Fay and Dr. Cheol Park for their careful reading and critique of the manuscript.

Lydia Whitaker, Lianne Ashborne, and Rosario Fox for their administrative support.

For their collaboration, thoughts, discussion, help and support: Dr. Laura R. Dickinson, Dr. Arthur Jaeton Glover, Anne Kelly Rhudy, Gregory Ginsburg, Natalie Hudson-Smith, Patrick Smith, Yvonne Mack, Ryan Shintani, Charles Blevins, Jacob Lisi, HaeSeong Kim, Alyssa Pence, Megha Vipani, David Smith, Megan Gay, Yunwoo Noh, Aiden de Sena, Erin Hills, Chris Moad, William Kim, Sang Kim, Chris Komatsu, Andrew Morris, Min Seo, Kyle Overdeep, Ingrid Mielke-Maday.

This PhD is dedicated to my Family. To my beloved wife Lopamudra and all who supported me during this journey.

LIST OF TABLES

Table 3-1: Rate constants and equilibrium molecular weight for laboratory made PA11 aged in 1.05 ×10^{-2} M aqueous weak organic acid conditions; determined using the measured M_m over time and a non-linear least squares fit of the hydrolysis kinetic model Equation 2-12. 47

Table 3-2: Weight gain and acid concentration in neat PA11 aged at 100 ˚C in 1 M acid solutions, measured using gas chromatography, weight gain, and thermogravimetric analysis (TGA). 48

Table 3-3: The molarity of the aging acid solution versus the acid molarity of the distillate. The table reports the concentration of the acid within the PA11 matrix after 10 days at 100 ˚C, and the moles of acid and water respectively within the 2 mL injection aliquot of the distillate based on the GC results and the calibration of peak area to moles. 49

Table 3-4: Rate constants and equilibrium molecular weight for commercial Besno P40TLOS PA11 aged in various aqueous acid conditions; determined using the measured M_m over time and a non-linear least squares fit of the hydrolysis kinetic model Equation 2-12. 55

Table 3-5: Hansen solubility parameters. 56

Table 4-1: The input values and range limits that were used in a non-linear east squares fit of Equation 4-1 to the experimental data are listed. The fitted best fit values for each parameter are listed, with an R^2 of 0.82. 83

Table 4-2: Summary of key observations. 86

Table 4-3: Molecular weight (kDa), crystallinity (J/g) and ultimate strain (%) data collected for aging in water, acetic, and butanoic acid at 120 ˚C. 95

Table 5-1: Rate constants and M_{me} for GO-PA11 aged in water; determined using Equation 2-12 and a non-linear least squares fit. 109

Table 5-2: Integration values of DSC heat flow peaks from 140 ˚C to 200 ˚C for GO-PA11 and PA11, aged and unaged samples. The error margin is 2.5 J/g per measurement and peak integration. 116

Table 5-3: DSC peak temperatures for GO-PA11 and PA11, aged and unaged samples. The peak temperatures are accurate within 0.5 ˚C. 117

Table 5-4: DSC onset melting and formation temperatures for GO-PA11 and PA11, aged and unaged samples. The onset melting and formation temperatures are accurate within 0.5 ˚C. 118

LIST OF FIGURES

Figure 2-1: Base catalyzed amide hydrolysis elementary mechanism steps, pathway I and pathway II. 19

Figure 2-2: Acid catalyzed amide hydrolysis elementary mechanism steps. 19

Figure 2-3: Water assisted amide hydrolysis elementary mechanism steps. 19

Figure 2-4: Measured molecular weights of polyamide-11 during fractionated elution volumes using size exclusion chromatography multiple angle laser light scattering. 21

Figure 2-5: The molecular weight distribution of a polyamide-11 sample: the mass fraction of measured molecular weights of polyamide-11 from a fractionated SEC-MALLS measurement. 22

Figure 2-6: Attenuated total reflectance fourier transform infrared spectra of graphitic oxide and polyamide-11 (PA11). 24

Figure 2-7: Thermogravimetric behavior of a commercial polyamide-11 (PA11). The water content and plasticizer content are quantified by the mass reduction at 105 ˚C and 240˚C respectively. 26

Figure 2-8: DSC measured heat flow behavior of semi-crystalline PA11: a heat/cool/heat procedure. The melting of the crystalline regions, heat of fusion ΔH_{fus}, is observed in the heating ramps and the crystalline formation, heat of crystallization ΔH_c, is measured in the cooling ramp. 29

Figure 2-9: The glass transition temperature, T_g, for polyimide was measured on the DSC using a rapid heating ramp of 30 ˚C/min. 30

Figure 3-1: A plot of the Light Scattering measured M_m over time for PA-11 aged at 100 ˚C in small organic acid solutions.
■ water data; —— water fit.
◇ acetic data; —— acetic fit.
○ propanoic data; —— propanoic fit.
● butanoic data; —— butanoic fit. 45

Figure 3-2: A plot of the Light Scattering measured M_m over time for PA-11 aged at 120 ˚C in small organic acid solutions.
■ water data; —— water fit.
◇ acetic data; —— acetic fit.
○ propanoic data; —— propanoic fit.
● butanoic data; —— butanoic fit. 46

Figure 3-3: PA11 weight gain at 100 ˚C in a small organic acid. (■) Total mass percent gain measured using gravimetry versus acid concentrations. The percent content of (■) acid and (■) water measured in the distillate with gas chromatography. 50

Figure 3-4: Commercial plasticized PA-11 aged at 100 ˚C in various aqueous acid conditions. M_m data was measured using SEC-MALLS.
○ pH=7 water data; —— water fit.
□ pH=6.2 buffered acetic acid at 6.29 ×10^{-2} M data; —— buffered acetic acid fit.
◇ pH=4.2 CO_2 data; —— CO_2 fit.
◇ pH=2.9 HCl data; —— HCl fit.
▲ pH=2.98 acetic acid at 6.29 ×10^{-2} M data; —— acetic acid at 6.29 ×10^{-2} M fit. 54

Figure 4-1: Aging M_m over time for P40TLO PA11 in water, acetic and butanoic accelerated aging environments; color is the ultimate strain where red is ductile and blue is brittle. Averaged experimental data of X-water; O-acetic acid aged; and •-butanoic acid aged, and error bars are the standard deviation calculated from 3 or more data points. 72

Figure 4-2: Crystallinity over time, with ultimate strain color overlay where red is ductile and blue is brittle. Averaged experimental data of X-water; O-acetic acid aged; and •-butanoic acid aged, and error bars are the standard deviation calculated from 3 or more data points. 73

Figure 4-3: ΔH_{fus} as a function of the M_m during aging. Color is the ultimate strain where red is ductile and blue is brittle. Averaged experimental data of X-water; O-acetic acid aged; and •-butanoic acid aged, and error bars are the standard deviation calculated from 3 or more data points. 75

Figure 4-4: Ultimate strain as a function of molecular weight. Color is the crystallinity measured through ΔH_{fus} in J/g strain where high crystallinity and blue low crystallinity. Averaged experimental data of X-water; O-acetic acid aged; and •-butanoic acid aged, and error bars are the standard deviation calculated from 3 or more data points. 78

Figure 4-5: A closer look at the embrittlement region; color is the ultimate strain where red is ductile and blue is brittle. Averaged experimental data of X-water; O-acetic acid aged; and •-butanoic acid aged, and error bars are the standard deviation calculated from 3 or more data points. 80

Figure 4-6: Model predicted color coded ε for a given M_m and ΔH_{fus}. Averaged experimental data of X-water; O-acetic acid aged; and •-butanoic acid aged overlayed on the model predictions. Error bars are the standard deviation calculated from 3 or more data points. 84

Figure 4-7: 3-D plot: Model predicted color coded ε for a given M_m and ΔH_{fus}. Averaged experimental data of X-water; O-acetic acid aged; and •-butanoic acid aged fit to the model. Error bars are the standard deviation calculated from 3 or more data points. 85

Figure 5-1: Atomic force microscope height image (from GO-water dispersion) distributed on mica. 101

Figure 5-2: M_m of PA11 aging in water over time at 100 ˚C and 120 ˚C. M_{me} of 1-GO-PA11 was approximately 10 kDa higher than PA11 and 5-GO-PA11 at 100 ˚C and 120 ˚C aging temperatures, respectively. 108

Figure 5-3: 60 x 60 μm transmission optical microscopy images of PA11 bright field (6a), cross-polarized (6b), 1-GO-PA11 bright field (6c), and 5-GO-PA11 bright field (6d). 110

Figure 5-4: Elementary chemical mechanism of resonance stabilization of the amide bond. 112

Figure 5-5: Base catalyzed elementary chemical mechanism of amide hydrolysis. 112

Figure 5-6: Acid Catalyzed elementary chemical mechanism of amide hydrolysis. 112

Figure 5-7: Elementary chemical mechanism for water assisted hydrolysis of the amide bond. 112

Figure 5-8: DSC scans for unaged, 100 ˚C, and 120 ˚C 80-90 days aged PA11 unloaded, 1-GO-PA11, and 5-GO-PA11. The DSC test was a standard heat, cool, heat sequence at 3 ˚C/min between 40 and 220 ˚C. The 3 columns from left to right are 1st heat ramp from 40 ˚C to 220 ˚C, followed by a cool ramp to 40 ˚C, and a 2nd heat ramp to 220 ˚C. The rows top to bottom are unaged, 100 ˚C, and 120 ˚C aged samples. 115

Figure 5-9: Attenuated total reflectance fourier tranform infrared spectra of PA11 & 1-GO-PA11, and aged PA11 & aged 1-GO-PA11. 123

Figure 5-10: The peak widths centered at 3305 cm^{-1} for PA11, 1-GO-PA11, and 5-GO-PA11 and grouped by unaged and aged at 120 ˚C for 90 days. 125

Figure 5-11: 60 x 60 μm cross polarized transmission optical microscopy images of 100 ˚C and 120 ˚C aged PA11 and 1-GO-PA11. 127

Figure 5-12: The deconvoluted peak heights centered at 1635 cm^{-1} are grouped based on material; PA11, 1-GO-PA11, and 5-GO-PA11; then by unaged and aged at 120 ˚C for 90 and 120 days. 146

Figure 5-13: The deconvoluted peak heights centered at 1654 cm^{-1} are grouped based on material; PA11, 1-GO-PA11, and 5-GO-PA11; then by unaged and aged at 120 ˚C for 90 and 120 days. 147

Figure 5-14: The deconvoluted peak heights centered at 1684 cm^{-1} are grouped based on material; PA11, 1-GO-PA11, and 5-GO-PA11; then by unaged and aged at 120 ˚C for 90 and 120 days. 148

Figure 5-15: PA11, ATR-FTIR spectra between 1590 and 1800 cm^{-1} de-convoluted using Gaussian peak shapes at 1635, 1654, and 1684 cm^{-1}. 149

Figure 5-16: PA11 aged 90 days at 120 ˚C, ATR-FTIR spectra between 1590 and 1800 cm^{-1} de-convoluted using Gaussian peak shapes at 1635, 1654, and 1684 cm^{-1}. 150

Figure 5-17: PA11 aged 120 days at 120 ˚C, ATR-FTIR spectra between 1590 and 1800 cm^{-1} de-convoluted using Gaussian peak shapes at 1635, 1654, and 1684 cm^{-1}. 151

Figure 5-18: 1-GO-PA11, ATR-FTIR spectra between 1590 and 1800 cm^{-1} de-convoluted using Gaussian peak shapes at 1635, 1654, and 1684 cm^{-1}. 152

Figure 5-19: 1-GO-PA11 aged for 90 days at 120 ˚C, ATR-FTIR spectra between 1590 and 1800 cm^{-1} de-convoluted using Gaussian peak shapes at 1635, 1654, and 1684 cm^{-1}. 153

Figure 5-20: 1-GO-PA11 aged 120 days at 120 ˚C, ATR-FTIR spectra between 1590 and 1800 cm^{-1} de-convoluted using Gaussian peak shapes at 1635, 1654, and 1684 cm^{-1}. 154

Figure 5-21: 5-GO-PA11, ATR-FTIR spectra between 1590 and 1800 cm^{-1} de-convoluted using Gaussian peak shapes at 1635, 1654, and 1684 cm^{-1}. 155

Figure 5-22: 5-GO-PA11 aged 90 days at 120 ˚C, ATR-FTIR spectra between 1590 and 1800 cm^{-1} de-convoluted using Gaussian peak shapes at 1635, 1654, and 1684 cm^{-1}. 156

Figure 5-23: 5-GO-PA11 aged 120 days at 120 ˚C, ATR-FTIR spectra between 1590 and 1800 cm^{-1} de-convoluted using Gaussian peak shapes at 1635, 1654, and 1684 cm^{-1}. 157

Figure 6-1: ATR-FTIR normalized absorbance spectra of ODA, ODA-GO and GO. 169

Figure 6-2: Atomic force microscope images and profiles of graphene oxide (GO) and ODA functionalized graphene oxide (ODAGO). 172

Figure 6-3: Raman Spectra of GO and ODAGO. 174

Figure 6-4: Water vapor permeability for unloaded PI, GO-PI, and ODAGO-PI films at 23 ˚C and 70% humidity. 176

Figure 6-5: Calculated aspect ratio of the nanoparticles in the PI nanocomposites where the dashed line is for a value of 1000, an average aspect ratio for GO. 178

Figure 6-6: Glass transition temperatures (Tg) of PI, GO-PI, and ODAGO-PI measured using differential scanning calorimetry. 181

Figure 6-7: Wide anlge X-ray Diffraction, WAXRD, spectra of GO, GO-PI, and ODAGO-PI. 182

Figure 6-8: Fourier Transform Infrared Spectra of polyimide (PI); graphene oxide loaded PI (GO-PI) at 0.1 wt%; and ODA functionalized graphene oxide loaded PI (ODAGO-PI) at 0.1 wt%. 184

Figure 6-9: Percent water gain after 24 hours immersion in DI water for ODA-GO-PI, GO-PI and neat PI. 187

Figure 6-10: Young's modulus of ODA-GO-PI, GO-PI and neat PI films. 189

Chapter 1

Introduction

Theme: Understanding chemical molecular interactions and their relationship to macroscopic performance properties of polymer materials

Macroscopic material properties: strength, toughness, permeability, conductivity, color, optical transparency are all widely understood to be influenced by the material's molecular properties. An example is the hardness of a diamond being an expression of its highly ordered, chemically stable, covalently bound carbon crystal structure – a ceramic. Conversely, the toughness and tensile properties of polymers are the result of molecular chain entanglements and their intermolecular interactions[1-4].

Staudinger [5] proposed a macromolecular theory justifying the existence of polymer molecules through observations of polystyrene. However, an understanding of polymers at the molecular level was not widely accepted until Carothers produced the first synthetic polymer in 1935, polyamide-6-6, later commercialized as nylon by DuPont. Polyamides, in all their variety, remain the most widely used polymers in the world today[2, 6, 7].

Polyamides are a class of polymers named for their characteristic amide

bonds that link the monomer chain units. Oversimplified, polyamides would be any polymer that has a $R_1R_2N\text{-}COR_3$ bond at chain linkages, and would include several classes of polymers: polypeptides, polyurethanes, polyimides, and polyamides. Kapton™ is a popular polyimide, and Nylon™ and Kevlar™ are examples of commercial polyamides. The amide bond $R_1R_2N\text{-}COR_3$ is a polar bond that can hydrogen bond with other amide bonds to form aligned, stiff, and thermally stable impermeable crystalline domains. Crystallinity in a polyamide happens spontaneously in aliphatic polyamides such as polyamide-11 (PA11). With both amorphous and crystalline regions, polyamides are uniquely well suited for applications where toughness, thermal and chemical stability are important. Polyamides and polymers in general can be chemically designed and customized to solve unique material performance property challenges.

With the need to transport crude oil from the ocean floor, a major issue faced by the oil companies was the design of flexible risers to transport crude from the sea floor to offshore platforms. In 1957 the French government funded research to determine what material would best contain the crude in flexible pipelines. The polymer PA11, obtained from the castor bean, was chosen. To contain crude oil and act as the pipeline pressure sheath, the polymer PA11 had to be chemically resistant, strong, and tough[8].

While in use, it was discovered that over time PA11 would become brittle and the pipelines could rupture. Sudden failures and oil spills propelled a well-funded interest to predict and avoid pipeline failure. This led to a worldwide

study of PA11's mechanical and hydrolysis properties during use. Measurement of mechanical properties did not forecast failure as it was sudden and without symptoms. However, with a focus on how molecular properties affect the mechanical properties, world-wide laboratory studies were conducted to investigate the behavior of PA-11 under simulated offshore field conditions. The average molecular weight, and average length of the polymer chains, were determined to be the fundamental and critical molecular property to be monitored and characterized to predict the approach of the onset of PA11 embrittlement and thereby avoid flexible riser failure[9].

For applications such as the transport of crude oil, the mechanical, permeability, and swelling properties are all of interest. Mechanical properties include tensile modulus, ultimate strength, ultimate strain, hardness and wear resistance. The macroscopic performance criteria are dependent upon the particular application. Some applications require high thermal stability. PA11 is well suited at temperatures of 60 ˚C to 90 ˚C. A higher temperature stability would require a different kind of amide, such as the ODA-BTDA polyimide or at 120 ˚C, a polymer such as poly vinyl difluoride.

Polyimides (PI) are a family of high-performance polymers that derive excellent mechanical strength, thermal resistance, and chemical resistance from their stable and rigid imide bonds. Their stiffness starts as an amide bond that is then further reacted to form an imide ring. Two C=O groups attach to the nitrogen to form an imide group in place of one in an amide. Polyimides can be found in a

wide array of industrial applications such as electric motors, jet engine blades, aircraft wire, and molded pistons and seals. Recent aerospace applications of PI films include the Mars Explorers Curiosity and Spirit [10], the European Space Agency's Rosetta space probe [11], and the sun shield of NASA's James Webb Space Telescope [12]. In all of the PI applications, efficiency can be improved by using less material to effect the same utility. Additionally, in some cases, the use of PI can enable new applications or technologies in extreme environments, e.g. outer space. In a global effort to make better and enabling materials, many different fillers and nano-fillers have been researched for polyimide and polyamide nanocomposites. In recent years, graphene has been explored as a nano-filler to make nanocomposites with new and more advantageous properties.

A wide interest in graphene's exceptional strength has revitalized research involving the analogous compound graphene oxide (GO). GO has nearly the same strength and barrier properties as pristine graphene, given the very high aspect ratio planar honeycomb structure. GO has the same honeycomb structure as graphene but with oxygen-containing functional groups on the surface of the planar carbon. These oxygen containing functional groups are ketones, 6-membered lactol rings, alcohols, epoxides and hydroxyl groups[13]. As a result, GO is a polar hydrophilic material compared to graphene, which is nonpolar and hydrophobic. GO, unlike graphene, can be dispersed into water and solvents[14] commonly used in polymer precursor resins or mixtures to create GO-polymer nanocomposites. Also, the oxide groups on the GO surface can be reacted with

different chemical groups for improved polymer nanocomposite performance properties.

By combining several molecular measurement techniques, the molecular behavior of a polymer, the effect of additives such as GO, and the chemistry of the environment can be characterized. Molecular measurements can be correlated to the macroscopic performance properties to identify molecular measurements to be monitored for predicting changes in macroscopic performance properties. As an example, the chemistry of polymer chains and their intermolecular interactions with each other and fillers such as GO can be probed with infrared light: fourier transform infrared spectroscopy (FTIR). FTIR can determine the presence of functional groups and resolve the relative intensities for quantification. Shifts in the FTIR peak positions reflect intermolecular interactions between functional groups within the material, such as hydrogen bonding, which affects polymer chain mobility and in turn water vapor permeability.

The two polymers that are studied in this dissertation are polyamide-11 and a 4,4-oxidianiline and 3,3'-benzophenonetetra-carboxylic polymide. These two linear polymers when polymerized form a distribution of chain lengths where each polymer exhibits differing degrees of entanglement and crystallinity. Size exclusion chromatography (SEC) can be used to measure the distribution of molecular chain lengths. Multi-anlge laser light scattering (MALLS) can directly measure the molecular weight within the distribution. Thereby SEC-MALLS when combined determines the distribution in the chain lengths as well as the number

and mass average molecular weight (M_n & M_m) of the distribution.

Hydrolytic degradation of the amide bond leads to lower molecular weights. Hydrolysis is the process by which water attaches to the amide bond to chemically break the bond. A competing reaction is polymerization where amide bonds are formed through condensation, Equation 2-1. Equation 2-1 is an equilibrium equation where the steady state chemistry is determined by the environment. The rate of chain scission is denoted by a hydrolysis rate constant k_H, and the rate of re-polymerization is denoted k_P. The reaction favors k_H or k_P by changes in the thermal and chemical environment, or by adding a catalyst.

There are three mechanisms for hydrolysis of an amide bond: base catalyzed Figure 2-1, acid catalyzed Figure 2-2, and water assisted Figure 2-3. In an acidic environment, an acid will catalyze the amide hydrolysis reaction and the activation energy of hydrolysis is reduced[15-17]. Theoretically, the rate of acid catalyzed amide hydrolysis is a function of the water and the environmental pH.

Earlier in our group, Glover [18] documented that organic acids such as acetic acid found in crude production water could lead to increased molecular weight degradation during accelerated aging tests of PA11. Chapter 3 describes a series of experiments that show the unexpected result that weak small organic acids at low concentrations hydrolyze PA11 at rates approximately twice that of a water HCl solution of the same pH. The study was done in an anaerobic aqueous environment to avoid oxidation and so the molecular weight degradation occurred

exclusively through hydrolysis reactions. Chapter 3 demonstrates that the diffusion of the acid into the polymer is the molecular basis for the unexpectedly accelerated molecular weight reduction and accelerated reduction in mechanical properties. Chapter 3 reports results on the hydrolysis of polyamide-11 polymerized from aminoundecanoic acid, both neat and a commercial plasticized composition, placed in water at 100 ˚C and 120 ˚C under anaerobic conditions in high pressure glass tubes. As a result of this work, it is evident that knowledge of the acid molecular diffusion and solubility in the polymer is more important than the environmental pH for predicting degradation of polyamide-11's molecular weight and its service lifetimes. This work has resulted in an ongoing joint industry investigation of acetic acid in oil fields throughout the world.

The performance properties of a polymer are directly related to other molecular properties of the polymer beyond the critical chain length. Fundamental molecular relationships and performance properties can be difficult to characterize as molecular properties are often inter-related with one another. For example, in PA11 the molecular weight and crystallinity content are inversely proportional: when polymerized a higher molecular weight has a smaller crystallinity, and a lower molecular weight has a higher crystallinity.

Since 2003, the mass average molecular weight of approximately 35 kDa has been considered to be the onset molecular weight for the ductile-brittle phase transition, and the safe use criteria for PA11 lined deep sea flexible risers[9, 19]. Chapter 4 illuminates this inter-relationship between molecular crystallinity and

molecular weight in PA11, and the inter-related joint influence on the macroscopic ductility. This work shows that there is a critical crystallinity content of 35% (66 $^{J}/_{g}$) that determines the M_m for the onset of the ductile-brittle transition. The M_m has a large effect on the decreasing ductility with increasing crystallinity once the critical crystallinity of 66 $^{J}/_{g}$ is achieved.

To improve PA11's resistance to hydrolytic degradation, Chapter 5 describes the incorporation of graphene oxide (GO) into PA11 via in-situ polymerization. The chapter describes why at the molecular level, the GO-PA11 nanocomposite displays significantly improved resistance to hydrolytic degradation. The decreased rate of degradation and resulting 50 % increase in equilibrium molecular weight of PA11 was attributed to the highly asymmetric planar GO nano-sheets that inhibited the molecular mobility of water and the polymer chain. The crystallinity of the polymer matrix was similarly affected by a reduction in mobility during annealing due to the GO nanoparticles' chemistry and highly asymmetric nano-planar sheet structure.

GO's effect on chain mobility is further described by the results in Chapter 6, where polyimide is combined with GO at concentrations of 0.01 to 0.10 weight percent (wt%). The performance properties of polyimide (PI), made from 3,3'-benzophenonetetra¬carboxylic dianhydride (BTDA) and 4-4' oxydianiline (ODA), were strongly affected at extremely low GO and functionalized GO concentrations. The improved barrier properties of the polyimide nanocomposites observed for the GO and much more so for the functionalized GO are attributed

to tortuosity and a stabilizing effect on the polymer matrix of the chemical groups on the surface of the GO sheets. The resulting decrease in the mobility of the PI chain reduced water diffusion through the polymer matrix. ATR-FTIR, WAXS, Raman and Tg results support this molecular understanding.

Macroscopic properties of polymers and in general all types of materials are innately related to their molecular structure and intermolecular properties. This dissertation offers scientific evidence on how the molecular structure, chain properties, and inter-molecular chain interactions within PA11 can be used to explain and predict improved macro level performance properties; and how the addition of graphene oxide nanosheets enhances the performance properties of PA11 and polyimide(ODA-BTDA) through those same intermolecular interactions.

1.1 References

[1_1] ODIAN, G. 2004. Principles of Polymerization, Hoboken, New Jersey, John Wiley & Sons, Inc.

[1_2] COWIE, J. M. G. & ARRIGHI, V. 2007. Polymers: Chemistry and Physics of Modern Materials, Boca Raton, FL, CRC Press.

[1_3] WELTER, J., KIM, S., SANTOR, K. & MALINOWSKI, S. (eds.) 2008. Fundamentals of Materials Science and Engineering, Hoboken, NJ: John Wiley & Sons.

[1_4] KUMAR, A. & GUPTA, R. K. 2011. Fundamentals of Polymer Engineering. 1-712.

[1_5] STAUDINGER, H. 1920. Über Polymerisation. Berichte der deutschen chemischen Gesellschaft (A and B Series), 53, 1073-1085.

[1_6] FLORY, P. J. & FLORY, J. 1936. Molecular Size Distribution in Linear Condensation Polymers 1. Journal of the American Chemical Society, 58, 1877-1885.

[1_7] RAPOLU, S. 2010. The Future of the Offshore Drilling Industry to 2015 - Market Analysis, Capital Expenditure and Competitive Landscape. 1-4.

[1_8] LANGE, H., BERGE, S., ROGNE, T. & GLOMSAKER, T. 2004. Material Selection in the Offshore Industry. SINTEF Materials and Chemistry.

1404778145 ed.: MARINTEK.

[1_9] API 2003. Technical Report 17TR2, The Ageing of PA-11 in Flexible Pipes. Washington, DC: American Petroleum Institute.

[1_10] DUPONT 2015a. Electronic Materials Go to Mars and Beyond. DuPont Electronic Materials.

[1_11] DUPONT 2015b. Kapton Plays Important Role on Rosetta Mission 2015.

[1_12] DUPONT 2013. NASA's Webb Telescope Sunshield made with DuPont Kapton polyimide film.

[1_13] DREYER, D. R., PARK, S., BIELAWSKI, C. W. & RUOFF, R. S. 2010. The chemistry of graphene oxide. Chemical Society Reviews, 39, 228-240.

[1_14] KIM, H., ABDALA, A. A. & MACOSKO, C. W. 2010. Graphene/Polymer Nanocomposites. Macromolecules, 43, 6515-6530.

[1_15] ZAHN, D. 2003. Theoretical study of the mechanisms of acid-catalyzed amide hydrolysis in aqueous solution. Journal of Physical Chemistry B, 107, 12303-12306.

[1_16] ZAHN, D. 2004b. On the Role of Water in Amide Hydrolysis. European Journal of Organic Chemistry, 2004, 4020-4023.

[1_17] ZAHN, D. 2004a. Car-Parrinello molecular dynamics simulation of base-

catalyzed amide hydrolysis in aqueous solution. Chemical Physics Letters, 383, 134-137.

[1_18] GLOVER, A. J. M. 2011. Characterization of PA-11 Flexible Pipe Liner Aging in the Laboratory and in Field Environments Throughout the World. Doctor of Philosophy Dissertation, The College of William and Mary.

[1_19] MEYER, A., JONES, N., LIN, Y. & KRANBUEHL, D. 2002. Characterizing and Modeling the Hydrolysis of Polyamide-11 in a pH 7 Water Environment. Macromolecules, 35, 2784-2798.

Chapter 2

Modeling and Instrumentation

The hydrolysis of polyamide bonds is a central topic for chapters Chapter 3, 4, and 5. The hydrolysis model used to characterize the hydrolysis process over time for polyamide-11 (PA11) is described here. The base catalyzed, acid catalyzed, and water assisted mechanisms for the amide bond hydrolysis are reviewed for background and discussions in Chapters 3 - 5. Three in-line size exclusion chromatography high performace liquid columns are paired with a multiple angle laser light scattering detector and used to measure the molecular weight of the PA11 material samples characterized in Chapters 3 - 5. Infrared spectroscopy and its use for polymer characterization is reviewed and introduced for Chapters 5 and 6. The thermal characterization techniques of thermo-gravimetric analysis and differential scanning calorimetry are introduced and used for analysis in Chapters 3 - 6.

2.1 Amide Bond Hydrolysis: Modeling via Time Dependent Mass Average Molecular Weight

We characterized the equilibrium molecular weight (M_{me}), pseudo-hydrolysis (k'_H), and solid state polymerization (k_P) rate constants during accelerated molecular weight degradation by fitting a mathematical model of amide hydrolysis to the measured M_m per aging time. The model was previously published and is derived from the condensation-hydrolysis kinetics described on page 15 by the chemical and kinetic Equation 2-2 and the associated first order ordinary differential Equation 2-9 [1-3]. The values k'_H and k_P, which are used to fit the changing values of molecular weight with time, reflect the composition of the aqueous aging environment and its effect on the hydrolysis process.

Using the steady state approximation at equilibrium Equation 2-3, assuming the concentration of water being constant in Equation 2-8, solving the ordinary differential Equation 2-11, making equivalent substitutions Equation 2-12, and rearranging the result, the hydrolysis degradation model is obtained in terms of the average number of amide bonds (a) over time, Equation 2-12. The number of amide bonds is directly proportional to the mass average molecular weight (M_m) over time, Equation 2-7.

Using Equation 2-7 to convert the measured M_m over time to the number os amide bons (a), the model, Equation 2-12, is fit to the data using nonlinear least squares to determine both the M_{me} and k'_H. In turn, using Equation 2-1 and M_{me} and

k'_H from the best fit results the re-polymerization rate constant k_P is calculated, where a_t is the average number of amide bonds at time t. Subscript $_0$ refers to the starting value, $_e$ refers to the equilibrium value, and $_t$ refers to the value per time t.

Equation 2-1:

$$R'NH_2 + RCO_2H \underset{k_H}{\overset{k_P}{\rightleftharpoons}} R'NHCOR + H_2O$$

Equation 2-2:

$$-\frac{d(R'NH_2)}{dt} = -\frac{d(RCO_2H)}{dt} = k_P[R'NH_2][RCO_2H] - k_H[R'NHCOR][H_2O$$

Equation 2-3:

$$0 = k_P[R'NH_2]_e[RCO_2H]_e - k'_H[R'NHCOR]_e[H_2O]_e$$

Equation 2-4:

$$x = [R'NH_2] = [RCO_2H]$$

Equation 2-5:

$$a = [R'NHCOR] = \frac{\overline{M}_m}{2 \cdot M_0} - 1$$

Equation 2-6:

$$x = a_0 - a$$

Equation 2-7:

$$a = \frac{\overline{M}_m}{2 \cdot M_0} - 1$$

Equation 2-8:

$$k'_H = k_H \cdot [H_2O]$$

Equation 2-9:

$$\frac{dx}{dt} = k'_H (a_0 - x_e) - k_P \cdot x^2$$

Equation 2-10:

$$k_P = \frac{k'_H (a_0 - x_e)}{x_e^{\,2}}$$

Equation 2-11:

$$k'_H\, t = \frac{x_e}{2a_0 - x_e} \cdot \ln \frac{a_0\, x_e + x(a_0 - x_e)}{a_0(x_e - x)}$$

Equation 2-12:

$$a_t = \frac{a_0^{\,2} + a_0\, a_e\, e^{\frac{a_0 + a_e}{a_0 - a_e} t\, k'_H}}{a_e + a_0\, e^{\frac{a_0 + a_e}{a_0 - a_e} t\, k'_H}}$$

2.2 Amide Bond Hydrolysis: Mechanism and Elementary Reaction Steps

Equation 2-1 shows the essence of amide hydrolysis. To elaborate, three chemical mechanisms have been identified for amide bond hydrolysis: base catalyzed[4-8], acid catalyzed[9-12], and water assisted[13, 14]. The activation energies have been determined to be 21, 31, and 99 kJ/mol for the base, acid, and water mechanisms of amide hydrolysis respectively[15]. And computationally, Zahn [13] found the activation energies to be 66, 78, and 147 kJ/mol. Thus, it can be understood that given equivalent concentrations of OH^- and H^+, the base catalyzed pathway is favored; and the water assisted hydrolysis of an amide bond is the least favored pathway.

The base catalyzed hydrolysis elementary reaction steps, mechanism Pathway I and Pathway II are shown in Figure 2-1, page 19. Zahn [4] computationally studied the mechanism of base catalyzed hydrolysis of the amide bond, and found that the Pathway II is favored. Zahn [4] found that no proton transfer reaction led to the simultaneous protonation of the amide nitrogen and deprotonation of the hydroxyl group. The amide anion is a poorer leaving group than an alkoxide ion, and in the base catalyzed hydrolysis, the proton transfer to the amide anion is considered the rate limiting step[16, 17].

The four step acid catalyzed hydrolysis mechanism is shown in Figure 2-2. The first step is the protonation of the carboxylic oxygen of the amide bond. Zahn

[18] found in a computational study that the second step, nucleophilic attack of a water molecule to the carbon atom of the amide group, is the rate determining step. The third step is the intermediate de-protonation of the carboxylic oxygen and protonation of the amide nitrogen, quickly followed by the dissociation of the protonated amine and the carboxylic acid.

The water assisted hydrolysis mechanism is shown in Figure 2-3. The water assisted mechanism involves two water molecules that act in a concerted process and utilize a Grotthuss mechanism of proton hopping. The first step, and rate determining step, is the nucleophilic attack of the amide carbon and simultaneous protonation of the amide nitrogen[13].

Pathway I

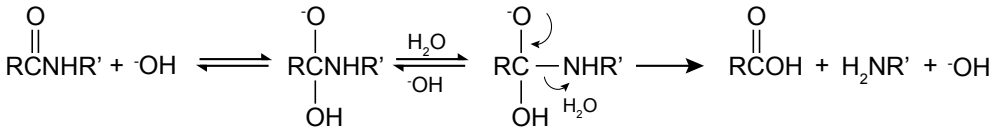

Pathway II

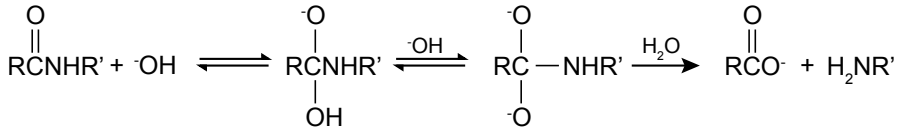

Figure 2-1: Base catalyzed amide hydrolysis elementary mechanism steps, pathway I and pathway II.

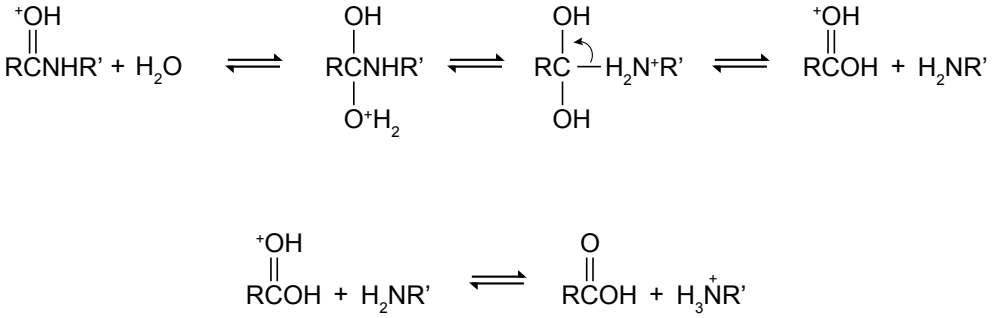

Figure 2-2: Acid catalyzed amide hydrolysis elementary mechanism steps.

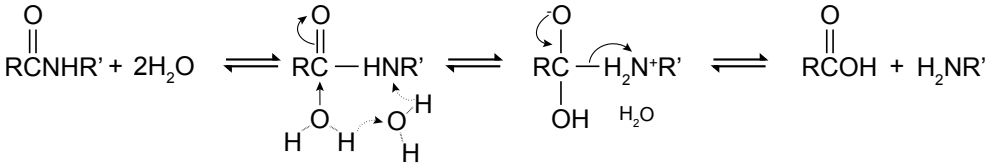

Figure 2-3: Water assisted amide hydrolysis elementary mechanism steps.

2.3 Size-Exclusion-Chromatography paired with Multiple Angle Laser Light Scattering

Light scattering is a primary method to measure the molecular weight of a polymer in solution[19]. The system used for this work has multiple in-line sized exclusion chromatography HPLC Shodex columns (HFIP-LG, HFIP-805, and HFIP-803) with packing beads composed of a polystyrenedivinyl benzene copolymer paired with a Wyatt miniDAWN light scattering and Wyatt Optilab 803 dynamic refractive index detector. The size exclusion chromatography columns fractionate the polymer molecule solution; the refractive index and the light scattering detectors were used to measure the molecular weight at each fraction, Figure 2-4 and Figure 2-5. The miniDAWN has a laser wavelength of 690 nm and 3 detection angles of 45˚, 90˚, and 135˚. A measured and literature verified $^{dn}/_{dc}$ of 0.235 determined the concentration of the polyamide-11 at each fraction. The solvent used to dissolve the polymer samples was 1,1,1,3,3,3-hexafluoro-2-propanol (HFIP) doped with 0.05 M Potassium Tri-Fluoroacetate (KTFA) salt to remove nylon agglomerations [24]. The solvent was degassed in the pump reservoir via constant Helium sparge under atmospheric pressure. The polymer sample solutions were 2 $^{mg}/_{mL}$ and 100 mL aliquots of a sample solution were injected.

The SEC-light scattering M_m measurements in this work have a 6% instrumental error. The error was determined by the standard deviation divided by the mean for six consecutive M_m measurements on a single solution of unaged laboratory-made PA-11.

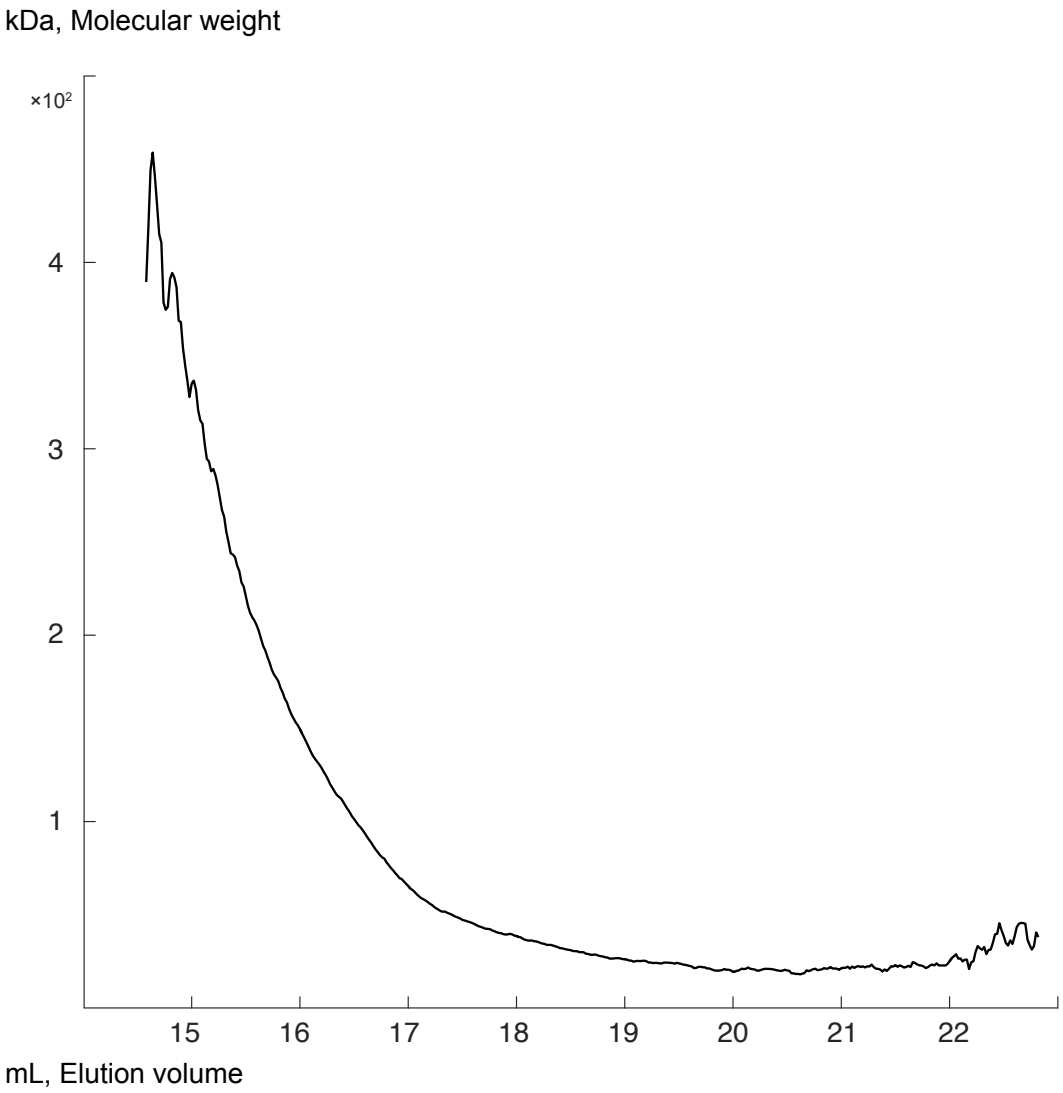

Figure 2-4: Measured molecular weights of polyamide-11 during fractionated elution volumes using size exclusion chromatography multiple angle laser light scattering.

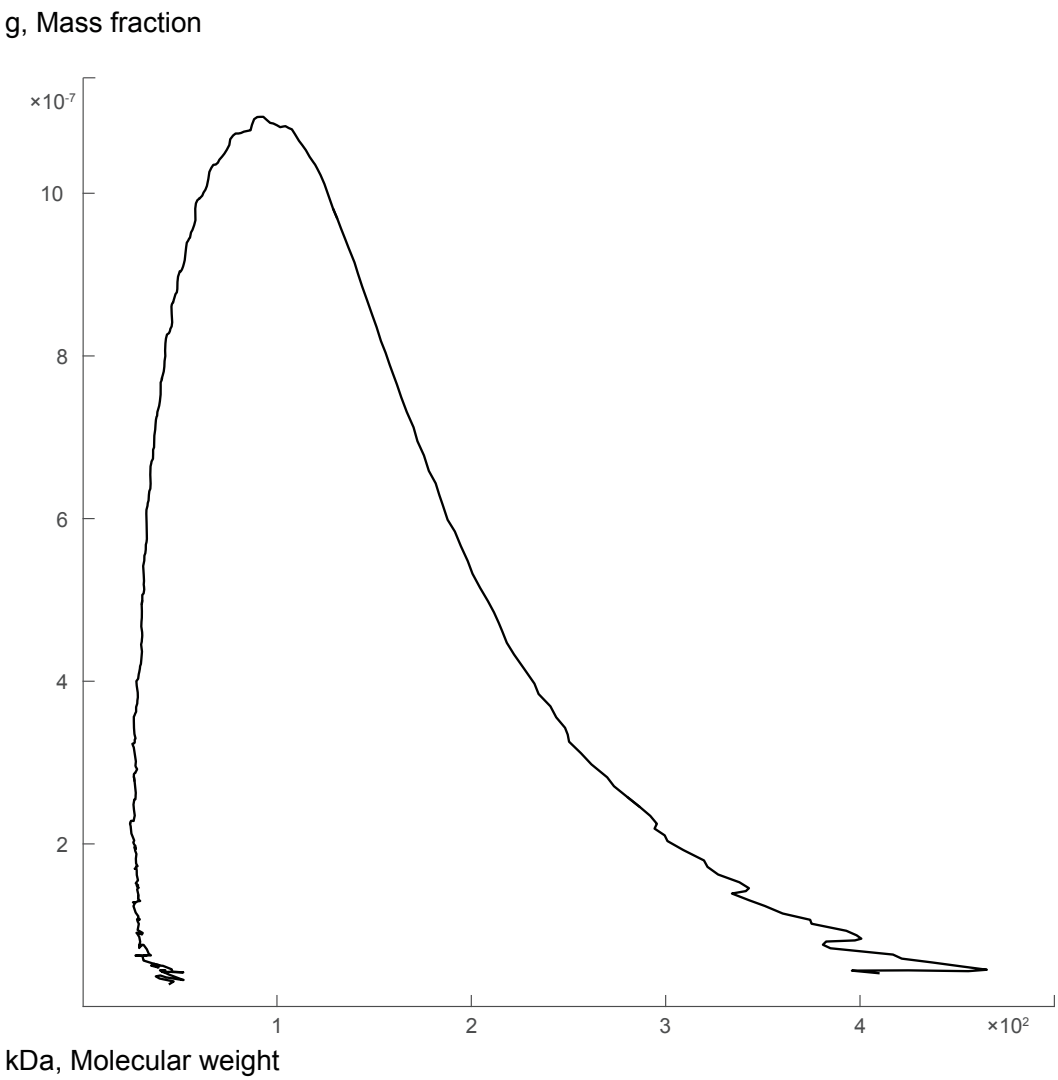

Figure 2-5: The molecular weight distribution of a polyamide-11 sample: the mass fraction of measured molecular weights of polyamide-11 from a fractionated SEC-MALLS measurement.

2.4 Infrared Spectroscopy

Attenuated Total Reflectance Fourier Transform Infrared Spectroscopy (ATR-FTIR) was included in several chapters to describe the chemical functional groups and intermolecular interactions. Spectra were taken from 600 to 4000 cm^{-1} and obtained using the IR Tracer-100 Shimadzu FTIR's MIRacle 10 Single Reflectance ATR accessory. Figure 2-6 shows ATR-FTIR spectra of pristine graphitic oxide and PA11, respectively.

The infrared spectrum of light has an appropriate energy to interact with the bonding vibrations and stretches in organic molecular structures, such as organic polymers or graphene oxide. Infrared spectroscopy is the measure of the infrared light's absorption due to changes in the vibrational energy level of a bond. The frequency of absorption provides information through peak position, intensity, width, and shapes towards identifying the type of functional group and its location[20].

Herein, infrared spectra are reported in absorbance versus wavenumber. The wavenumber is inverse wavelength, which is directly proportional to the energy through Planck's constant. A higher wavenumber is a lower wavelength, higher frequency, and higher energy, a blue shift. A lower wavenumber is a higher wavelength, lower frequency, and lower energy, a red shift. At a wavenumber, or peak position, the absorbance is the energy that is absorbed by the matter material the infrared light is reflected or transmitted[20].

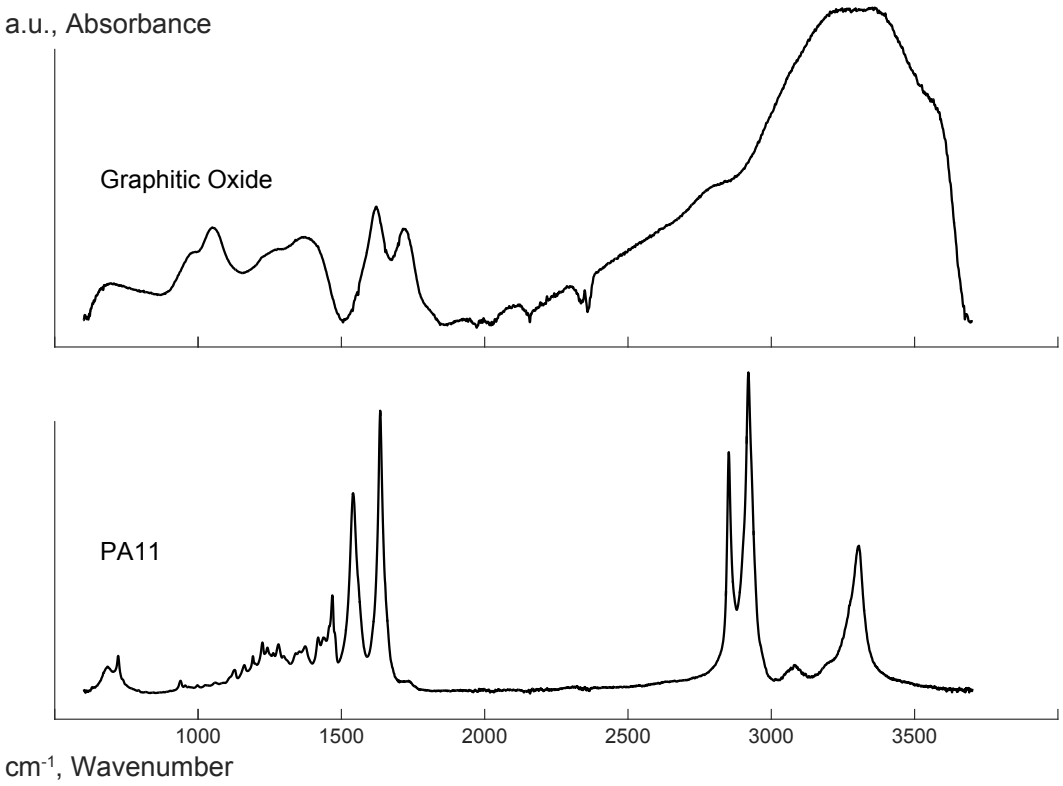

Figure 2-6: Attenuated total reflectance fourier transform infrared spectra of graphitic oxide and polyamide-11 (PA11).

2.5 Thermo-gravimetric Analysis

Thermo-gravimetric analysis (TGA) is a technique that monitors the mass change of a material as a function of temperature. A TGA has many applications. The work herein uses the TGA to determine volatile content versus temperature for various polymer samples, as well as the thermal stability of graphene oxide and functionalized graphene oxide.

The instrument used for the experiments presented here was a model Q500 from TA Instruments. The model Q500 features a programmable furnace, a max temperature of 1000 ˚C, mass changes to the nearest microgram, and a programmable gas flow sample chamber. Nitrogen gas is constantly purging the environment so to prevent oxidation effects while heating the sample. If the polymer samples were to be exposed to oxygen while in the melted state, a reduction in mass would occur due to oxidation: CO_2 and H_2O evolution.

TGA sampling of polymer uses slices thinner than 1 mm in a pyrolysis-cleaned platinum pan. The TGA is done under nitrogen gas. Figure 2-7 shows a typical PA11 volatile content thermogravimetric analysis.

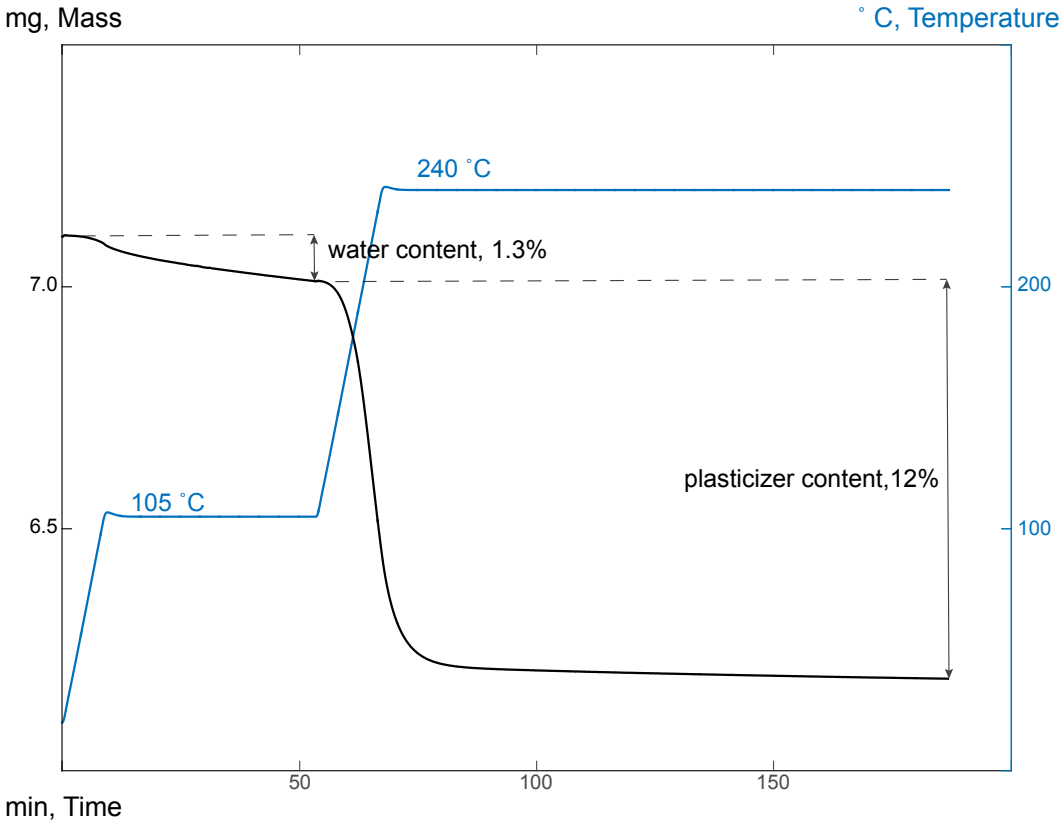

Figure 2-7: Thermogravimetric behavior of a commercial polyamide-11 (PA11). The water content and plasticizer content are quantified by the mass reduction at 105 ˚C and 240˚C respectively.

2.6 Differential Scanning Calorimetry

Like a TGA, the Differential Scanning Calorimeter (DSC) is a thermal characterization instrument. A DSC measures the heat absorption difference between air and sample material, enthalpy changes as a result of changes in physical state or chemical reactions in the material. A DSC is capable of investigating several material and chemical properties. In this dissertation, the heat of fusion, heat of formation, peak positions, and glass transition temperature are used to characterize the polymers and polymer nanocomposites. The DSC 2920 Modulated, made by TA Instruments with a maximum temperature of 350 ˚C was used to measure enthalpy for polymer and polymer nanocomposite samples.

A sample mass of 5-10 mg was used and measured to within ± 0.1 mg on an analytical balance. The sample material was loaded into a TA Instruments aluminium hermetic DSC pan. The filled pan was then covered with a matching hermetic lid and the set was crimped together using a DSC pan press provided by TA instruments.

Experimental error is in the accuracy and precision of the sample mass and the contact between the DSC sensor and the sample pan.

A DSC works by applying heat to a sample containing pan and an empty pan. The result is a plot of enthalpy versus temperature. For a semi-crystalline polymer, the DSC records the energy transfer under a characteristic melting peak that is proportional to the total crystalline content within the polymer, Figure 2-8.

The area of the peak in J/g is used to determine the total crystalline content. The enthalpy of fusion, ΔH_{fus}, is the heat required to melt the crystalline regions of the polymer. A lower total ΔH_{fus} indicates less total crystallinity of the polymer. The melting temperature is a measure of the thermal stability of the crystalline regions within the polymer.

In the case of PA11 a typical well-formed crystalline peak can be observed at 189.0 ˚C, and a pre-peak related to poorly formed crystalline blocks is seen to melt at 184.5 ˚C.

After the first heating ramp on the DSC, the polymer sample is melted and its thermal history has been erased. With controlled cooling the heat of re-crystallization (ΔH_c) can be characterized.

After controlled cooling, a second heating ramp can be used to compare polymer crystalline behavior after removing environmental effects. This second heating ramp can be used to probe the effect of molecular weight on the crystallization or the effect of nano-particle inclusion on the crystallization.

By using a rapid ramp, such as 30 ˚C/min, the glass transition temperature (T_g) can be observed, Figure 2-9. The T_g was used for characterizing polyimide and GO-polyimide nanocomposites in chapter.

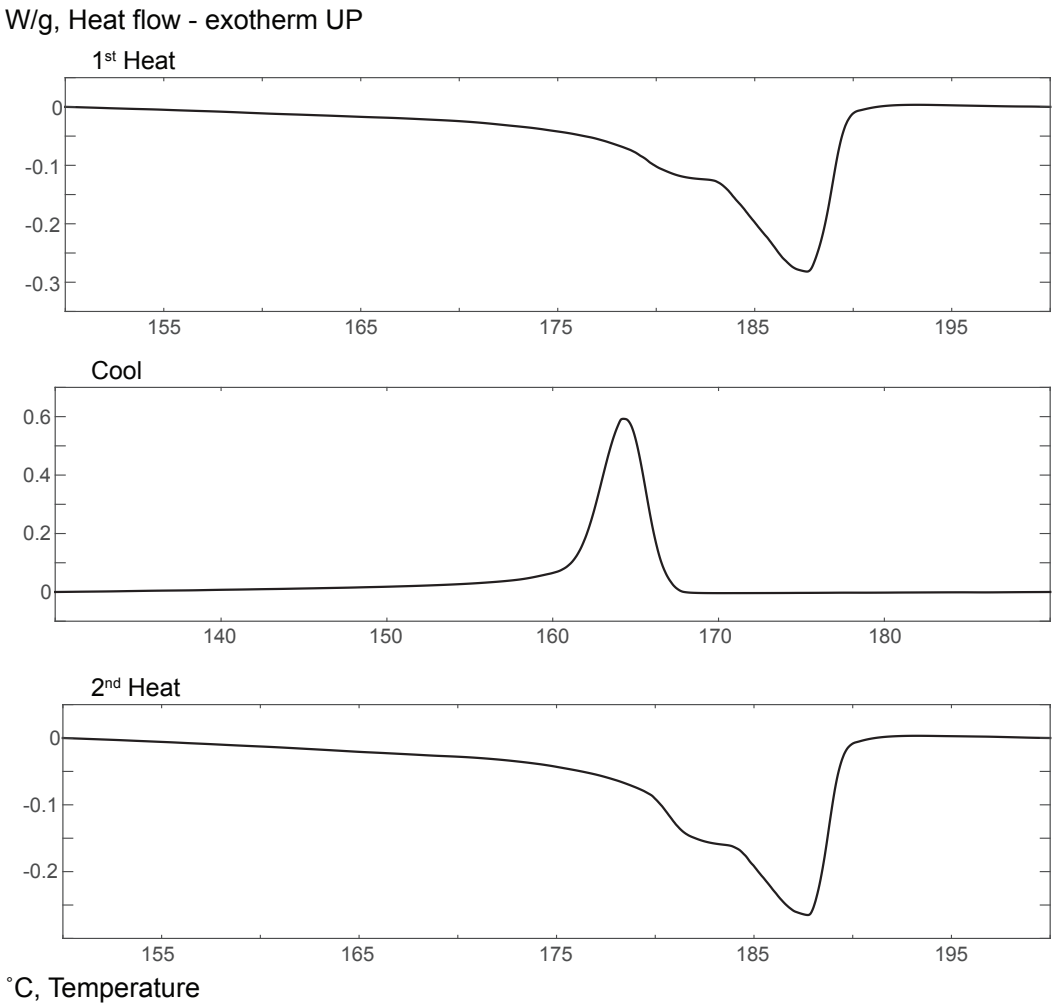

Figure 2-8: DSC measured heat flow behavior of semi-crystalline PA11: a heat/cool/heat procedure. The melting of the crystalline regions, heat of fusion ΔH_{fus}, is observed in the heating ramps and the crystalline formation, heat of crystallization ΔH_c, is measured in the cooling ramp.

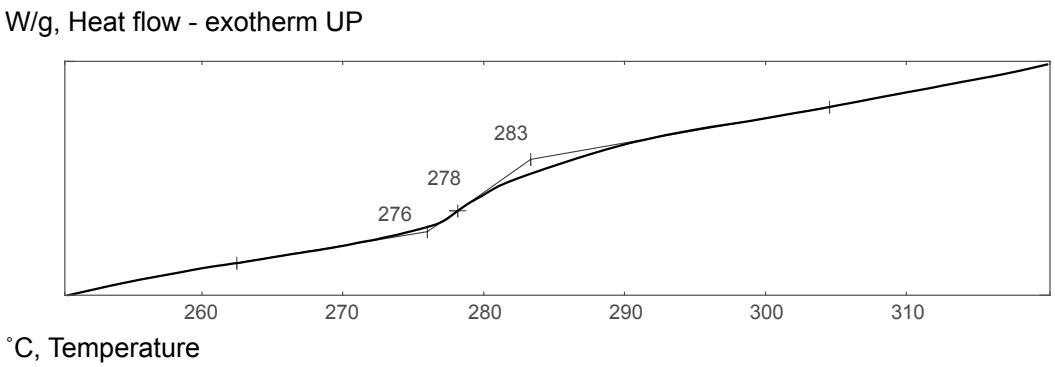

Figure 2-9: The glass transition temperature, T_g, for polyimide was measured on the DSC using a rapid heating ramp of 30 $^{\circ}C/_{min}$.

2.7 References

[2_1] HOCKER, S., RHUDY, A. K., GINSBURG, G. & KRANBUEHL, D. E. 2014. Polyamide hydrolysis accelerated by small weak organic acids. Polymer, 55, 5057-5064.

[2_2] JACQUES, B., WERTH, M., MERDAS, I., THOMINETTE, F. & VERDU, J. 2002. Hydrolytic ageing of polyamide 11. 1. Hydrolysis kinetics in water. Polymer, 43, 6439-6447.

[2_3] LAIDLER, K. J. 1987. Chemical Kinetics, New York, NY, Harper & Row.

[2_4] ZAHN, D. 2004a. Car-Parrinello molecular dynamics simulation of base-catalyzed amide hydrolysis in aqueous solution. Chemical Physics Letters, 383, 134-137.

[2_5] XIONG, Y. & ZHAN, C. G. 2006. Theoretical studies of the transition-state structures and free energy barriers for base-catalyzed hydrolysis of amides. Journal of Physical Chemistry A, 110, 12644-12652.

[2_6] BENDER, M. L. & THOMAS, R. J. 1961. Concurrent Alkaline Hydrolysis and Isotopic Oxygen Exchange of a Series of p-Substituted Acetanilides. Journal of the American Chemical Society, 83, 4183-4189.

[2_7] BROWN, R. S., BENNET, A. J. & SLEBOCKATILK, H. 1992. Recent Perspectives Concerning the Mechanism of H3O+ Promoted and OH- Promoted

Amide Hydrolysis. Accounts of Chemical Research, 25, 481-488.

[2_8] POLLACK, R. M. & BENDER, M. L. 1970. Alkaline Hydrolysis of Para Nitroacetanilide and Para Fromylacetanilide. Journal of the American Chemical Society, 92, 7190-7194.

[2_9] BAGNO, A., LOVATO, G. & SCORRANO, G. 1993. Thermodynamics of Protonation and Hydration of Aliphatic Amides. Journal of the Chemical Society-Perkin Transactions 2, 1091-1098.

[2_10] FERSHT, A. R. 1971. Acyl-Transfer Reactions of Amides and Esters with Alcohols and Thiols - Reference System for Serine and Cysteine Proteinases - Concerning N Protonation of Amides and Amide-Imidate Equilibria. Journal of the American Chemical Society, 93, 3504-3515.

[2_11] MARTIN, R. B. 1972. O-Protonation of Amides in Dilute Acids. Journal of the Chemical Society-Chemical Communications, 793-794.

[2_12] KRESGE, A. J., FITZGERA.PH & CHIANG, Y. 1974. Position of Protonation and Mechanism of Hydrolysis of Simple Amides. Journal of the American Chemical Society, 96, 4698-4699.

[2_13] ZAHN, D. 2004b. On the Role of Water in Amide Hydrolysis. European Journal of Organic Chemistry, 2004, 4020-4023.

[2_14] PAN, B., RICCI, M. S. & TROUTT, B. L. 2011. A Molecular Mechanism of Hydrolysis of Peptide Bonds at Neutral pH Using a Model Compound. Journal

of Physical Chemistry B, 115, 5958-5970.

[2_15] DUAN, P. G., DAI, L. Y. & SAVAGE, P. E. 2010. Kinetics and mechanism of N-substituted amide hydrolysis in high-temperature water. Journal of Supercritical Fluids, 51, 362-368.

[2_16] SCHOWEN, R. L., JAYARAMA.H, KERSHNER, L. & ZUORICK, G. W. 1966a. Solvent Isotope Effects in Amide Hydrolysis. Journal of the American Chemical Society, 88, 4008-4012.

[2_17] SCHOWEN, R. L., JAYARAMAN, H. & KERSHNER, L. 1966b. Catalytic efficiencies in amide hydrolysis. The two-step mechanism. 88, 3373-3375.

[2_18] ZAHN, D. 2003. Theoretical study of the mechanisms of acid-catalyzed amide hydrolysis in aqueous solution. Journal of Physical Chemistry B, 107, 12303-12306.

[2_19] WYATT, P. J. 1993. Light scattering and the absolute characterization of macromolecules. Analytica Chimica Acta, 272, 1-40.

[2_20] SMITH, B. C. 1998. Infrared Spectral Interpretation: A Systematic Approach, Boca Raton, Florida 33431, CRC Press.

Chapter 3

Polyamide hydrolysis accelerated by small weak organic acids

3.1 Introduction

It is well known that acidity, pH, of a solution accelerates the hydrolysis of soluble amides. The unexpected result that weak small organic acid at low concentrations hydrolyze a polyamide at rates approximately twice that of a water HCl solution of the same pH is described herein. The effect of three small organic acids in dilute solutions, acetic, propanoic, and butanoic was studied. It is observed that the effect on the hydrolysis rate increases as the organic acid gets weaker. Butanoic, the weakest acid, has the strongest effect on increasing the hydrolysis rate. Measurements on the concentration of these acids in the polyamide reveal that there is a selective desire for these weak organic acids to diffuse into a polyamide. The concentration of these acids in the polyamide is found to be several multiples of the concentration in the water environment. The acid concentration is highest for butanoic.

This result is important not only because it differs from the widely expected dependence on pH but because polyamides (nylons) are frequently used in everyday life and are the preferred polymer in critical applications involving hydrocarbons. Polyamide-11, because of the lower number of amide bonds for a given chain length, is widely used throughout the world as a pressure sheath in flexible pipes to transport crude oil from the ocean floor to platforms. It is also used as a liner in steel pipes for crude transport over land. When polyamide-11 (PA11) is used as the barrier in pipes for transporting crude, which is a mixture of hydrocarbons and water, over time hydrolytic degradation of PA11 occurs.

This can result in low molecular weights where PA11 looses its ductility and becomes brittle. This is the so called ductile-brittle transition [1,2]. Knowing that the molecular weight at a given time is above the ductile-brittle transition onset molecular weight is the primary factor for continued safe use. Understanding the factors governing amide hydrolysis kinetics is therefor not only of fundamental scientific interest but essential in understanding polyamide's useful life.

The kinetics of polyamide degradation in water has been extensively studied [3-13]. The existence of an equilibrium molecular weight, which occurs when the rates of hydrolysis and repolymerization become equal, was established for varied temperatures and initial molecular weights [3-5]. Studies have examined the hydrolytic degradation of both neat and plasticized PA-11 in environments of water [3-11], salt water [10], oilfield water [6], crude oil [6,10], and in acidic [5,12,13] conditions.

Meyer, Jones [3] and Jacques, Werth [4] have both shown that in the absence of oxygen, PA11 reaches an equilibrium molecular weight when aged in deionized water. Acidic conditions have been shown to accelerate amide hydrolysis [5,6,11,12,14]. The chemical effects that acids have on polyamide hydrolysis are amine scavenging and acid catalysis [5,15-19]. Merdas, Thominette [5] showed that the average equilibrium molecular weight (M_{me}) of aged PA11 is lowered in carbonic acid, pH 4, by approximately 1 kDa at 130 ˚C and 3 kDa at 160 ˚C due to CO_2 solubility in the polymer. They also propose a model to predict the equilibrium molecular weight for PA11 aged in an acidic aqueous environment.

Their model requires the acid concentration within the PA11 matrix to be known. Merdas et al. suggest that for weak acids there is no catalytic effect and that weak acids could effect PA11 hydrolysis by shifting the equilibrium towards lower values of M_{me} [5]. Chaupart, Serpe [13] reported a strong pH acid effect on PA11 hydrolysis at low pH's of 4, 2, and 0. But the presence of oxygen was uncontrolled and an equilibrium was not observed. The absence of an equilibrium is now the expected result when oxidation and hydrolysis are both degrading the polyamide chain. Naphthenic carboxylic acids in crude oil are also known to accelerate the degradation process beyond the aging in pH 7 water. Naphthenic acids have been shown to degrade polyamides primarily on the surface [20].

Recently, Romao, Castro [6] aged PA11 in oilfield water, with a pH of 5.5. They report a very large equilibrium molecular weight decrease (10 kDa) compared with deionized water. Such a significant decrease of the equilibrium molecular weight remains unexplained by the oilfield water pH of 5.5. Here it is proposed that this result is related to other molecular species in the oilfield water, particularly small hydrocarbon acids such as acetic acid, which is found in many oilfields.

The work herein reveals the importance of understanding the molecular species present during hydrolytic degradation conditions. It is reported that a significant increase in the rate of degradation was caused by small organic acids and the molecular basis for the unexpected large effect of weak organic small acids, acetic, propanoic, and butanoic is discussed.

Here it is shown that the smaller and much weaker organic acids significantly accelerate degradation process even more than HCl water at similar pH conditions. This effect occurs at the very low concentrations of small organic acids often found in crude oil reservoirs. Characterization of this surprising effect of weak, small organic acids on the rate of degradation is one objective of this work. Determining the effect of the organic acid's structure and concentration is another. Most important is development of a fundamental understanding of why the rate of degradation is uncorrelated with the small organic acids acidity and is so strong given the very low acidity of small organic acids. This report focuses on the effect of three low molecular weight organic weak acids (acetic, propanoic, and butanoic) on accelerating the aging of PA11 at 100 ˚C and 120 ˚C, at a constant molarity.

3.2 Experimental

3.2.1 Making PA11 coupons

PA11 was made in our laboratory by heating the monomer, 11-aminoundecanoic acid, purchased from Sigma-Aldrich, at 240 ˚C for 3 hours. The polymer material was then pressed into the form of a film, 15×7×0.25 cm^3. The film was punched into 1 cm diameter coupons for aging.

Commercially polymerized PA11 Besno P40TL made by Arkema was supplied by National Oilwell VARCO of Denmark. The commercial PA11 has n-butyl benzene sulfonamide (BBSA) at 12 wt% to function as a plasticizer. The function of the plasticizer is to disrupt hydrogen bonding in the amorphous region of the polymer matrix [21]. Coupons having a cylindrical shape with 1 cm diameter and 1 cm thickness were punched from this extruded commercial PA11.

3.2.2 Aging conditions

The coupons were immersed in deionized water and controlled acidic solutions over a period of months at controlled constant temperatures of 100 ˚C and 120 ˚C to accelerate aging. Ace #40 high pressure rated glass tubes with teflon plugs were used as the containment vessels. Dissolved oxygen was removed, to avoid oxidation effects, by sparging the aging solution with argon in the

containment vessel to keep the oxygen level below 50 ppb.

One set of aging solutions was made using three small weak organic acids: acetic, propanoic, and butanoic. Each acid was mixed with deionized water at a concentration of 1.05×10^{-2} M. Deionized water was the control aging solution. Previous work has characterized the molecular weight degradation behavior of PA11 aged in deionized water for a range of temperatures [3,5-11]. Laboratory made PA11 coupons were aged in these 1.05×10^{-2} M small organic acid solutions at 100 ˚C and 120 ˚C.

A second set of aging solutions was made to create a range of pH values and conditions to explore the effect of H^+ ions at pH conditions similar to that of the three weak organic acids. A hydrochloric acid solution with a pH of 2.9 was prepared by diluting HCl into deionized water. Acetic acid was diluted into deionized water to 6.29×10^{-2} M and a pH of 2.9. A carbonic acid solution, having a pH of 4.2, was prepared by bubbling deionized water with carbon dioxide for 15 min at a flow rate of 400 mL/min. Finally, a buffer solution was used to control the ratio of protonated and deprotonated acetic acid during aging. Since a buffered solution has a known pH, this ratio is easily calculated using the Henderson-Hasselbach relationship, Equation 3-1 [22,23]. In the buffered system, significantly more acetic acid exists in the de-protonated form, compared to a normal system. Sørensen's phosphate buffer was used, which consists of monobasic and dibasic sodium hydrogen phosphate. The buffer was prepared at a 0.3 M concentration and used to create an acetic acid 6.29×10^{-2} M solution

with a buffered pH of 6.2. The punched commercial extruded PA11 coupons were immersed in the environments at 100 ˚C.

Equation 3-1:

$$pH = pK_a + log\frac{[A-]}{[AH]}$$

3.2.3 Measuring mass average molecular weight, M_m, and crystalline content

Details are on page 20 regarding the measurement of mass average molecular weight, M_m. The SEC-light scattering M_m measurements in this work have a 6 % instrumental error. The error was determined by the standard deviation divided by the mean for six consecutive M_m measurements on a single solution of unaged laboratory-made PA11.

The crystalline content of PA11 was measured using a TA Instruments Q20 differential scanning calorimeter (DSC). The ramp rate was 3 $^{\circ}C/min$ and the integration limits were 150 ˚C to 200 ˚C.

3.2.4 Mathematical modeling and characterization of polyamide accelerated aging

We characterized the equilibrium molecular weight (M_{me}), pseudo-hydrolysis

(k'_H), and solid state polymerization (k_p) rate constants during accelerated molecular weight degradation by fitting a mathematical model of amide hydrolysis to the measured M_m per aging time. The values k'_H and k_p, which are used to fit the changing values of molecular weight with time, reflect the composition of the aqueous aging environment and its effect on the hydrolysis process: details on page 14.

3.2.5 Acid absorption characterization

Three grams of PA11 beads, supplied by Sigma-Aldrich, were placed in the small organic acid solution and weighed each day for a period of 10 days at 100 ˚C with oxygen removed. These small organic acid solutions ranged in concentration from 1 to 8.75 molarity in deionized water.

In a preliminary experiment we had found that the PA11 beads reach a constant volatile content by day 5 at 100 ˚C and retained that value for 35 days. Therefore after 10 days the beads were removed from 100 ˚C temperature aging environment. Using a Kimwipe tissue, the surfaces were patted dry before final massing of the bead group. Three of these beads were used for thermogravimetric analysis. The remaining beads were placed in a dry round bottom flask. The beads were heated to 220 ˚C in the round bottom flask and the vapor from the heated beads was condensed and collected, the distillate. The composition of the distillate was quantified using gas chromatography. The area of the acid peak was

calibrated to moles. Using the calibration of area to moles and the volume injected, the acid molarity of the distillate was determined from the gas chromatograph results.

3.3 Results and discussion

Figure 3-1 and Figure 3-2 show that the degradation process leads to an equilibrium mass average molecular weight (M_{me}), when aging PA11 anaerobically in 1.05×10^{-2} M solutions of these weak organic acids. The equilibrium is achieved when the rate of chain scission equals the rate of recombination as shown in Equation 2-1 on page 15. The equilibriums observed for the pH 7 water condition at both 100 ˚C and 120 ˚C agree with previously published results. In water, Meyer, Jones [3] report M_{me} in the range of 23.5 and 32.5 kDa at temperatures of 135, 120, 105, and 90 ˚C and Jacques, Werth [4] report an equilibrium M_m of 26 kDa at 80 ˚C [3,4]. Figure 3-1 and Figure 3-2 also show that the rate of degradation is somewhat faster in the presence of all three acids than in water. The figures also show that the rate of hydrolysis and the equilibrium molecular weight are both a function of the acid hydrocarbon chain length. Butanoic acid, the weakest of these three acids, has the strongest degradative effect.

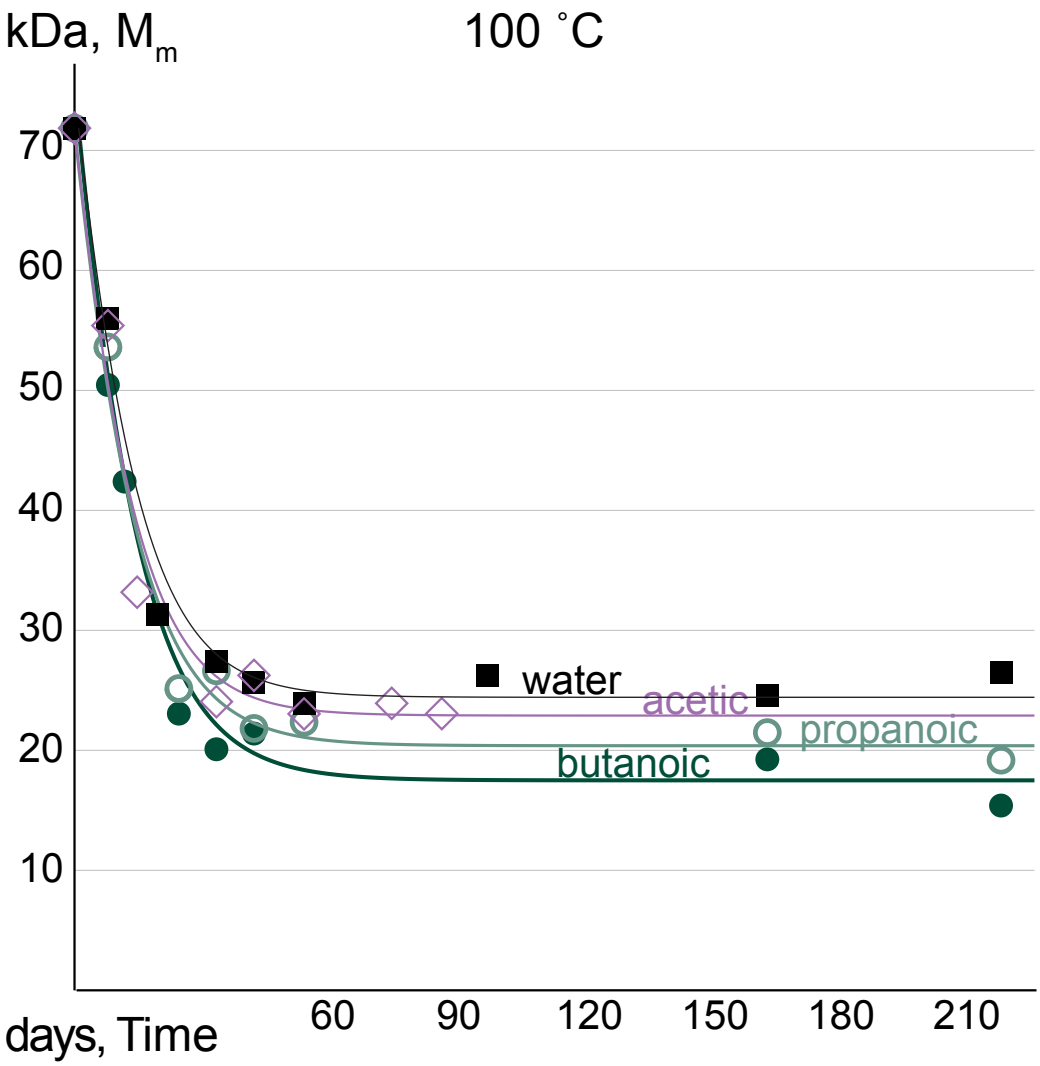

Figure 3-1: A plot of the Light Scattering measured M_m over time for PA-11 aged at 100 ˚C in small organic acid solutions.
■ water data; —— water fit.
◇ acetic data; —— acetic fit.
○ propanoic data; —— propanoic fit.
● butanoic data; —— butanoic fit.

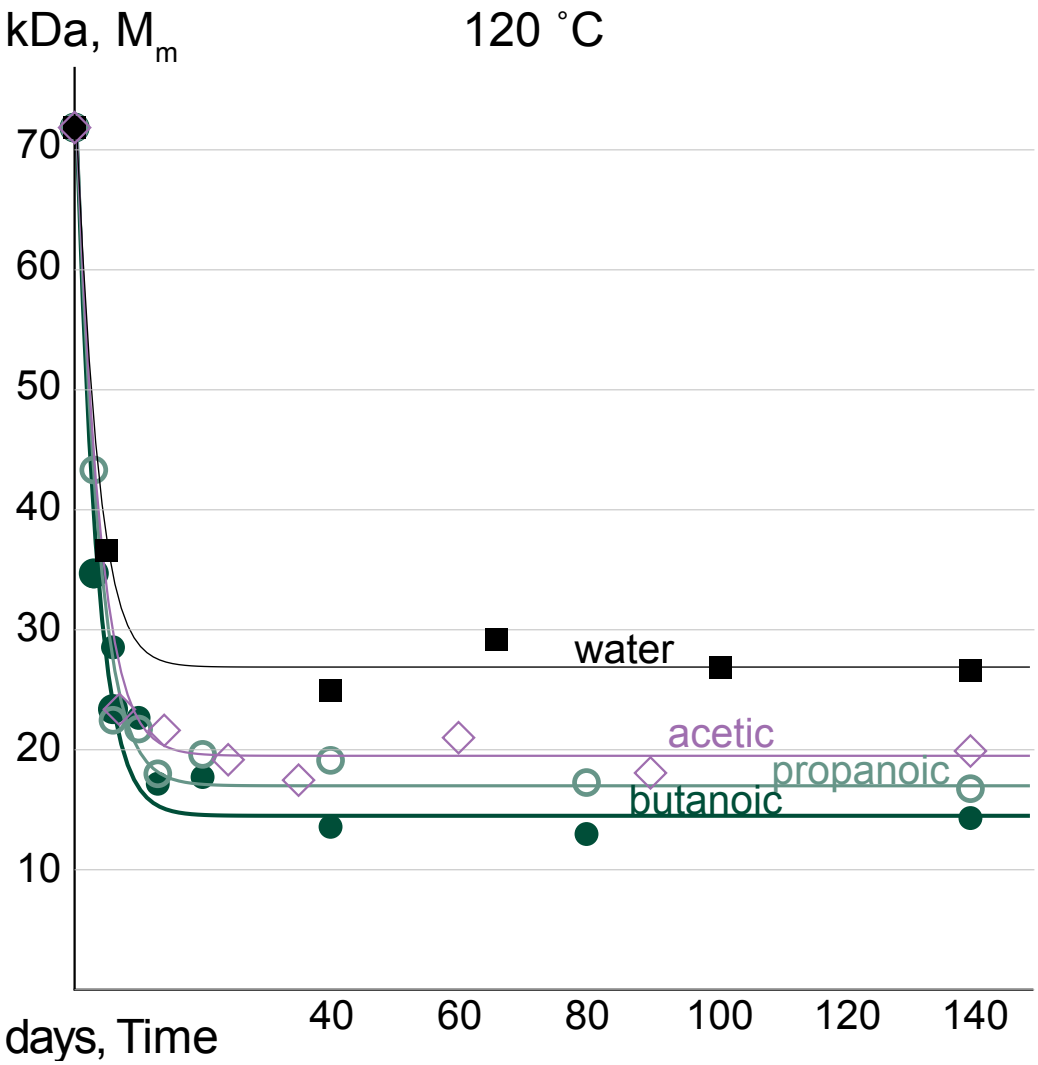

Figure 3-2: A plot of the Light Scattering measured M_m over time for PA-11 aged at 120 ˚C in small organic acid solutions.
■ water data; —— water fit.
◇ acetic data; —— acetic fit.
○ propanoic data; —— propanoic fit.
● butanoic data; —— butanoic fit.

Table 3-1: Rate constants and equilibrium molecular weight for laboratory made PA11 aged in 1.05 $\times 10^{-2}$ *M* aqueous weak organic acid conditions; determined using the measured M_m over time and a non-linear least squares fit of the hydrolysis kinetic model Equation 2-12.

Solution	$k'_H \times 10^{-1}$	$k_P \times 10^{-4}$	kDa, M_{me}
100 ˚C			
Water	0.43	1.68	24.4
Acetic	0.45	1.57	22.9
Propanoic	0.46	1.28	20.4
Butanoic	0.50	1.05	17.5
120 ˚C			
Water	1.64	7.88	26.9
Acetic	1.84	4.71	20.0
Propanoic	1.99	4.04	17.0
Butanoic	2.32	3.66	14.5

The previously described hydrolysis model was used to fit to the changing mass average molecular weight, M_m, versus time, shown in Figure 3-1 and Figure 3-2 [3,4,25]. The hydrolysis model's parameters include the equilibrium molecular weight (M_{me}), pseudo-hydrolysis (k'_H) rate constant, and polymerization (k_P) rate constant. The results are reported in Table 3-1. Additionally we investigated the most aged,140 days at 120 ˚C, laboratory made PA11 samples for their changing chemical structure using differential scanning calorimetry (DSC). The unaged PA11 integrated melting peak area is 48.4 (J/g), while the water, acetic, propanoic, and butanoic aged samples were 100.9, 99.7, 97.6, and 99.2 (J/g) respectively. The result shows that during accelerated aging at 120 ˚C there is significant annealing. The increase in crystallinity in the neat PA11 is similar for the aging in water and in the organic acid environments at 120 ˚C.

Table 3-1 shows that the k'_H increases and k_P decreases with the increasing

alkyl chain length of these small organic acids: acetic, propanoic, and butanoic. The model parameter k'_H is determined by the initial decrease in M_m with time. This result is the opposite of the expected effect based on the acid strength of these three acids. Acetic is the strongest acid of the group with a $pK_a = 4.75$, and butanoic is the weakest acid with a $pK_a = 4.81$. The value k_P is determined by the equilibrium concentration of unreacted amine groups and k'_H as seen in the model's Equation 2-4 and Equation 2-10.

Table 3-2: Weight gain and acid concentration in neat PA11 aged at 100 ˚C in 1 *M* acid solutions, measured using gas chromatography, weight gain, and thermogravimetric analysis (TGA).

1 *M* acid Solution	***M* Concentration of acid in distillate**	**% Mass change measured by**	
		Gravimetry	**TGA**
Acetic	1.7	3.4	4.0
Propanoic	3.9	5.5	6.9
Butanoic	6.5	14.4	12.4

Table 3-3: The molarity of the aging acid solution versus the acid molarity of the distillate. The table reports the concentration of the acid within the PA11 matrix after 10 days at 100 ˚C, and the moles of acid and water respectively within the 2 mL injection aliquot of the distillate based on the GC results and the calibration of peak area to moles.

Acid molarity of		**Moles in distillate of**	
Aging solution	**Distillate**	**Acid $\times 10^{-5}$**	**Water $\times 10^{-5}$**
Acetic			
1.0	1.9 ± 0.2	0.38 ± 0.04	10 ± 0.8
2.2	5.6 ± 0.5	1.1 ± 0.1	7.9 ± 0.9
4.4	8.7 ± 1.0	2.0 ± 0.3	3.1 ± 1.7
8.7	10.0 ± 2	2.0 ± 0.4	5.8 ± 0.5
Propanoic			
1.0	3.9 ± 0.0	0.79 ± 0.00	6.1 ± 0.1
2.2	6.6 ± 0.6	1.3 ± 0.1	3.6 ± 0.4
3.4	8.0 ± 1.3	1.6 ± 0.3	7.5 ± 1.2
4.4	7.9 ± 0.1	1.6 ± 0.0	3.3 ± 0.3
6.7	8.5 ± 0.6	1.7 ± 0.1	3.5 ± 0.4
8.7	8.3 ± 0.7	1.7 ± 0.1	2.4 ± 0.5
Butanoic			
1.0	6.5 ± 0.1	1.3 ± 0.0	4.7 ± 0.1
2.2	4.9 ± 0.3	0.98 ± 0.06	1.8 ± 0.4
2.7	4.8 ± 0.3	0.95 ± 0.05	5.3 ± 1.4
4.4	8.2 ± 0.5	1.6 ± 0.1	3.9 ± 0.0
5.4	7.6 ± 1.8	1.5 ± 0.4	2.9 ± 0.9
8.7	6.5 ± 0.6	1.3 ± 0.1	2.1 ± 0.2

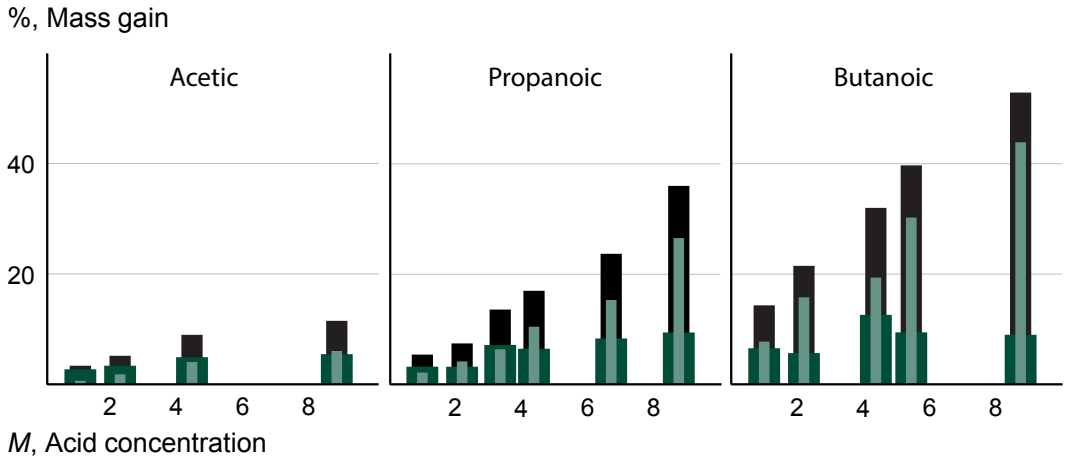

Figure 3-3: PA11 weight gain at 100 ˚C in a small organic acid. (■) Total mass percent gain measured using gravimetry versus acid concentrations. The percent content of (■) acid and (■) water measured in the distillate with gas chromatography.

To help explain this result, acid absorption measurements as described in section 3.2.5 were conducted. The experimentally determined increase in mass of PA11 due to ingress of water and acid molecules when immersed in 1 M solutions of each acid at 100 ˚C for 10 days is shown in Table 3-2. The mass gain became constant after 3 days and remained constant for 10 days. On the tenth day, the concentration of the acid in the PA11 beads was determined from the distillate collected from the retrieved PA11 as described in the experimental section. The results are shown in Table 3-2. The results show that an increase in both the mass gain and the concentration of the acid in the PA11 increases with the length of the alkyl chain in going from acetic, to propanoic, to butanoic.

Particularly important, Table 3-2 shows that after aging PA11 in each 1 M acid solution the acid concentration in the polyamide is higher inside the PA11 matrix than in the initial aging solutions. The molar acid concentration of the distillate, Table 3-2, shows increases for each acid: acetic, propanoic, and butanoic. The largest increase above the concentration of the aging solution occurs for butanoic acid.

In summary these small, weak organic weak acids are preferentially absorbed into the solid polyamide from the aging environment according to their molecular structure. As shown in Figure 3-1 and Figure 3-2 they degrade the polyamide faster and to a lower equilibrium molecular weight as the alkyl chain length increases. Further as shown in Figure 3-1 and Figure 3-2 the degradation process is somewhat faster for the 1.05×10^{-2} M weak organic acids with a pH near 3.3

than in water. The affinity of these acids to diffuse in to the solid polyamide lowers the pH within the polymer and thereby inhibits the repolymerization of broken amide bonds most likely by protonating the free amine end, amine scavenging [5,20].

Figure 3-3 and Table 3-3 add further insight into the reasons why these small organic acids have such a large unexpected effect on the degradation process. In Figure 3-3 the PA11 weight gain is shown after 10 days when immersed in acetic, propanoic, and butanoic acid solutions of varying molarity from 1.0 M to 8.7 M. Figure 3-3 shows the increase in the mass percent of the acid and the mass per cent of the water as the molar concentration of the aging environment increases. Again, butanoic acid, the weakest acid shows the largest increases at each molarity of the aging solution.

Table 3-3 shows that the acid molarity and the ratio of the acid to water molecules that have diffused in to the solid PA11 is a function of the molarity of the aging environment. When exposed to the 1 M acid environment, the molarity in the solid PA11 versus in the aging solution is 1.9 times higher for acetic acid, 3.9 times higher for propanoic, and 6.5 times higher for butanoic acid. As the molarity of the environment increases these values increase, but the relative concentration increase in the polymer decreases indicating an approach to saturation.

The important conclusion is that the longer the alkyl chain, the higher the concentration of these small organic acids in the PA11. Most important for

all three acids, these acids prefer to be in the PA11 more than in the water environment.

Finally the affinity of the acetic acid to diffuse into PA11 as an undissociated protonated weak acid versus the affinity of the dissociated proton and acetate ion is explored along with the affinity of the hydronium ion to effect hydrolytic degradation at similar pH, acid concentrations. As described in the experimental section, commercially extruded Besno P40TL PA11 was aged in five environments at 100 ˚C: pH = 7 water; 6.29×10^{-2} M acetic acid, with pH = 2.98; 6.29×10^{-2} M acetic acid buffered to a pH of 6.2; water saturated with CO2, with a pH of 4.2; and HCl water with a pH of 2.9.

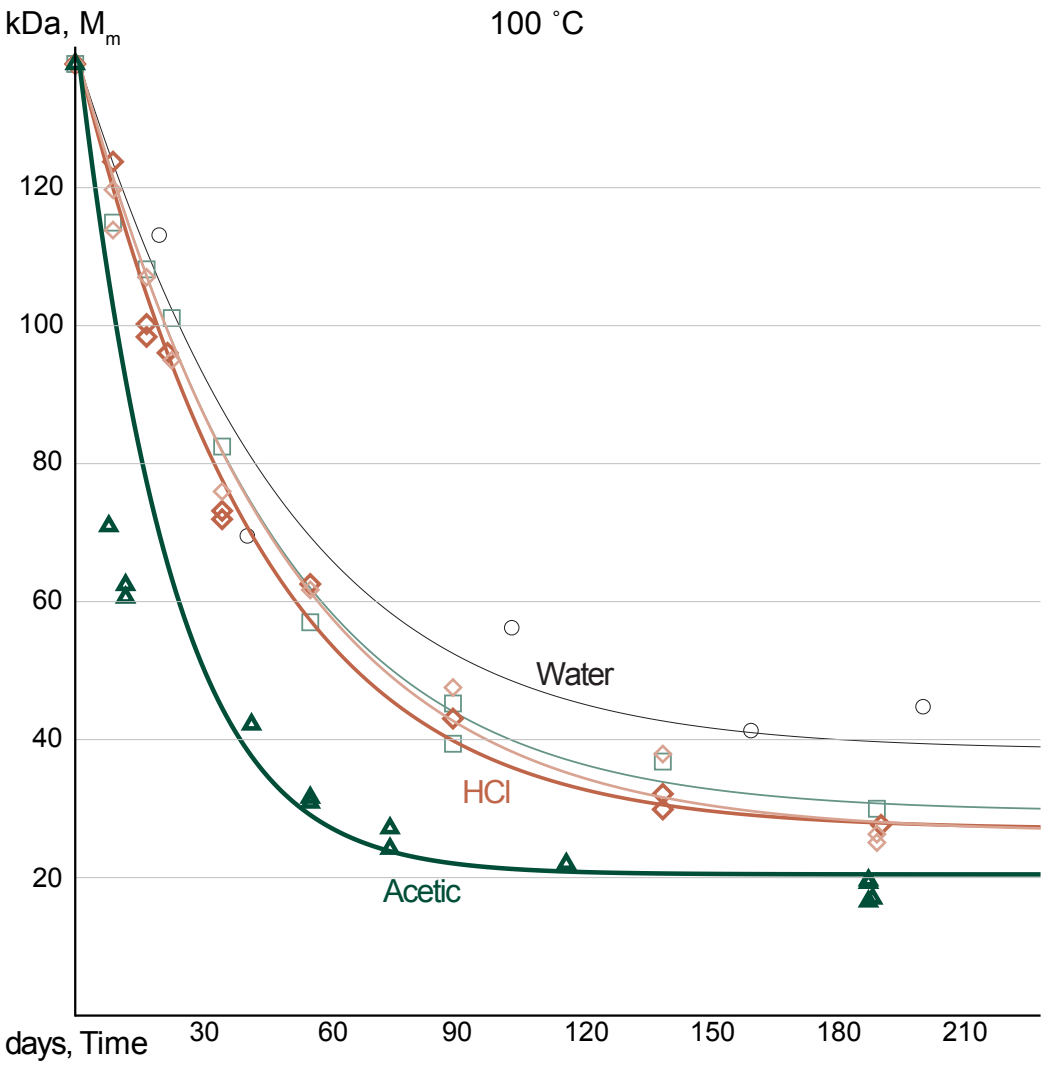

Figure 3-4: Commercial plasticized PA-11 aged at 100 ˚C in various aqueous acid conditions. M_m data was measured using SEC-MALLS.
○ pH=7 water data; —— water fit.
□ pH=6.2 buffered acetic acid at 6.29 $\times 10^{-2}$ *M* data; —— buffered acetic acid fit.
◇ pH=4.2 CO_2 data; —— CO_2 fit.
◇ pH=2.9 HCl data; —— HCl fit.
▲ pH=2.98 acetic acid at 6.29 $\times 10^{-2}$ *M* data; —— acetic acid at 6.29 $\times 10^{-2}$ *M* fit.

Table 3-4: Rate constants and equilibrium molecular weight for commercial Besno P40TLOS PA11 aged in various aqueous acid conditions; determined using the measured M_m over time and a non-linear least squares fit of the hydrolysis kinetic model Equation 2-12.

Solution	pH	$k'_H \times 10^{-2}$	$k_P \times 10^{-5}$	kDa, M_{me}
100 ˚C				
Water	7.0	1.38	1.95	38.5
Buffered acetic	6.2	1.59	1.44	29.5
CO_2	4.2	1.59	1.23	26.5
HCl	2.9	1.76	1.39	27.0
Acetic	2.9	3.71	1.98	20.5

Figure 3-4 displays the aging results. Table 3-4 reports the values of the equilibrium molecular weight, psuedo-hydrolysis k'_H rate constant and the chain recombination k_P rate constant. When aging in water at 100 ˚C, a difference is seen between the laboratory made and the commercially extruded Besno P40TL PA11 resulting equilibrium molecular weights, 24.4 kDa and 38.5 kDa respectively. The higher equilibrium molecular weight is an effect of the BBSA plasticizer presence during the aging process, partially explained by its ability to disrupt hydrogen bonding in the amorphous phase of the PA11 [21]. Jacques et al. report an equilibrium number average molecular weight (M_{ne}) of 19.3 for Besno P40TL PA11 when aged in water at 100 ˚C. A M_{ne} of 19.3 is a M_{me} of 38.6 and is in agreement with our measurements, knowing the polydispersity index for PA11 is two [4,26]. Domingos et al. aged BBSA containing Besno P40TL PA11 at 110 ˚C in water for 50 days and report a corrected inherent viscosity (CIV) of 1.19 (dL/g) that coverts to a M_m of 38 kDa using our Mark-Houwink relationship [9].

Table 3-5: Hansen solubility parameters [27].

Solvent	Dispersion	Polarity	H-bonding	Molecular Volume
Water	15.5	16.0	42.3	18.0
Acetic	14.5	8.0	13.5	57.5
Propionic	14.7	5.3	12.4	75.0
Butanoic	14.9	4.1	10.6	110.0
m-Cresol	18.0	5.1	12.9	104.7
HFIP	17.2	4.5	14.7	105.3
PA11	17.0	4.4	10.6	

Meyer, Jones [3] show that when aging neat PA11 at 105 ˚C in water the M_{me} is around 25 kDa [3]. Jacques, Werth [4] corroborate Meyer's results, reporting a M_{me} of 26.5 kDa when aging additive free PA11 at 80 ˚C in water for 200 days [4].

It is clear from Figure 3-4 and Table 3-4 that the unbuffered 6.29×10^{-2} *M* acetic acid environment with a pH of 2.98 is the most degradative and has the largest effect on the hydrolysis rate constant. The acetic acid in a primarily ionized acetate state has little effect on the rate of degradation indicating it is in its undissociated state that it is soluble in the PA11. The HCl environment with a similar pH acidity has a much weaker effect on hydrolytic degradation in the solid PA11 than does the weak acetic acid. The accelerated chain scissions in Figure 3-4 and Table 3-4 are shown to be the direct result of higher acetic acid concentration within the polyamide matrix. Acid catalysis of the PA11's amide bond is not changed very much by the pH of the water environment as shown by the CO_2 pH =4.2 and the HCl pH =2.9 water environments. Large increases in degradation occur because of the high concentration of the butanoic acid versus propanoic versus acetic acid within the PA11.

In summary, the high concentrations of small organic acids also lead to a decrease in k_p and a lower equilibrium molecular weight M_{me}. Increased concentrations of these carboxylic acid groups in the polyamide matrix lead to end-capping. The small organic acid is proposed to bond with the amide end-group on a polyamide chain inhibiting recombination with a carboxylic end-group of another chain. This suppresses the re-polymerization and lowers the equilibrium molecular weight M_{me}.

These molecular weight degradation results and the concentration of the small organic acids in PA11 can be understood by the similarity of polyamides and these acids structures, a hydrocarbon chain terminated with a carboxylic acid group. This is reflected in their solubility parameters, Table 3-5. Herein the most similar solubility parameter to polyamide is butanoic, then propanoic, and then acetic. The least similar solubility parameter is water.

Finally, the results in Table 3-4 show that in the absence of unusual solubility effects, the concentration of H^+ ions in a water environment, pH of the water environment, is correlated with only modest increases in the hydrolysis rate and a modest reduction in the equilibrium molecular weight in the pH range of 3 to 7. This effect of the presence of small organic acids is uncorrelated and not predicted based on the pH of the aging environment.

3.4 Conclusion

Small organic acids such as acetic, propanoic, and butanoic in water

significantly accelerate the rate of degradation due to hydrolysis and reduce the recombination rate. Thereby small organic acids produce a large reduction in the equilibrium molecular weight. Butanoic acid, the weakest of these acids, has the largest effect on the rate of hydrolysis and the largest effect on the reduction in the equilibrium molecular weight.

Small organic acids have a much larger effect than an HCl water environment at the same pH on the rate and extent of degradation. The fundamental molecular basis for this previously unexpected and unreported result is the similarity in structure to the polyamide and the solubility for these acids in their undissociated state to diffuse into the solid polyamide, creating acid concentrations many times that in the aging water-acid environment.

3.5 References

[3_1] UBRICH, E., FAFET, A., ROBERT, E. & SERPE, G. 1994. Vieillissement du Polyamide 11 Utilise Dans les Conduites Flexibles: Influence de la Composition du Fluide Transporte. Revue de l'institut Francais du Petrole, 49, 165-175.

[3_2] FAYOLLE, B., RICHAUD, E., COLIN, X. & VERDU, J. 2008. Review: degradation-induced embrittlement in semi-crystalline polymers having their amorphous phase in rubbery state. Journal of Materials Science, 43, 6999-7012.

[3_3] MEYER, A., JONES, N., LIN, Y. & KRANBUEHL, D. 2002. Characterizing and Modeling the Hydrolysis of Polyamide-11 in a pH 7 Water Environment. Macromolecules, 35, 2784-2798.

[3_4] JACQUES, B., WERTH, M., MERDAS, I., THOMINETTE, F. & VERDU, J. 2002. Hydrolytic ageing of polyamide 11. 1. Hydrolysis kinetics in water. Polymer, 43, 6439-6447.

[3_5] MERDAS, I., THOMINETTE, F. & VERDU, J. 2003. Hydrolytic ageing of polyamide 11—effect of carbon dioxide on polyamide 11 hydrolysis. Polymer Degradation and Stability, 79, 419-425.

[3_6] ROMAO, W., CASTRO, E. V. R., FILHO, E. A. S., GUIMARAES, R. C. L., SILVA, A. L. N., TEIXEIRA, S. C. S., DE PAOLI, M.-A. & DE SENA, G. L. 2009. Ageing of polyamide 11 used in the manufacture of flexible piping. Journal of Applied Polymer Science, 114, 1777-1783.

[3_7] HOCHSTETTER, G., AMOUROUX, N., HUGON, L., DANG, P. & WERTH, M. 2007. Polyamide 11 in Offshore Conditions, Hydrolytical Ageing, Mechanical Behaviour in Flexible Pipes. 26th International Conference on Offshore Mechanics and Arctic Engineering, 561-572.

[3_8] HOCHSTETTER, G. & DANG, P. 2009. Correlation between hydrolysis and the ultimate mechanical properties of polyamides in offshore conditions. ASME 2009 28th International Conference on Ocean, Offshore and Arctic Engineering, 797-803.

[3_9] DOMINGOS, E., PEREIRA, T. M. C., FILGUEIRAS, P. R., BUENO, M. I. M. S., DE CASTRO, E. V. R., GUIMARAES, R. C. L., DE SENA, G. L., ROCHA, W. F. C. & ROMAO, W. 2012. Monitoring the polyamide 11 degradation by thermal properties and X-ray fluorescence spectrometry allied to chemometric methods. X-Ray Spectrometry, 42, 79-86.

[3_10] BERGER, J., FRANOSCH, J., SCHUETT, C., DOWE, A. & AG, E. I. 2011. The Aging of Offshore Polyamides under Services Conditions in Subsea Applications. Offshore Technology Conference. Rio de Janeiro, Brazil.

[3_11] GLOVER, A. J. M. 2011. Characterization of PA11 Flexible Pipe Liner Aging in the Laboratory and in Field Environments Throughout the World. Doctor of Philosophy Dissertation, The College of William and Mary.

[3_12] SERPE, G. & CHAUPART, N. 1997. Ageing of polyarnide 11 in acid solutions. 38, 1911-1917.

[3_13] CHAUPART, N., SERPE, G. & VERDU, J. 1998. Molecular weight distribution and mass changes during polyamide hydrolysis. Polymer, 39, 1375-1380.

[3_14] MYAGKOV, V. A. & PAKSHVER, A. B. 1952. Kinetics of Hydrolysis of Caprolactam and of polyamide resin. Kolloid Zhur., 14, 172.

[3_15] ZAHN, D. 2004. On the Role of Water in Amide Hydrolysis. European Journal of Organic Chemistry, 2004, 4020-4023.

[3_16] ZAHN, D. 2003. Theoretical study of the mechanisms of acid-catalyzed amide hydrolysis in aqueous solution. Journal of Physical Chemistry B, 107, 12303-12306.

[3_17] BROWN, R. S., BENNET, A. J. & SLEBOCKA-TILK, H. 1992. Recent Perspectives Concerning the Mechanism of H3O+ and OH- Promoted Amide Hydrolysis. Accounts of Chemical Research, 25, 481-488.

[3_18] MULLER, A. & PFLUGER, R. 1960. High acid hydrolysis resistance of polyamides 11 and 12 compared to polyamides 6 and 6,6. Kunststoffe, 50, 203.

[3_19] WYNESS, K. 1960. High acid hydrolysis resistance of longer carbon chain polyamides compared to polyamides 6 and 66, study of stress cracking. Makromol Chem, 38.

[3_20] API 2003. Technical Report 17TR2, The Ageing of PA11 in Flexible Pipes. Washington, DC: American Petroleum Institute.

[3_21] SERPE, G. & CHAUPART, N. 1996. Relaxation-structure relationship in bulk and plasticized polyamide 11. Journal of Polymer Science Part B: Polymer Physics, 34, 2351-2365.

[3_22] HENDERSON, L. J. 1908. Concerning the relationship between the strength of acids and their capacity to preserve neutrality. American Journal of Physiology, 21, 173-179.

[3_23] HASSELBALCH, K. A. 1916. Die Berechnung der Wasserstoffzahl des Blutes aus der freien und gebundenen Kohlensäure desselben, und die Sauerstoffbindung des Blutes als Funktion der Wasserstoffzahl, Julius Springer.

[3_24] CHEN, J., RADKE, W. & PASCH, H. 2003. Analysis of Polyamides by Size Exclusion Chromatography and Laser Light Scattering. Macromolecular Symposia, 193, 107-118.

[3_25] LAIDLER, K. J. 1987. Chemical Kinetics, New York, NY, Harper & Row.

[3_26] FLORY, P. J. & FLORY, J. 1936. Molecular Size Distribution in Linear Condensation Polymers 1. Journal of the American Chemical Society, 58, 1877-1885.

[3_27] HANSEN, C. M. 2000. Hansen Solubility Parameters - a user's handbook.

Chapter 4

The Ductile-Brittle Transition of Polyamide-11 as Determined by Molecular Weight and Crystallinity

4.1 Introduction

At the molecular level, chain entanglements are the key factor in determining the ductile-brittle behavior of a polymer. For an amorphous linear chain polymer, a critical entanglement molecular weight (M_c) can be characterized[1-4]. The knowledge of how the molecular weight influences polymer embrittlement has been extended to linear chain semi-crystalline polymers, but the relationships between the crystalline domains, chain entanglement, and molecular weight are complex. Predictions based on molecular weight alone are imprecise[5-13]. Recently the distance between lamellar crystalline regions during oxidative degradation has been proposed to monitor the onset of brittleness in polyethylene and polyamide-11[8, 9]. Chain entanglement in the amorphous region is the key to ductility and is determined by the size of the amorphous region between the crystalline lamellae. In an effort to understand the correlated effects of M_m and crystallinity on ductility the significant challenge of making PA11 of the same M_m but different crystallinity was overcome by using small organic acids. By aging at different rates, the two inter-related effects of M_m and percent crystallinity on PA11's ductility were de-coupled.

The acquired knowledge in this study describes the relationship of the length of polymer chains and the percent crystallinity and provides a far more accurate means to detect the onset of the ductile-brittle transition.

Offshore grade commercial PA11 has three inter-related properties

affecting its operational lifetime as an inner pressure sheath: the additives, crystallinity, and molecular weight. The additive in offshore grade PA11 is N-n-butylbenzenesulfonamide (BBSA) and the purpose of BBSA is to disrupt hydrogen bonding and thereby decrease the crystallinity of PA11. This makes PA11 more ductile and easier to extrude. Research has shown that hydrolytic aging results in an equilibrium molecular weight[14, 15], and that BBSA has the added benefit of a higher equilibrium molecular weight[13, 16]. Romao, Castro [17], Domingos, Pereira [18] showed that the additive, BBSA, results in a higher equilibrium M_m during accelerated water aging.

The 2003 API technical report 17ATR2[19] recommended a method for predicting and avoiding failure of the PA11 liner by monitoring the molecular weight through the inherent viscosity corrected for concentration of additives (CIV) in offshore commercial PA11 P40TLO grade. A CIV of 1.05 dL/cm3 was considered the onset of possible failure in the API technical report 17ATR2 based on field experience. A CIV value of 1.20 was proposed as the time when careful M_m monitoring is needed.

For the past 15 years, molecular weight of PA11 has since been monitored to predict the transition from ductility to brittleness. Given the importance that M_m degradation has on the performance properties of PA11, the effect of environment and resulting kinetics have been extensively studied[14-16, 18, 20-23]. The correlated effects that the 3 components of offshore PA11 have on the mechanical performance of PA11 (the BBSA plasticizer, crystalline regions, and the M_m) have

been recently recognized and empirically studied by Mazan, Jorgensen [5, 6, 24]. Most notable is the recent investigation by Okamba-Diogo, Richaud [8] of crystallinity, morphology and molecular weight of PA11 during embrittlement.

Okamba-Diogo, Richaud [8] explored the relationship between the crystallinity and molecular weight for PA11 and the related embrittlement or decreasing ultimate strain. They used oxidation to degrade the molecular weight of PA11 at 110 ˚C, and used stabilizers to alter the rate of M_m degradation. Thereby they decouple the crystallinity and molecular weight effects. They observed the transition from relative ductility to brittleness in oxidized PA11, and ultimately embrittlement of PA11. Oxidation of stabilized PA11 took 67 days at 110 ˚C to reach embrittlement in air, four times the time it took for the un-stabilized PA11 to encounter the ductile-brittle transition. They report that the time to embrittlement correlated with the time to decreasing average molecular weight for both stabilized and unstabilized PA11.

This work of Okamba-Diogo, Richaud [8] represents the state of the art for understanding the oxidation mechanism for embrittlement in PA11. It is interesting to note in their work, PA11 is deduced to have a critical number average molecular weight of 10 kDa and a proportionality of 5 to the entanglement molecular weight, estimated to be 2 kDa. This correlates to a well established relationship to embrittlement in glassy polymers[2]. In their paper, PA11 showed a critical interlamellar distance of 6.5 nm at the onset of brittleness, which was similar to previous findings for polyethylene, polyoxymethylene and polypropylene[7, 9, 11].

This brittleness inflection point of the interlamellar distance was established via small angle x-ray scattering. This semicrystalline critical interlamellar distance at the ductile-brittle transition for PA11 was similar to previous findings in these semicrystalline carbon chain polymers. This correlation to semicrystalline polymers suggests that PA11's critical molecular weight (M_C) ratio to molecular weight of chain entanglements (M_e) might be as high as 50 as observed in these carbon backbone polymers. Since the deduced ratio was 5, instead PA11 is not well described by the M_C/M_e ratio of 50 for semicrystalline polymers. Thus the question of the universality of lamellar distance and the M_C/M_e ratio remains. Okamba-Diogo, Richaud [8] conclude that the amorphous region thickness, in the PA11, is a crucial parameter for determining whether the PA11 is brittle or ductile. This important finding gives insight into the mechanism resulting in PA11's embrittlement.

Small organic acid hydrolysis aging of PA11 accelerates the M_m degradation at 3 to 4 times the rate of water hydrolysis degradation[16]. By acid accelerating the hydrolysis reaction of PA11 at elevated temperature, less time elasped and thermal annealing was avoided as PA11 acheived a lower M_m and with lower crystallinity content. This work used a commercial PA11 and accelerated the M_m degradation such that thermal annealing was preempted compared to the slower aging in pH 7 water. Low molecular weights were achieved with low crystallinity and unexpected high ultimate strain. By accelerating the M_m degradation, the challenge of making semi-crystalline PA11 of the same M_m but different crystallinity was overcome. The

crystalline content and molecular weight of a semicrystalline polymer are known to influence the polymer performance properties[25]. The research herein examines the relationship of the crystalline content and the mass average molecular weight to the onset of the ductile-brittle transition and predicting embrittlement of PA11.

4.2 Experimental

Two samples of commercial offshore grade PA11, extruded P40TLO, were used in this study: P1 and P2. P1 was an offshore grade PA11 containing BBSA plasticizer at 12% by weight, a starting mass average molecular weight (M_m) of 100 ± 10 kDa, a crystallinity content of 31 J/g, or 16 % where the 100 % H_{fus} for PA11 is 189 J/g[26], and an ultimate strain of 500 ±50 %. P2, also P40TLO, had 12 wt% N - n - Butylbenzenesulfonamide, a starting M_m of 80 ±5 kDa, a crystallinity of 35 J/g or 19%, and an ultimate strain of 370 ±30 %. P1 was the thicker sample, 2 ±0.5 mm compared to sample P2, 0.3 ±0.02 mm.

Both P1 and P2 were formed into dogbone tensile test specimens and mechanical tests were performed on a MTS at a rate of 6.35 mm/min.

The PA11 dogbones were immersed in deionized water, acetic, or butanoic acid solution at 6.3×10^{-2} M and aged at 120 °C over a period of 4, 2, and 0.5 months respectively to accelerate aging and M_m degradation. Ace #40 high pressure rated glass tubes with Teflon plugs were used as containment vessels. Before sealing the pressure tube, oxygen was removed by sparging the aqueous solution with argon in-situ to achieve a concentration below 50 ppm.

A TA Instruments Q20 Differential Scanning Calorimeter (DSC) was used to measure the crystalline content of PA11. The ramp rate of 3 $^{\circ}C/_{min}$ was used to heat the samples under nitrogen from 40 to 220 $^{\circ}C$ with peak integration limits of 140 to 200 $^{\circ}C$.

To measure mass average molecular weight, M_m, a system of multiple in-line size exclusion chromatography (SEC) columns (Shodex HFIP-LG, HFIP-805, and HFIP-803) with a Wyatt miniDAWN multi-angle laser light scattering (MALLS) detector and a Wyatt Optilab 803 dynamic refractive index detector was used. The details of these measurements can be found elsewhere[16] and on page 14. The measured M_m values have a 6 % error margin as determined by the standard deviation divided by the mean for six consecutive M_m measurements on a single solution of PA11.

4.3 Results and Discussion

Figure 4-1 shows that low molecular weight acids significantly accelerate the hydrolysis aging of PA11[16]. This was used to achieve lower molecular weights faster than deionized water aging at the given temperature. By utilizing this rapid acetic and butanoic hydrolysis and decrease in the molecular weight, the PA11 samples at 120 ˚C reach the same M_m as the water aged PA11 in ½ and ¼ the time, Figure 4-1. In 9 days the butanoic acid accelerated hydrolysis brought PA11 from 100 kDa to 36 kDa, a rate of 7 $^{kDa}/_{day}$, compared with the 40 days required for water hydrolysis to reach the equilibrium M_m of 36 kDa at 120 ˚C, 1.6 $^{kDa}/_{day}$. A kinetic increase in crystallinity due to the formation of the degraded short chains for water aged samples and the acid aged chains is observed as the chains approach the equilibrium M_m. Ultimate strain, the macroscopic mechanical property of interest, decreases with the M_m over time and they increase in crystallinity. For water aged PA11 at M_{me} the decrease in ductility occurs because annealing slowly increases the crystallinity with time once near the equilibrium molecular weight[27].

The acetic acid aged PA11 enters a different equilibrium molecular weight of 18 kDa compared to 36 kDa for water. Once in the equilibrium M_m, the increasing crystallization through thermal annealing also becomes proportional to decreasing ultimate strain, Figure 4-2.

For butanoic acid aged PA11, the equilibrium molecular weight is below

18 kDa, but PA11 aged in butanoic acid became brittle before the equilibrium molecular weight was reached. Particularly interesting was that the degradative brittleness occurs at the same degree of crystallinity through chemicrystallization process in butanoic acid aged PA11 as annealing at the equilibrium M_m for water aged PA11, the dark blue symbols in Figure 4-1.

Figure 4-2 illustrates the two ways to change or increase the crystallinity as measured by the enthalpy of fusion (ΔH_{fus}), the degradation induced thermodynamic chemicrystallization and the annealing processes. The degradation chemicrystallization process occurs as the shortened polymer chains align more quickly and are absorbed onto and thickened the lamellar regions. The classic slower thermal annealing occurs once at the equilibrium M_m, where temperature determines the molecular mobility, and in time, this mobility results in formation of poorly aligned lower temperature ΔH_{fus} melting crystalline regions.

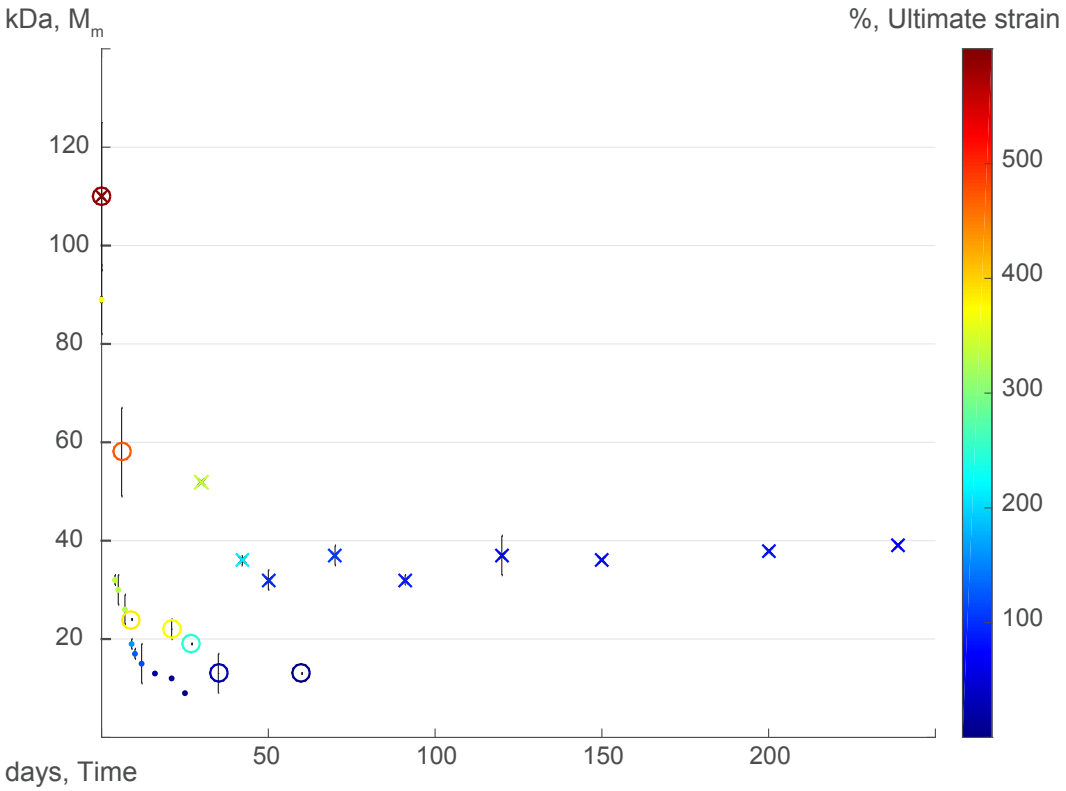

Figure 4-1: Aging M_m over time for P40TLO PA11 in water, acetic and butanoic accelerated aging environments; color is the ultimate strain where red is ductile and blue is brittle. Averaged experimental data of X-water; O-acetic acid aged; and •-butanoic acid aged, and error bars are the standard deviation calculated from 3 or more data points.

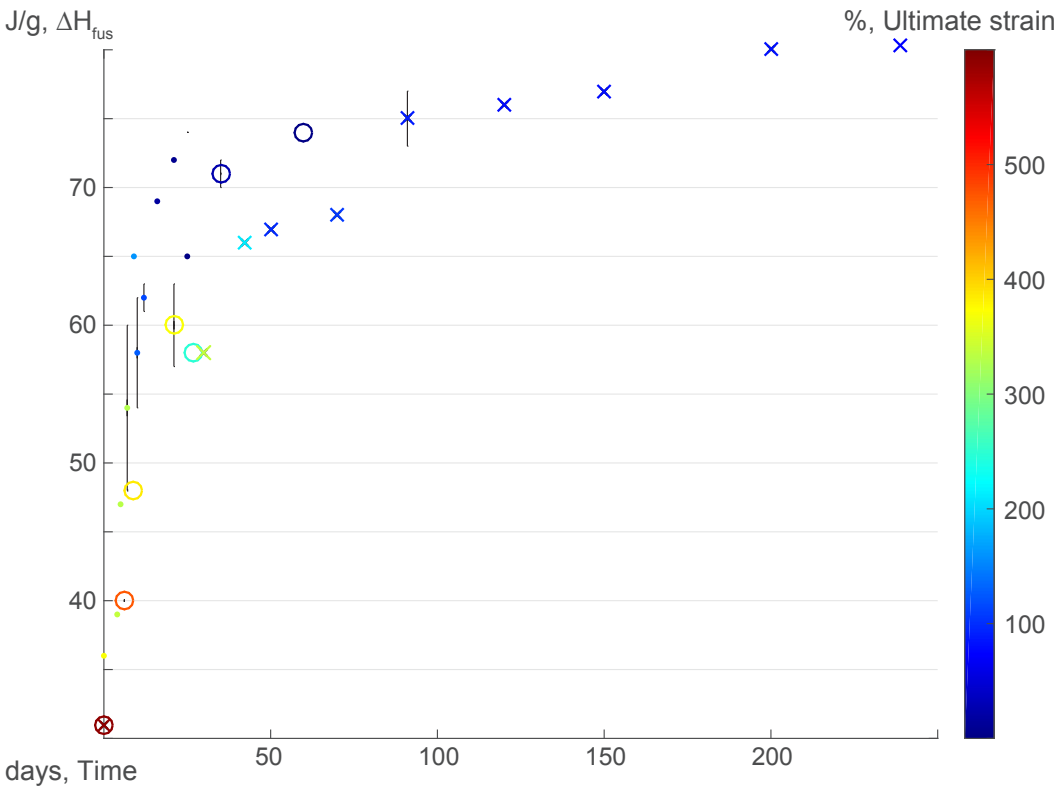

Figure 4-2: Crystallinity over time, with ultimate strain color overlay where red is ductile and blue is brittle. Averaged experimental data of X-water; O-acetic acid aged; and •-butanoic acid aged, and error bars are the standard deviation calculated from 3 or more data points.

Rapid aging preempts annealing crystallization and results in chemicrystallization. Figure 4-2 shows very fast crystallinity increases that are spontaneous and thermodynamically favored with the rapidly decreasing M_m of the acid aged PA11. Increases in crystallinity at a rate of 6.5 $^{J}/_{g}/_{day}$ for butanoic, 3.2 $^{J}/_{g}/_{day}$ for acetic aging and 1.8 $^{J}/_{g}/_{day}$ for water aging during their approach to an equilibrium M_m. These rates of increase compare well with the initial decreasing M_m rates: 7 $^{J}/_{g}/_{day}$ for butanoic, 3.6 $^{kDa}/_{day}$ for acetic, and 1.6 $^{kDa}/_{day}$ for water aged of Figure 4-1.

Beyond the initial rapid increase in the crystallinity and decrease in M_m, the water aged samples spend extended time, 160 days, at the M_{me}. This results in the slower annealing increase of the ΔH_{fus} with a modest 10 to 20 % decrease in the ultimate strain. But once above a ΔH_{fus} of 70 $^{J}/_{g}$, regardless of the crystallization process, both water and acid accelerated aged PA11 samples are in the brittle regime. Thus, at a ΔH_{fus} of 70 $^{J}/_{g}$ brittleness is expected at molecular weights below 45 kDa. Figure 4-2 and Table 4-1 show the onset of the transition from ductility to brittleness began at 55 $^{J}/_{g}$, and brittleness occured at 70 $^{J}/_{g}$, a region where the ultimate strain was brittle. Equally important, the differing ultimate strain values at different crystallinities given the same M_m showed that the crystallinity was of fundamental importance to embrittlement, but alone did not govern the ultimate strain of PA11.

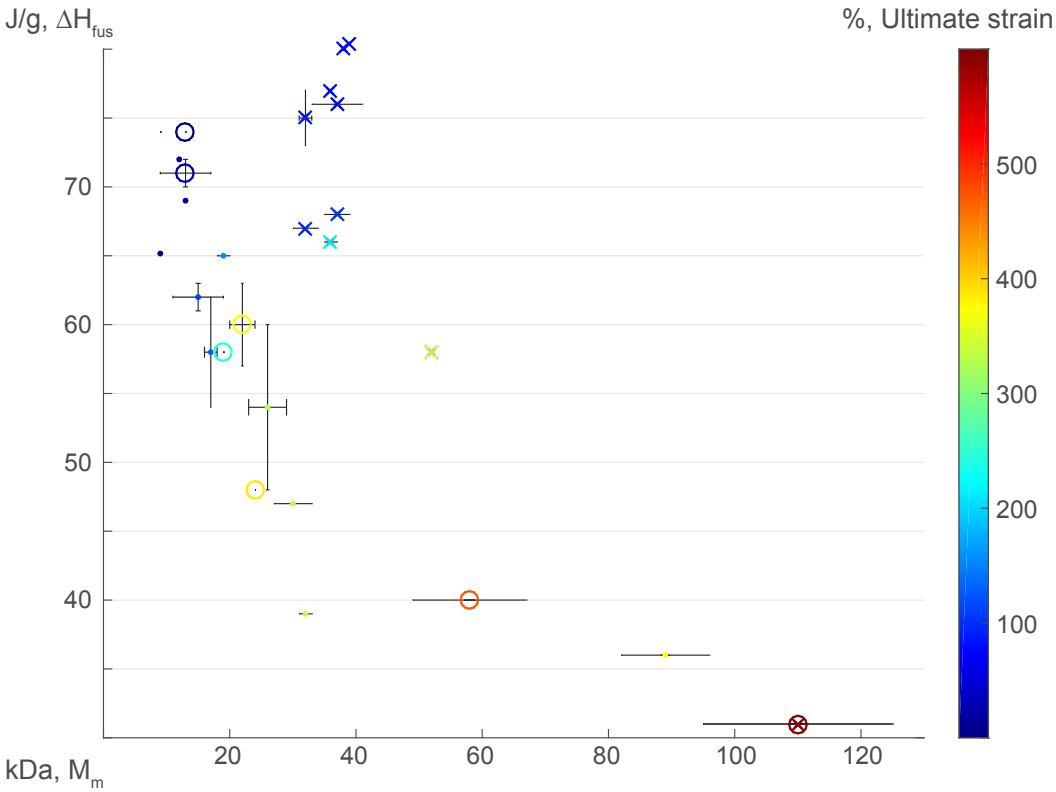

Figure 4-3: ΔH_{fus} as a function of the M_m during aging. Color is the ultimate strain where red is ductile and blue is brittle. Averaged experimental data of X-water; O-acetic acid aged; and •-butanoic acid aged, and error bars are the standard deviation calculated from 3 or more data points.

Figure 4-3 showed in greater detail the suggested relationship of the decreasing M_m and ΔH_{fus} to the ultimate strain, the color values. The onset at 35 kDa for both acid accelerated systems chemicrystallization controlled crystallization had an apparent linear relationship with decreasing M_m. Figure 4-3 showed that the rapid chemicrystalline growth, preemptive of the slower annealing crystalline process, followed the same linear slope at the onset of 35 kDa for both acid accelerated systems; a slope of 1.6 $^{J}/_{g/kDa}$. This relationship of the molecular weight to chemicrystallization and lamellar thickening increasing the crystallinity has been previously shown[9-12, 28-33].

Time at a fixed temperature and fixed M_m results in thermal annealing of PA11. The much longer 40 plus days aging time at 120 ˚C in water versus 9 days in acetic and 4 days in butanoic, resulted in increased crystallinity during further aging at the equilibrium M_m. Due to the lack of thermal annealing, the acid accelerated aged PA11 had greater than 200 % ultimate strain, at 20 kDa as it approached its equilibrium M_m. This ductility at 20 kDa is 15 kDa below the molecular weight of 35 kDa where water aged PA11 had a similar ductility and both approach the ductile-brittle phase transition. With time the water aged PA11 at much higher M_ms had an ultimate strain below 100 % with M_m between 35 and 40 kDa as expected from thermal annealing.

The longer aging time beyond the 40 days in water, where the equilibrium molecular weight of 35 kDa M_{me} is achieved, results in the annealing driven crystallinity increases during 200 days aging at 120 ˚C. There are small

decreases in ultimate strain with increasing crystallinity from 65-81 J/g in the water aged samples at the equilibrium molecular weight of 35 kDa. A maximum crystallinity was achieved at 81 J/g, and an ultimate strain of 75 % was observed. It might be expected that the aged PA11 samples at higher ΔH_{fus} values such as 81 J/g, would degrade their ultimate strain further with decreasing M_m.

The focus of Figure 4-4 was ultimate strain as a function of M_m. For both acetic and butanoic accelerated aging, ultimate strains greater than 300 % are possible at M_m values in the range of 30 ±5 kDa. The butanoic 4 days aged and 5 days aged showed 365% and 332% ultimate strain at 35 kDa and 30 kDa respectively. This was in direct comparison to the water aged samples from day 42 to 240 days, 35 ±5 kDa with ultimate strain ranging from 75 to 100 %. That was a 200 % greater ultimate strain at the same molecular weight. Overall, the acid accelerated samples showed decreasing M_m with unexpectedly high ultimate strain values at M_ms far below 30 kDa where water aged PA11 is at equilibrium M_m (M_{me}) and in the ductile to brittle transition region. After 250 days of aging in water, the crystallinity for water aged 35 kDa PA11 is 81 J/g, 15 J/g beyond a proposed critical crystallinity of 66 ±3 J/g, and where the ultimate strain remained semi-ductile below 100%, at 80% ultimate strain.

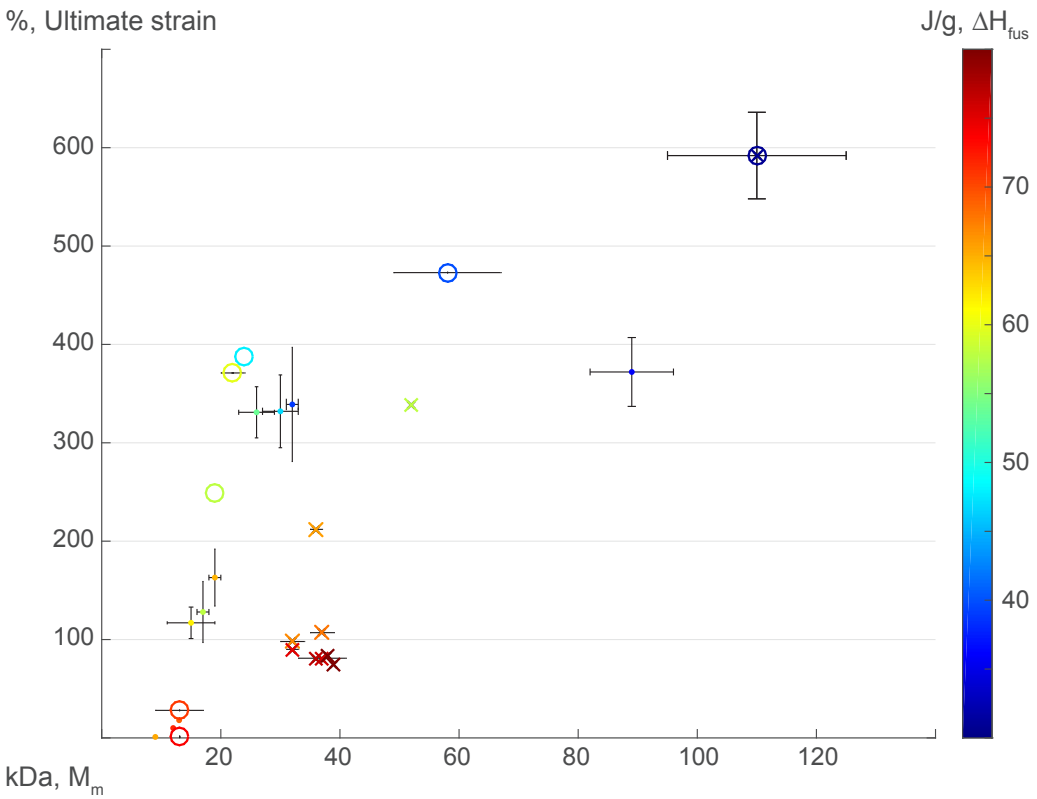

Figure 4-4: Ultimate strain as a function of molecular weight. Color is the crystallinity measured through ΔH_{fus} in J/g strain where high crystallinity and blue low crystallinity. Averaged experimental data of X-water; O-acetic acid aged; and •-butanoic acid aged, and error bars are the standard deviation calculated from 3 or more data points.

Chain entanglements in the amorphous phase are the key to ductility and an ultimate strain greater than 50 %. The amorphous regions are between the crystalline regions and decrease with increases in crystallinity[26]. Thus increased crystallinity and decreased molecular weight both result in a reduction of entropic molecular chain entanglement. That is the cause of embrittlement in PA11. Previously the onset of embrittlement has been correlated to the distance between crystalline regions using small angle x-ray diffraction[8]. The results in Figure 4-4 show that a critical crystallinity of PA11, ΔH_{fus} at 66 ±3 $^{J}/_{g}$ can also be used to indicate the ductile-brittle transition onset of PA11, independent of M_m.

Focusing on the region of embrittlement, Figure 4-5 displays how for both water aged samples and acid accelerated aged samples, crystallinity is correlated with decreasing ultimate strain. The figure shows that higher M_m values have semi-ductile behavior, while lower M_m shows brittle PA11 for similar ΔH_{fus}. At a M_m range of 35 ±5 kDa for water and 18 ±3 kDa for acid aging, Figure 4-5 shows different areas of embrittlement for PA11 based on rate of M_m degradation. At the higher crystallinity values of the water aged PA11, 70-81 $^{J}/_{g}$, the ultimate strain is 75 to 107 %. This semi-ductile characteristic can be attributed to the higher value of M_m, 35 ±5 kDa. This result compares with the slightly lower ΔH_{fus}, 68 – 74 $^{J}/_{g}$, acid accelerated results that are brittle with less than 50 % ultimate strain, and attributed to the lower M_m value of 18 kDa.

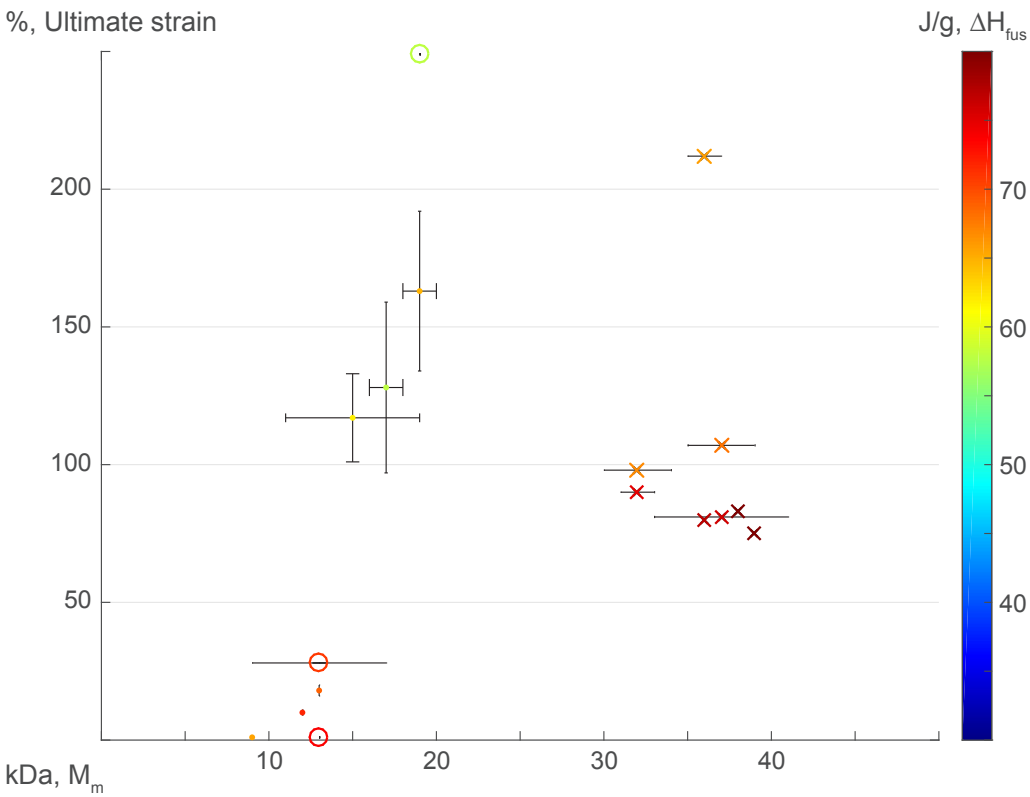

Figure 4-5: A closer look at the embrittlement region; color is the ultimate strain where red is ductile and blue is brittle. Averaged experimental data of X-water; O-acetic acid aged; and •-butanoic acid aged, and error bars are the standard deviation calculated from 3 or more data points.

At a molecular weight as low as 20 kDa, the acid aged PA11 was ductile, and had a 250 % ultimate strain, with a crystallinity of 50 J/g for the acid aged PA11, less than the proposed critical crystallinity value of 66 J/g. For the rapid acid aged, the brittle phase transition occurs at lower molecular weights at 66 J/g crystallinity content.

The size of the amorphous phase is key to ductility and high ultimate strains as the crystalline regions are rigid. As the crystallites develop in the PA11 matrix, the molecular volume of the amorphous chain entanglement regions are reduced in size. This was the molecular basis for the effect that crystallinity had on ultimate strain, ductility.

The molecular weight provides the initial key information required to predict the embrittlement of PA11, as is well known. But the crystallinity content becomes increasingly influential with annealing and during the M_m approach to 35 kDa. When the crystallinity was low, at a heat of fusion below 60 J/g , a M_m as low as 20 kDa remains ductile. Conversely when the M_m was 38 kDa with a 68 J/g ΔH_{fus}, PA11 was at the onset of the ductile brittle phase transition. Once PA11 has reached the equilibrium M_m at 120 ˚C, the brittleness of the PA11 progresses with a slow increase in crystallinity due to annealing.

These experimental results on the correlated effect of crystallinity and molecular weight on embrittlement suggest there is both a critical crystallinity of 70 J/g, and a critical molecular weight of 16 ±3 kDa. Together these experimental

critical embrittlement values can be used to model and predict the ultimate strain behavior of PA11 based on the inter-related molecular properties of M_m and ΔH_{fus}, as they change over time, Equation 4-1. The best fit parameters for Equation 4-1 were: ε_0 =491, the starting ultimate strain value; h_c =55 J/g, the critical ΔH_{fus}; h_0 =31, the starting ΔH_{fus}; h is the ΔH_{fus}; m is the M_m; m_c =14, kDa the critical M_m; A =0.24, the fitting coefficient for M_m effect on ultimate strain; and B =0.88, the fitting coefficient of ΔH_{fus}, effect on ultimate strain. With the known starting PA11 ultimate strain, the ratio of critical values to current values of molecular M_m and ΔH_{fus} properties, the ultimate strain can be predicted and monitored with greater accuracy, precision, and understanding. Use of Equation 4-1 is explored and evaluated in Figure 4-6.

Equation 4-1:

$$\varepsilon = \varepsilon_0\left(1 - A\frac{m_c}{m} - B\,\frac{h_c - h - h_0}{h_c}\right)$$

Matlab fitting software was used to fit the model to the data. Starting values were used in the least-squares fitting routine to minimize the least squares fit, and solved for each value: ε_0, m_c, h_c, h_0, A, and B; with an R^2 of 0.82. Table 4-1 lists the starting values, range, and fit results for each value

Table 4-1: The input values and range limits that were used in a non-linear east squares fit of Equation 4-1 to the experimental data are listed. The fitted best fit values for each parameter are listed, with an R^2 of 0.82.

Equation parameters	Input value	Range	Best fit value
ε_0 (%)	550	±100	491
A	0.5	±0.5	0.24
m_c (kDa)	21	±10	14
B	0.5	±0.5	0.88
h_c (J/g)	70	±20	55
h_0 (J/g)	36	±6	31

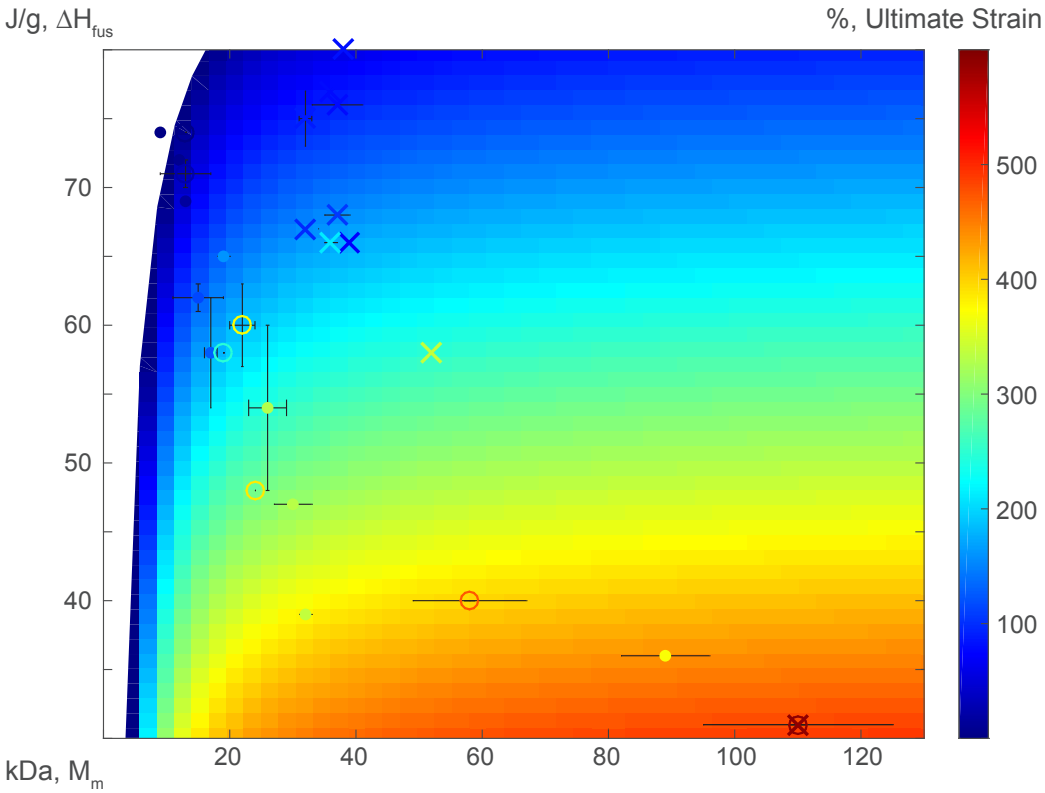

Figure 4-6: Model predicted color coded ε for a given M_m and ΔH_{fus}. Averaged experimental data of X-water; O-acetic acid aged; and •-butanoic acid aged overlayed on the model predictions. Error bars are the standard deviation calculated from 3 or more data points.

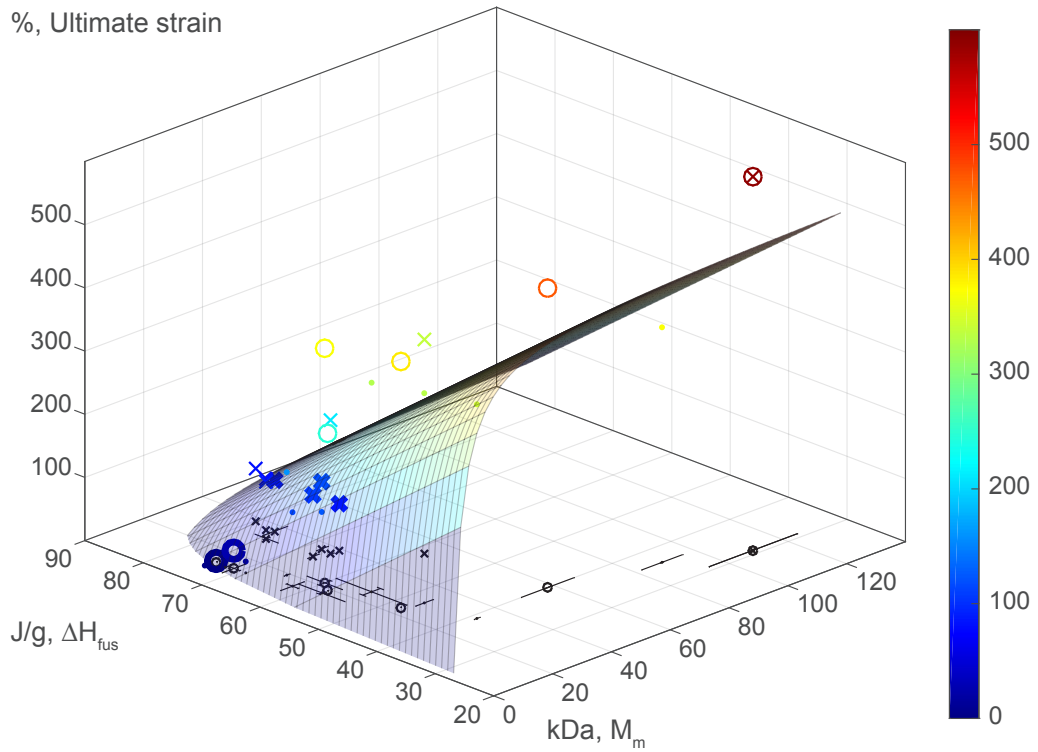

Figure 4-7: 3-D plot: Model predicted color coded ε for a given M_m and ΔH_{fus}. Averaged experimental data of X-water; O-acetic acid aged; and •-butanoic acid aged fit to the model. Error bars are the standard deviation calculated from 3 or more data points.

4.4 Summary

Table 4-2 highlights the contrasting experimental results that were observed. From these results for both the acid accelerated and water aged systems, the linear increase of ΔH_{fus} with decreasing M_m initiated at the previously determined critical M_m of 35 kDa describes the transition from ductile to semi-ductile to brittle.

Table 4-2: Summary of key observations.

Observation #	kDa, **M_m**	J/g **ΔH_{fus}**	%, **ε**
1	110	31	592
2	35	39	350
3	35	65 - 81	107 - 75
4	20	58	250
5	10 - 15	70	< 50

In summary, these experimental results showed a ductile PA11 down to a degraded critical M_m of 16 ±3 kDa with low crystallinity. For the crystallinity, a critical embrittlement value of 70 J/g could be observed in Figure 4-3, with a transition to brittleness starting at 66 J/g. That crystallinity and molecular weight both effect the mechanical or ultimate strain properties is textbook[25], but the ability to decouple the effect of total crystallinity from the effect of molecular weight has now been achieved by studying PA11 degradation at different rates but the same temperature. The description of how crystallinity and molecular weight were correlated with the ultimate strain was based on the combined results of the three aging studies. These three studies decoupled the correlated effects of the molecular properties of crystallinity and molecular weight and their influence on

the ultimate strain of PA11. This resulted in development of an empirical model to predict the ultimate strain as a function of the molecular weight and crystallinity for PA11, Equation 4-1.

The modeling approach, while empirical, is based on aging data and has an appropriate application in the field use of PA11. Future work may include more research to understand how the α and γ crystalline forms of PA11 can effect the macroscopic mechanical properties of PA11. This would create a more detailed model to understand and predict the mechanical behaviors of semicrystalline polymers such as PA11, based on the additional property of crystal structure.

4.5 Conclusion

To understand the ductile-brittle transition region of PA11, the rate of M_m degradation was varied by water and acid accelerated aging and the correlated effects of M_m and crystallinity upon the ultimate strain of PA11 were decoupled.

The results showed that there is a critical crystallinity content of PA11 that determines the onset M_m of the ductile-brittle phase transition (66 J/g) and when the crystalline content goes beyond 70 J/g, brittleness ensues. M_m governs the ductility until the equilibrium M_m is reached. In water aging, the approach to embrittlement progresses slowly with increasing crystallinity once degraded to the constant equilibrium molecular weight. When PA11 has reached the equilibrium M_m, the brittleness of the PA11 progresses with increasing crystallinity due to annealing.

In this study, a M_m range of 35 ±5 kDa for water and 16 ±3 kDa for acid accelerated are the two areas of embrittlement for PA11. For the high crystallinity values of the water aged PA11 at the 35 kDa equilibrium M_m and ΔH_{fus} of 70-81 J/g, the ultimate strain remained in the ductile to brittle transition, below 100 % and greater than 50 %. This semi-ductile characteristic can be attributed to the relatively high M_m of 35 ±5 kDa compared with acid aged PA11 that is ductile down to 18 ±3 kDa with ΔH_{fus}, 58 J/g. Acid aged PA11 becomes brittle with less than 50 % ultimate strain and is attributed to the combination of the lower M_m, below 15 kDa, with higher crystallinity, ΔH_{fus} of 68 – 74 J/g.

For PA11, the ΔH_{fus} along with M_m measurements are needed to monitor and predict the conditions for the onset of the ductile to brittle transition and when embrittlement occurs. The proposed model based on the three aging experiments can be used to predict the ultimate strain of PA11 during aging and during in-situ use in the field, by measuring both the crystallinity and molecular weight.

4.6 References

[4_1] CRETON, C., KRAMER, E. J., BROWN, H. R. & HUI, C. Y. 2002. Adhesion and fracture of interfaces between immiscible polymers: From the molecular to the continuum scale. Molecular Simulation Fracture Gel Theory, 156, 53-136.

[4_2] SHA, Y., HUI, C. Y., RUINA, A. & KRAMER, E. J. 1995. CONTINUUM AND DISCRETE MODELING OF CRAZE FAILURE AT A CRACK-TIP IN A GLASSY POLYMER. Macromolecules, 28, 2450-2459.

[4_3] DONALD, A. M. & KRAMER, E. J. 1982. EFFECT OF MOLECULAR ENTANGLEMENTS ON CRAZE MICROSTRUCTURE IN GLASSY-POLYMERS. Journal of Polymer Science Part B-Polymer Physics, 20, 899-909.

[4_4] BROWN, H. R. 1991. A MOLECULAR INTERPRETATION OF THE TOUGHNESS OF GLASSY-POLYMERS. Macromolecules, 24, 2752-2756.

[4_5] MAZAN, T., JORGENSEN, J. K. & ECHTERMEYER, A. 2015b. Aging of polyamide 11. Part 2: General multiscale model of the hydrolytic degradation applied to predict the morphology evolution. Journal of Applied Polymer Science, 132, 10.

[4_6] MAZAN, T., JORGENSEN, J. K. & ECHTERMEYER, A. 2015c. Aging of polyamide 11. Part 3: Multiscale model predicting the mechanical properties after hydrolytic degradation. Journal of Applied Polymer Science, 132, 11.

[4_7] FAYOLLE, B., AUDOUIN, L. & VERDU, J. 2004. A critical molar mass

separating the ductile and brittle regimes as revealed by thermal oxidation in polypropylene. Polymer, 45, 4323-4330.

[4_8] OKAMBA-DIOGO, O., RICHAUD, E., VERDU, J., FERNAGUT, F., GUILMENT, J. & FAYOLLE, B. 2016. Investigation of polyamide 11 embrittlement during oxidative degradation. Polymer, 82, 49-56.

[4_9] FAYOLLE, B., COLIN, X., AUDOUIN, L. & VERDU, J. 2007. Mechanism of degradation induced embrittlement in polyethylene. Polymer Degradation and Stability, 92, 231-238.

[4_10] FAYOLLE, B. & VERDU, J. 2011. Radiation aging and chemi-crystallization processes in polyoxymethylene. European Polymer Journal, 47, 2145-2151.

[4_11] FAYOLLE, B., RICHAUD, E., COLIN, X. & VERDU, J. 2008. Review: degradation-induced embrittlement in semi-crystalline polymers having their amorphous phase in rubbery state. Journal of Materials Science, 43, 6999-7012.

[4_12] FAYOLLE, B., VERDU, J., PICCOZ, D., DAHOUN, A., HIVER, J. M. & G'SELL, C. 2009. Thermooxidative Aging of Polyoxymethylene, Part 2: Embrittlement Mechanisms. Journal of Applied Polymer Science, 111, 469-475.

[4_13] JARRIN, J., DRIANCOURT, A., BRUNET, R. & PIERRE, B. 1998. Durability of polyamide 11 for offshore flexible pipe applications. MERL Oilfield engineering with polymers. London, UK.

[4_14] GLOVER, A. J. M. 2011. Characterization of PA-11 Flexible Pipe Liner Aging in the Laboratory and in Field Environments Throughout the World. Doctor of Philosophy Dissertation, The College of William and Mary.

[4_15] MEYER, A., JONES, N., LIN, Y. & KRANBUEHL, D. 2002. Characterizing and Modeling the Hydrolysis of Polyamide-11 in a pH 7 Water Environment. Macromolecules, 35, 2784-2798.

[4_16] HOCKER, S., RHUDY, A. K., GINSBURG, G. & KRANBUEHL, D. E. 2014. Polyamide hydrolysis accelerated by small weak organic acids. Polymer, 55, 5057-5064.

[4_17] ROMAO, W., CASTRO, E. V. R., FILHO, E. A. S., GUIMARAES, R. C. L., SILVA, A. L. N., TEIXEIRA, S. C. S., DE PAOLI, M.-A. & DE SENA, G. L. 2009. Ageing of polyamide 11 used in the manufacture of flexible piping. Journal of Applied Polymer Science, 114, 1777-1783.

[4_18] DOMINGOS, E., PEREIRA, T. M. C., FILGUEIRAS, P. R., BUENO, M. I. M. S., DE CASTRO, E. V. R., GUIMARAES, R. C. L., DE SENA, G. L., ROCHA, W. F. C. & ROMAO, W. 2012. Monitoring the polyamide 11 degradation by thermal properties and X-ray fluorescence spectrometry allied to chemometric methods. X-Ray Spectrometry, 42, 79-86.

[4_19] API 2003. Technical Report 17TR2, The Ageing of PA-11 in Flexible Pipes. Washington, DC: American Petroleum Institute.

[4_20] BERGER, J., FRANOSCH, J., SCHUETT, C., DOWE, A. & AG, E. I. 2011. The Aging of Offshore Polyamides under Services Conditions in Subsea Applications. Offshore Technology Conference. Rio de Janeiro, Brazil.

[4_21] JACQUES, B., WERTH, M., MERDAS, I., THOMINETTE, F. & VERDU, J. 2002. Hydrolytic ageing of polyamide 11. 1. Hydrolysis kinetics in water. Polymer, 43, 6439-6447.

[4_22] MERDAS, I., THOMINETTE, F. & VERDU, J. 2003. Hydrolytic ageing of polyamide 11—effect of carbon dioxide on polyamide 11 hydrolysis. Polymer Degradation and Stability, 79, 419-425.

[4_23] PETHRICK, R. A., BANKS, W. M. & BRODESSER, M. 2014. Ageing of thermoplastic umbilical hose materials used in a marine environment II - Nylon. Proceedings of the Institution of Mechanical Engineers Part L-Journal of Materials-Design and Applications, 228, 63-88.

[4_24] MAZAN, T., BERGGREN, R., JORGENSEN, J. K. & ECHTERMEYER, A. 2015a. Aging of polyamide 11. Part 1: Evaluating degradation by thermal, mechanical, and viscometric analysis. Journal of Applied Polymer Science, 132, 11.

[4_25] ALLCOCK, H. R., LAMPE, F. W. & MARK, J. E. 2003. Contemporary Polymer Chemistry, Lebanon, Indiana USA, Prentice Hall.

[4_26] ZHANG, Q. Z., MO, Z. S., LIU, S. Y. & ZHANG, H. F. 2000. Influence of

annealing on structure of Nylon 11. Macromolecules, 33, 5999-6005.

[4_27] VOIGT-MARTIN, I. G. & MANDELKERN, L. 1984. A quantitative electron microscopic study of the crystallite structure of molecular weight fractions of linear polyethylene. Journal of Polymer Science, 22, 1901-1917.

[4_28] DUDIC, D., KOSTOSKI, D., DJOKOVIC, V. & STOJANOVIC, Z. 2000. Recrystallization processes induced by accelerated ageing in isotactic polypropylene of different morphologies. Polymer Degradation and Stability, 67, 233-237.

[4_29] MATHUR, A. B. & MATHUR, G. N. 1982. THERMO-OXIDATIVE DEGRADATION OF ISOTACTIC POLYPROPYLENE FILM - STRUCTURAL-CHANGES AND ITS CORRELATION WITH PROPERTIES. Polymer, 23, 54-56.

[4_30] VIEBKE, J., ELBLE, E., IFWARSON, M. & GEDDE, U. W. 1994. DEGRADATION OF UNSTABILIZED MEDIUM-DENSITY POLYETHYLENE PIPES IN HOT-WATER APPLICATIONS. Polymer Engineering and Science, 34, 1354-1361.

[4_31] YUE, C. Y. & MSUYA, W. F. 1990. CHANGES IN YIELD IN POLYPROPYLENE OF DIFFERENT MORPHOLOGY CAUSED BY PHYSICAL AGING. Journal of Materials Science Letters, 9, 985-988.

[4_32] RABELLO, M. S. & WHITE, J. R. 1997. Crystallization and melting behaviour of photodegraded polypropylene .1. Chemi-crystallization. Polymer, 38, 6379-

6387.

[4_33] PAPET, G., JIRACKOVAAUDOUIN, L. & VERDU, J. 1987. DIFFUSION CONTROLLED RADIOCHEMICAL OXIDATION OF LOW-DENSITY POLYETHYLENE .1. DEPTH DEPENDENCE OF MORPHOLOGICAL-CHANGES. Radiation Physics and Chemistry, 29, 65-69.

4.7 Supplementary Data

Table 4-3: Molecular weight (kDa), crystallinity (J/g) and ultimate strain (%) data collected for aging in water, acetic, and butanoic acid at 120 ˚C, as discussed in the text.

Sample	Day #	M_m (kDa)	ΔH_{fus} (J/g)	ε (%)
Unaged P1	0	129, 121, 96, 108, 96	31	573, 583, 665, 548
P2	0	77, 97, 81, 78, 93, 95, 103, 87	36	331, 355, 333, 388, 380, 359, 461, 413, 369, 357, 347, 404, 368, 345
Water aged	30	52	58	339
	42	35, 36	66	212
P1	50	30, 33	67	98
	70	35, 38	68	107
	91	31, 32	73, 76	90
	120	39, 32, 40	76	81
	150	36	77	80
	200	38	80	83
	240	39	81	75
Acetic aged	6	64, 51	40	473
	9	24	48	388
P1	21	21, 22, 24	63, 58, 60	371
	27	19, 19	58	249
	35	15, 10	70, 72	28
	60	13	74	1
Butanoic aged	4	31, 33	39	258, 395, 312, 337, 393
	5	27, 32	47	294, 367, 336
P2	7	25, 26, 22, 29	63, 51, 49, 52	304, 346, 316, 359
	9	18, 20	65	179, 180, 129
	10	18, 16, 17	56, 55, 63	146, 147, 92
	12	15, 11, 18	61, 62, 62	133, 117, 101
	16	13	69	17, 20, 17
	21	12	72, 67	9, 8, 9, 10, 11, 10
	25	9	65	1

Chapter 5

The Reduction of Hydrolytic Degradation in Polyamide-11 by the Addition of Graphene Oxide

5.1 Introduction

Polyamide-11 (PA11) is a widely used engineering polymer. PA11 comprises the pressure sheath liner in contact with the production fluid at elevated temperature and pressure in flexible hoses for underwater transport of gas, oil, and crude to offshore platforms. As such, PA11 fulfills a vital role in the global economy. Degradation and failure of these hoses has far-reaching financial and environmental implications. Currently, the molecular weight of PA11 is used to predict the operational lifetimes of the PA11 liner[1, 2] and hydrolysis of the PA11 is the mechanism for degradation in anaerobic environments such as the condition of underwater crude oil risers. Improving the properties of PA11 as a pressure sheath motivates this research on the hydrolytic degradation of graphene oxide (GO) loaded PA11: GO-PA11 polymer nanocomposite.

Polymer nanocomposites are high potential alternatives to filled polymers or polymer blends[3]. Since Usuki, Kojima [4], polymer nanocomposites have shown valuable performance property enhancements at much lower loadings than conventional glass and carbon fiber micron scale fillers; this can lead to simplified processing and innovation. Graphene is an atomic single layer of carbon, a 2-D carbon-honeycomb crystal structure with remarkable properties. It would be advantageous if graphene's properties - an extremely high modulus of 1 terapascal (TPa), an ultimate strength of 130 gigapascal (GPa), a gas impermeable honeycomb network, and superior electrical and thermal conductivity[5, 6] - could

be lent to polymers by means of creating graphene-polymer nanocomposites[3, 7-10]. The challenge is to disperse graphene as single nano-sheets into polar solvents and into the polymer matrix.

A wide interest in graphene's exceptional strength has revitalized research involving the analogous compound graphene oxide (GO). GO has nearly the same strength and barrier properties as pristine graphene, given the very high aspect ratio planar honeycomb structure. GO has the same honeycomb structure as graphene with oxygen-containing functional groups on the surface of the planar carbon. These oxygen containing functional groups are ketones, 6-membered lactol rings, alcohols, epoxides, and hydroxyl groups[11]. As a result, GO is a polar hydrophilic material compared to graphene, which is nonpolar and hydrophobic. GO, unlike graphene, can be dispersed into water and solvents[8] commonly used in polymer precursor resins or mixtures to create GO-polymer nanocomposites. Also, the oxide groups on the GO surface can be reacted with functional groups for improved dispersion and incorporation into a polymer matrix.

GO-polymer nanocomposites are easily made by exfoliating graphitic oxide into graphene oxide nanosheets (GO) using a compatible solvent in-situ with the polymer. Various methods of making graphitic oxide have been developed, starting with Brodie[12] in 1859, modified Brodie[13, 14], Staudenmaier[15], Hofmann[16], Hummers[17], modified Hummers[18], and most recently Tour[19] in 2010. Importantly, synthesis of graphitic oxide is suitable for industrial scale GO production[20, 21]. Many GO-polymer nanocomposites have been made

using polyurethanes, polyimides, polyamides, and other polymers[3, 7-10]. Properties reported to be improved by incorporating GO, functionalized GO, and functionalized graphene into polymers include: electrical conductivity[22-29], thermal conductivity[30, 31], thermal stability[22, 31-35], permeability[22-26, 29, 31-33, 36-41], and mechanical properties[22, 23, 26, 29, 31, 32, 34, 35, 38, 41-43]. Well dispersed GO nanoparticles in a polymer can change the chemical and morphological properties of the polymer, resulting in significantly improved performance properties.

In previous research on GO-PA11, Jin, Rafiq [38] extruded thermally reduced GO into commercial PA11 at loadings ranging from 1 to 30 $^{mg}/_{g}$ reduced GO-PA11. They showed that water vapor and oxygen permeation resistance of PA11 films were increased by 49 % at a 1 $^{mg}/_{g}$ loading and reported on the tensile properties of funcationalized graphene loaded PA11. Yuan, Wang [44] prepared 1.25 to 5 $^{mg}/_{g}$ GO-PA11 by in-situ melt polycondensation and discussed improved toughness and correlated changes in crystal structures that were formed when GO was loaded into PA11.

Here the hydrolytic degradation of GO-PA11 and the effect GO had on the PA11 matrix crystallization was explored.

5.2 Experimental

GO was incorporated into PA11 via in-situ melt condensation polymerization (GO-PA11). The aging of PA11 and GO-PA11 was accelerated by immersing

0.3 mm thick, 1 cm^2 samples in 15 mL of deionized water at elevated temperatures of 100 ˚C and 120 ˚C. The extent of hydrolytic degradation was measured by monitoring the change in mass averaged molecular weight (M_m) of PA11 over time. For PA11, a hydrolytic aging equilibrium molecular weight (M_{me}) was established after extended aging times in anaerobic conditions. The M_{me} is very important: if the M_{me} is above the ductile-brittle transition then PA11 can retain its toughness[1].

GO was synthesized using Hummers method[17], and dispersed in water by ultrasonication (Cole-Parmer EW-04711-40 homogenizer 750-Watt) at 35 % of max power for 30 minutes. The resulting solution of GO in water was filtered using a G4 glass fiber filter paper (Fisher Scientific) to remove unreacted graphitic particles. The GO particle water dispersion was then measured by solvent evaporation and mass to have a concentration of 0.3 mg/g. To visualize the particles, a spin processor (Laurell: WS-650Sz-6NPP-Lite) was used to apply a single layer of GO particles to a cleaved sheet of mica (Ted Pella, V5). An atomic force microscope (NT-MDT, model: NTEGRA) was used to characterize the dimensions of the GO sheets. The sheet sizes in the collected filtered GO/water dispersion were observed to be 0.3-1 μm laterally and 1 nm in height, Figure 5-1.

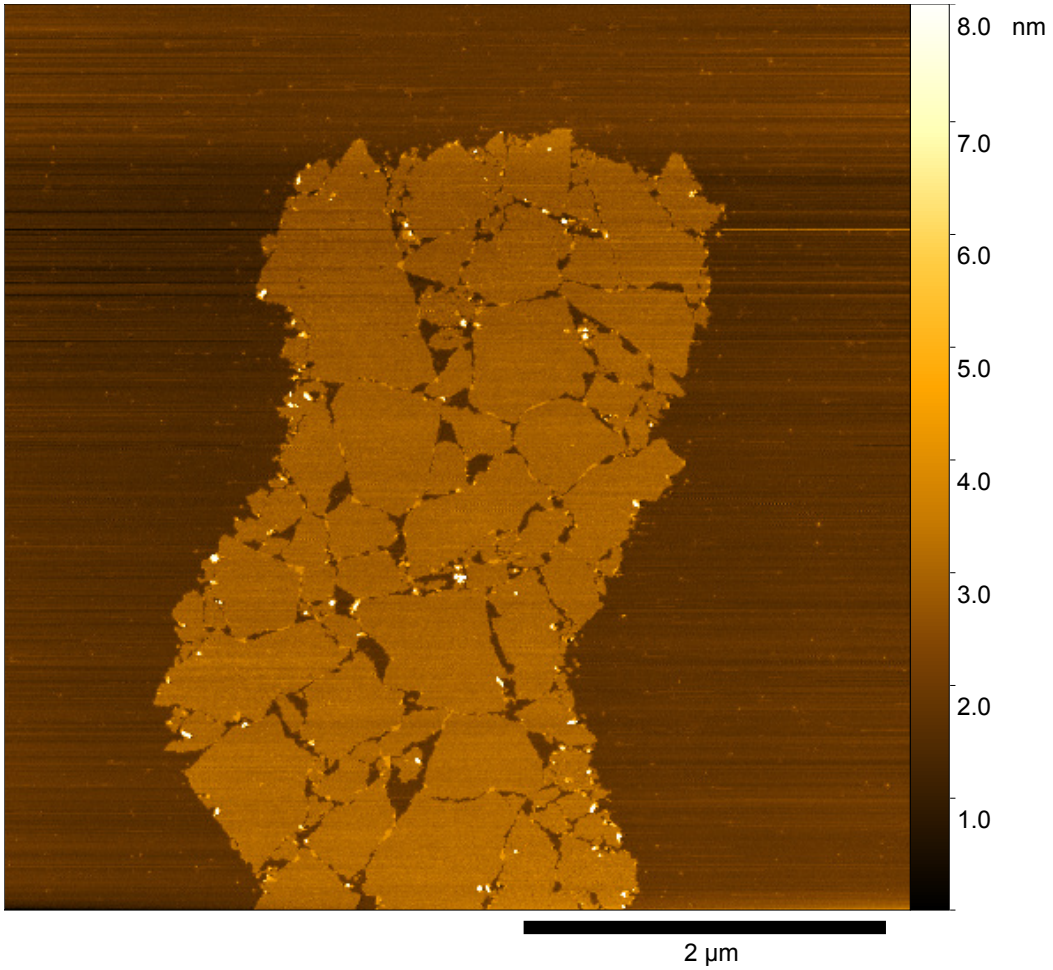

Figure 5-1: Atomic force microscope height image (from GO-water dispersion) distributed on mica.

Dry 11-aminoundecanoic acid powder was mixed with the filtered GO/water dispersion at a concentration of 1 mg and 5 mg of GO per gram of powder. Water was added to the mixture for a total volume of 15 mL. An ultrasonication tip was submerged in the mixture and sonication at 35 % of maximum power proceeded for 30 minutes with continuous stirring at 300 rpm and a maximum temperature of 30 ˚C.

A homogeneous golden-brown mixture of GO-monomer settled with a clear water supernatant. The mixture was poured into a Teflon® lined vessel and placed in an oven at 100 ˚C for 60 minutes. The result was a uniformly brown dry powder mix of GO-monomer. The GO-monomer mixture was placed under argon at 235 ˚C for 4 hours of melt condensation static polymerization with in-situ thermal reduction of GO's carbon oxygen ratio[45] to make GO-PA11; PA11 fabrication followed the same method. For convention, a concentration of 1 $^{mg}/_{g}$ GO-PA11 was termed 1-GO-PA11 and 5 $^{mg}/_{g}$ GO-PA11 was 5-GO-PA11.

Aging samples were prepared by slowly hot pressing the PA11 and GO-PA11 between two Teflon® surfaces at 250 ˚C under argon to make films of approximately 300 μm thickness. Then 1 cm^2 coupons were cut from the films and ten coupons were immersed in deionized water over a period of 3 - 4 months at elevated temperatures of 100 ˚C and 120 ˚C to accelerate aging. For containment vessels, Ace #40 high-pressure rated glass tubes with Teflon® plugs were used. Before sealing the pressure tubes, dissolved oxygen was removed by sparging the water with argon in situ for an oxygen presence below 50 ppm.

Mass average molecular weight (M_m) measurement details are on page 20. The SEC-light scattering M_m measurements in this work have a 6% instrumental error. The error was determined by the standard deviation divided by the mean for six consecutive M_m measurements on a single solution of unaged laboratory-made PA-11.

The GO-PA11/HFIP solutions were darkened by the presence of GO, indicating that HFIP is not an ideal solvent for GO. The dissolved GO-PA11 solutions were filtered through a 0.45 μm porosity Teflon filter to determine the molecular weight measurements. All visible GO in solution was filtered by the Teflon® filter. The GO diameters in the representative AFM image, Figure 5-1, were on average greater than 0.5 μm, and so it was assumed that the majority of the GO nanoparticles were filtered from the solution. Additionally, the 0.2 μm stainless steel frit column guard was unaffected by injections after filtering out the GO, indicating that the polymer solutions being measured on the SEC-MALLS are free of GO contamination.

Differential scanning calorimetry (DSC) was used to measure the heat of fusion and re-crystallization in PA11. The DSC was a TA Instruments Q20 and was calibrated using indium. A ramp rate of 3 $^{\circ}C/min$ was used to heat, cool, and re-heat the samples under nitrogen from 40 to 220 $^{\circ}C$. The integration limits were 140 $^{\circ}C$ to 200 $^{\circ}C$ for the heating ramps and 130 $^{\circ}C$ to 190 $^{\circ}C$ for the cooling ramp. The root of the peak onset maximum slope with the peak baseline set to zero is the fusion or crystallization onset temperature.

Optical microscopy images were taken with an IX71 Olympus Inverted microscope and a LUCPLFLN, 40x (0.6 NA) objective. Transmission bright field and cross polarized light images were taken. In transmission mode the light passes through the sample. With cross polarizers, the birefringent and therefore visible crystalline regions of PA11 and 1-GO-PA11 were imaged. For PA11 and 1-GO-PA11, optical glass microscope slides were prepared by melt pressing the PA11 or 1-GO-PA11 for 30 seconds at 250 ˚C under argon flow, then ambient cooling to room temperature. The 5-GO-PA11 was microtomed to obtain a sample thin enough for optical transmission, less than 150 nm.

Attenuated total reflectance fourier transform infrared spectroscopy (ATR-FTIR) was used to probe the chemical functional groups and intermolecular interactions. Spectra were taken using an IR Tracer-100 Shimadzu FTIR with a MIRacle 10 Single Reflectance ATR accessory at a resolution of 2 cm^{-1} and averaged from 32 scans from 600 to 4000 cm^{-1}. After adjusting to a common baseline and normalizing to peak 2851 cm^{-1}, the work of Skrovanek, Painter[47] was followed to de-convolute the 1635 cm^{-1} carbonyl oxygen peak using MagicPlot software to measure the relative concentration of free and hydrogen bonded amide oxygen groups characterized at 1684, 1654, and 1635 cm^{-1}. The heights of the de-convoluted peaks were used to compare the relative concentration of hydrogen bound carbonyl oxygen groups. The half height peak width of the 3304 cm^{-1} N-H was also used to probe the hydrogen bonding behavior of the amide hydrogen.

The M_{me}, hydrolysis rate constant (k_H), and solid state polymerization (k_p) rate

constant were determined during accelerated molecular weight degradation by fitting the literature mathematical model of amide hydrolysis to the measured M_m per aging time using nonlinear least squares [48-50]. The values k_H and k_P, which were used to fit the changing values of molecular weight with time, reflect the composition of the aqueous aging environment and its effect on the hydrolysis process. The previously published model was derived from the condensation-hydrolysis kinetics described by the kinetic Equation 2-1 on page 15.

5.3 Results and Discussion

The M_{me} of 1-GO-PA11 was 10 kDa larger than that obtained for PA11 at both 100 ˚C and 120 ˚C, Figure 5-2. This is an impressive increase of 50 % at both temperatures. Using Equation 2-12 and a least squares fit, the hydrolysis (k_H) and solid state re-polymerization (k_P) rate constants were determined and listed in Table 5-1. At 120 ˚C, both k_H and k_P were reduced for 1-GO-PA11 compared with PA11. The higher loading, 5-GO-PA11 showed no change in the rate of hydrolytic degradation compared with PA11. The absence of this effect at the higher concentration was attributed to a poor nano-particle dispersion as shown in Figure 5-3. In summary, Figure 5-2 and Table 5-1 show that the 1-GO-PA11 k_H was reduced by a factor of 2 and the M_{me} was increased by 50 % at both temperatures.

In the 1-GO-PA11, there are three species involved in the amide hydrolysis reaction: polyamide chains, GO, and water. Within Figure 5-4 - Figure 5-7 are the elementary amide hydrolysis reaction mechanisms by which the amide bond in the polymer chain is weakened resulting in chain scission and a reduction in molecular weight. Figure 5-4 shows the initial resonance stabilization of the amide bond. Three elementary chemical mechanisms for chain scission have been identified: base catalyzed[51-55], acid catalyzed[56-59], and water assisted[60, 61]. The activation energies have been determined to be 21, 31, and 99 $^{kJ}/_{mol}$ for the base catalyzed, acid catalyzed, and water assisted mechanisms of amide hydrolysis respectively[62]. Computationally, Zahn [60] found the activation energies to be 66, 78, and 147 $^{kJ}/_{mol}$. Thus, given equivalent concentrations of OH^- and H^+, the base catalyzed pathway is favored; the water assisted hydrolysis of an amide bond is the least favored pathway.

The base catalyzed hydrolysis mechanisms are shown in Figure 5-5. Zahn [51] computationally studied the mechanism of base catalyzed hydrolysis of the amide bond, and found that the base catalyzed Pathway II is favored. Zahn [51] also found that no proton transfer reaction led to the simultaneous protonation of the amide nitrogen and deprotonation of the hydroxyl group. As well, the amide anion is a poorer leaving group than an alkoxide ion, and in the base catalyzed hydrolysis, the proton transfer to the amide anion is considered the rate limiting step[63, 64].

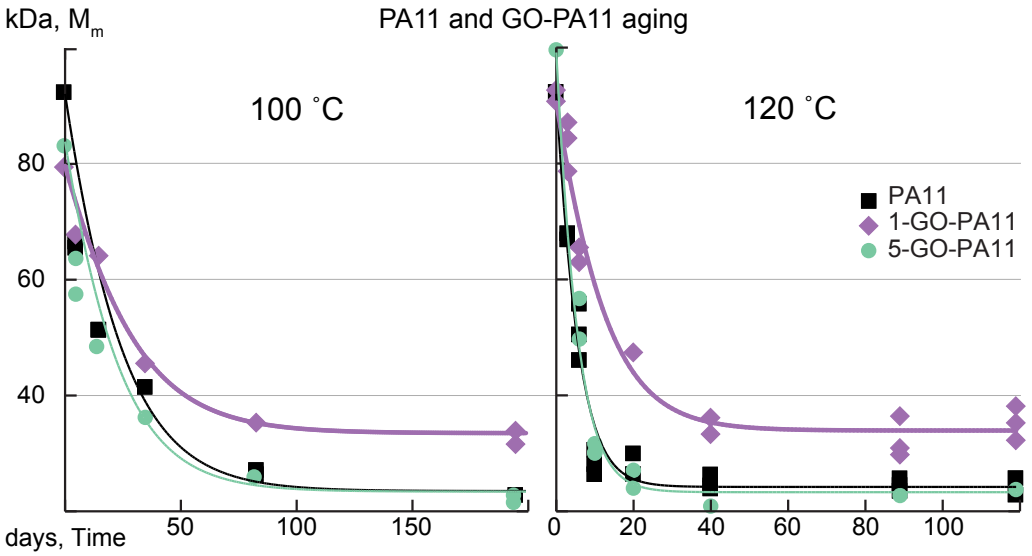

Figure 5-2: M_m of PA11 aging in water over time at 100 ˚C and 120 ˚C. M_{me} of 1-GO-PA11 was approximately 10 kDa higher than PA11 and 5-GO-PA11 at 100 ˚C and 120 ˚C aging temperatures, respectively.

Table 5-1: Rate constants and M_{me} for GO-PA11 aged in water; determined using Equation 2-12 and a non-linear least squares fit.

°C **Aging Temperature**	mg/g **GO Loading**	$K_H \times 10^{-2}$	$K_p \times 10^{-5}$	kDa M_{me}
100	0	2.8 ±0.5	5.0 ±1.5	24 ±3
	1	1.8 ±0.5	10.0 ±4.0	34 ±3
	5	2.9 ±0.6	6.8 ±2.4	24 ±3
120	0	12 ±2	23 ±7	24 ±3
	1	4.5 ±1.1	17 ±5	34 ±3
	5	13 ±2	19 ±5	23 ±3

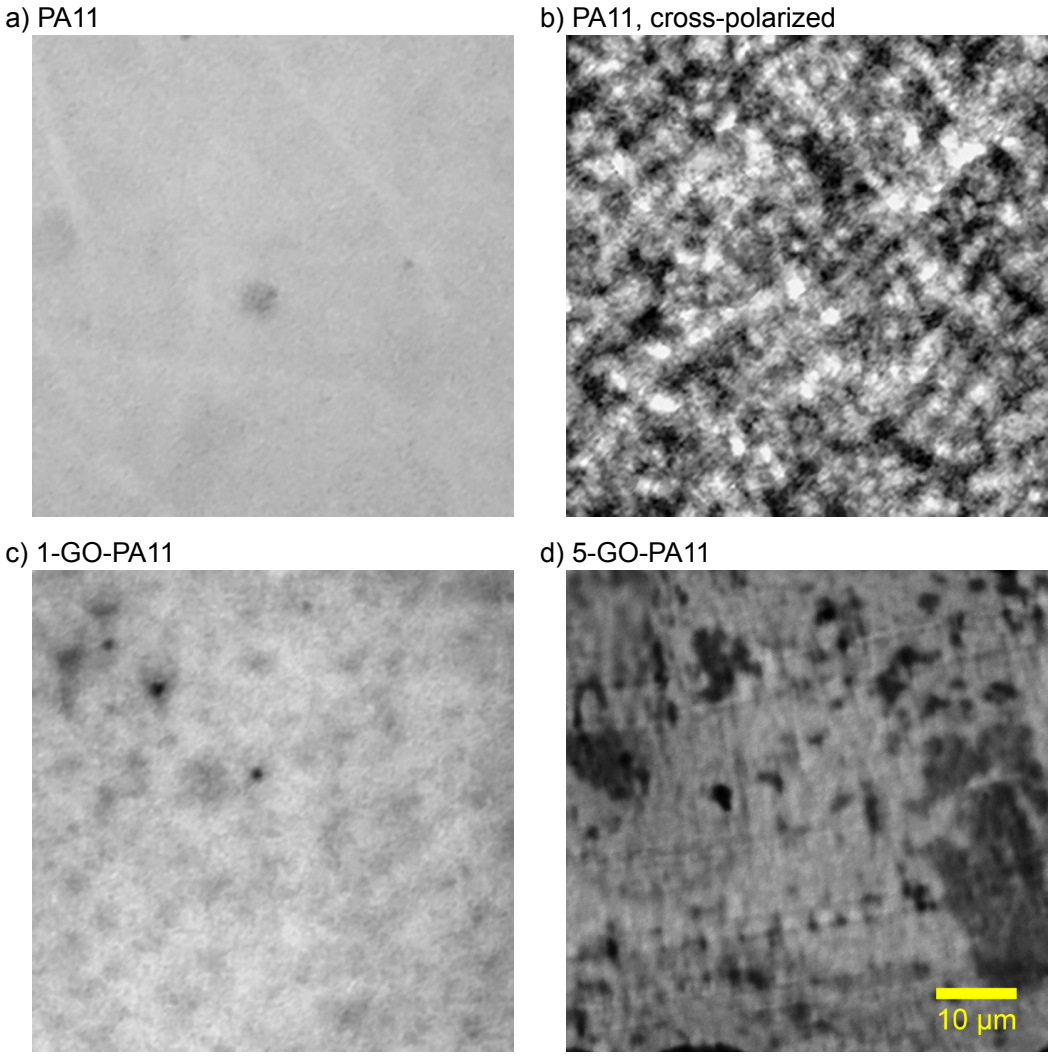

Figure 5-3: 60 x 60 µm transmission optical microscopy images of PA11 bright field (6a), cross-polarized (6b), 1-GO-PA11 bright field (6c), and 5-GO-PA11 bright field (6d).

The four step acid catalyzed hydrolysis mechanism is shown in Figure 5-6. The first step is the protonation of the carbonyl oxygen of the amide bond. Zahn [65] found in a computational study that the second step, nucleophilic attack of a water molecule to the carbon atom of the amide group, is the rate determining step. The third step is the intermediate de-protonation of the carbonyl oxygen and protonation of the amide nitrogen, quickly followed by the dissociation of the protonated amine and the carbonyl acid.

The water assisted hydrolysis mechanism is shown in Figure 5-7. The water assisted mechanism involves two water molecules that act in a concerted process and utilize a Grotthuss mechanism of proton hopping through hydrogen bonding. The first step and rate determining step are the nucleophilic attack of the amide carbon and simultaneous protonation of the amide nitrogen[60].

PA11 is a semicrystalline polymer. Amide hydrolysis in PA11 is understood to occur in the amorphous region rather than the impermeable crystalline domain. An important component of the crystalline formation is hydrogen bonding. The hydrogen bonding between adjacent amide groups is responsible for the higher melting temperatures of polyamide crystalline structures when compared with a non-polar semicrystalline polymer such as polyethylene. Additionally, hydrogen bonding between nearby amide bonds also occurs in the amorphous regions.

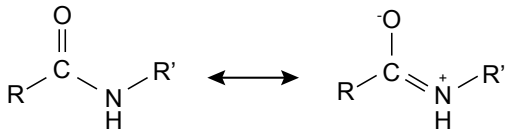

Figure 5-4: Elementary chemical mechanism of resonance stabilization of the amide bond.

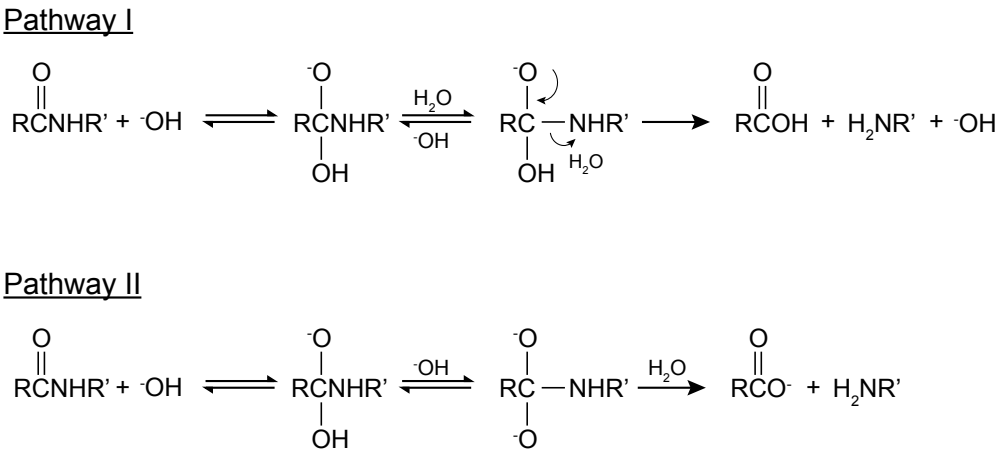

Figure 5-5: Base catalyzed elementary chemical mechanism of amide hydrolysis.

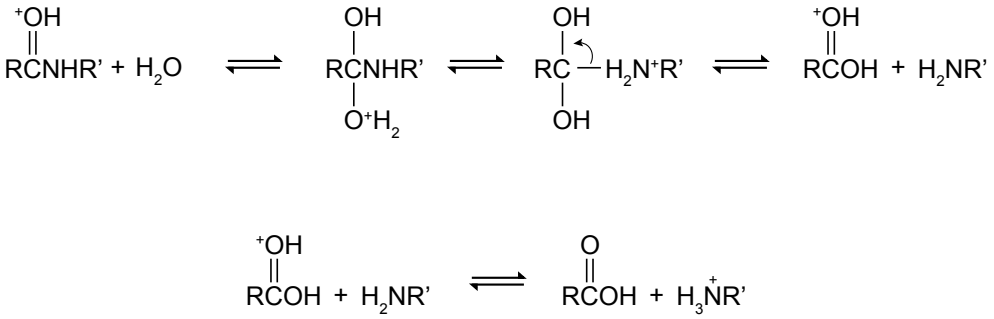

Figure 5-6: Acid Catalyzed elementary chemical mechanism of amide hydrolysis.

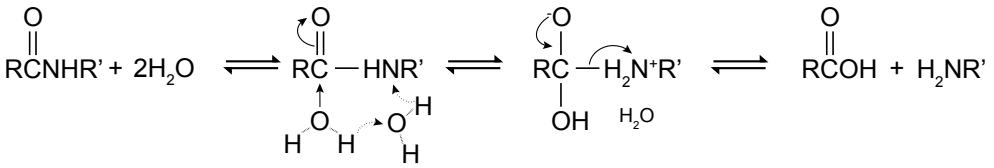

Figure 5-7: Elementary chemical mechanism for water assisted hydrolysis of the amide bond.

The GO nanoparticles are large immobile 2-D nano-thin barriers within the PA11 matrix. Consequently, they will reduce molecular mobility within the polymer. As such, we suggest that the GO nano-sheets reduce molecular mobility for both PA11 chains and water thus resulting in fewer accessible hydrolysis sites. To provide evidence for GO's reducing chain mobility, we characterized GO's effect on the rate of crystallization in PA11 and GO-PA11 - unaged and aged using DSC. Nanoparticles are known to affect the crystalline morphology of PA11[44, 66-75]. The DSC test was a standard heat, cool, heat sequence at 3 $^{\circ}C/_{min}$ between 40 and 220 $^{\circ}C$. Figure 5-8 shows the DSC curves of the unaged and 80-90 days aged samples in three columns from left to right to indicate the heat (fusion), cool (crystallization), and heat (fusion) curves. The peak integration values of specific heat of fusion (ΔH_{fus}) and crystallization (ΔH_c) are listed in Table 5-2.

Peak and onset temperatures are respectively tabulated in Table 5-3 and Table 5-4 for the fusion and crystallization of PA11 and GO-PA11. The effect of the previous thermal history on the semi-crystalline behavior of PA11 is revealed in the first heat ramp. The first heat ramp both reveals the previous thermal history on the semi-crystalline behavior of PA11 and melts the PA11 to erase that previous thermal history. The 3 $^{\circ}C/_{min}$ controlled cooling ramp measures the affect that GO has upon the crystallization behavior of PA11, both nucleation and growth. The second heating ramp compares how the total crystallization growth is affected by the GO loading.

The enthalpy of fusion, ΔH_{fus}, is the heat require to melt the crystalline regions

of PA11. In Table 5-2, a lower total ΔH_{fus} indicates a decrease in the crystallinity of the GO-PA11 after heat, cool, and re-heat ramps.

During aging at 100 and 120 ˚C, the PA11 matrix was annealed, resulting in increased crystallinity. Quantified by the peak total area, the first heating ramp reveals the extent of annealing for the PA11 and GO-PA11 samples via their ΔH_{fus}. Before aging, PA11 had 25% crystallinity, using 189 $^{J}/_{g}$ as 100% crystalline PA11[76]. Upon aging and annealing PA11, the crystallinity increased to 34% and 48% at 100 and 120 ˚C; a relative increase of 36% and 92%, respectively. The 1-GO-PA11 starts with a crystallinity of 25% and has lower relative increases of 12% and 76% at the same annealing conditions.

These results show the GO nano-sheets hindered crystallization annealing in PA11 during aging at these temperatures. The 1-GO-PA11 samples have the lowest ΔH_{fus} in both 100 and 120 ˚C conditions indicating a large immobilizing effect on the polymer chains. Again, the decreased effect of the 5-GO-PA11 as previously described is attributed to agglomeration and poor dispersion of 2-D nano-particles.

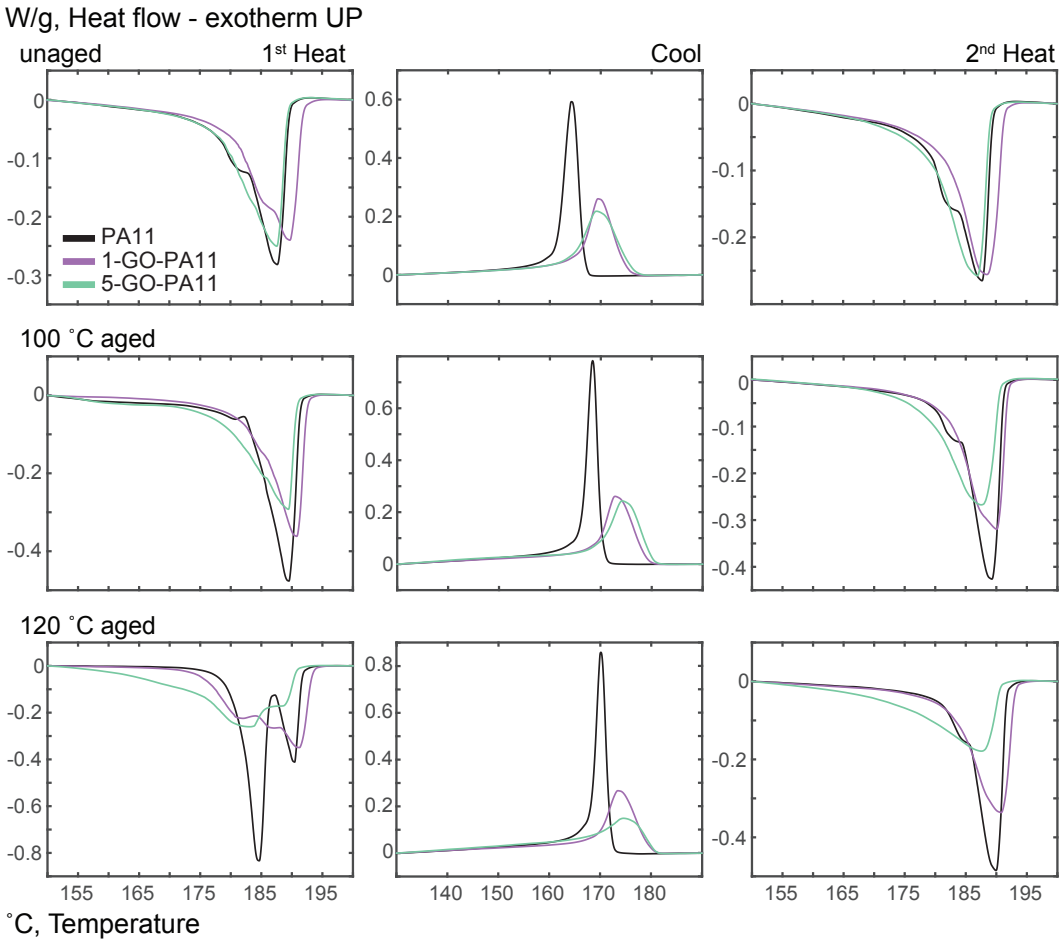

Figure 5-8: DSC scans for unaged, 100 ˚C, and 120 ˚C 80-90 days aged PA11 unloaded, 1-GO-PA11, and 5-GO-PA11. The DSC test was a standard heat, cool, heat sequence at 3 ˚C/min between 40 and 220 ˚C. The 3 columns from left to right are 1st heat ramp from 40 ˚C to 220 ˚C, followed by a cool ramp to 40 ˚C, and a 2nd heat ramp to 220 ˚C. The rows top to bottom are unaged, 100 ˚C, and 120 ˚C aged samples.

Table 5-2: Integration values of differential scanning calorimetry heat flow peaks from 140 ˚C to 200 ˚C for GO-PA11 and PA11, aged and unaged samples. The error margin is 2.5 J/g per measurement and peak integration.

Sample	GO Loading mg/g	1st Heat Ramp ΔH_{fus} J/g	Cooling Ramp ΔH_c J/g	2nd Heat Ramp ΔH_{fus} J/g
Unaged	0	47.5	50.0	48.0
	1	46.5	42.5	49.0
	5	46.0	44.0	49.0
100 ˚C aged	0	63.0	60.0	60.0
	1	53.0	50.0	55.0
	5	57.5	53.5	56.0
120 ˚C aged	0	91.0	65.5	61.0
	1	82.0	53.5	59.0

Table 5-3: DSC peak temperatures for GO-PA11 and PA11, aged and unaged samples. The peak temperatures are accurate within 0.5 ˚C.

Sample	GO Loading mg/g	˚C 1st Heat Ramp $T_{fus,m}$	˚C Cooling Ramp $T_{c,m}$	˚C 2nd Heat Ramp $T_{fus,m}$
Unaged	0	187.5	166.5	187.5
	1	190.0	169.5	188.5
	5	187.5	169.0	187.0
100 ˚C aged	0	189.5	168.5	189.5
	1	191.0	173.0	190.0
	5	189.5	174.0	187.5
120 ˚C aged	0	184.5, 190.5	170.0	190.0
	1	182.0, 187.0, 191.0	173.5	191.0

Table 5-4: DSC onset melting and formation temperatures for GO-PA11 and PA11, aged and unaged samples. The onset melting and formation temperatures are accurate within 0.5 ˚C.

Sample	GO Loading mg/g	˚C 1st Heat Ramp $T_{fus,o}$	˚C Cooling Ramp $T_{c,o}$	˚C 2nd Heat Ramp $T_{fus,o}$
Unaged	0	175.5, 180.5	167.0	177.5, 178.5
	1	178.5, 180.0	175.0	181.0
	5	175.0, 176.5	176.0	178.0
100 ˚C aged	0	182.5, 183.5	170.5	178.0, 183.0
	1	179.5, 183.5	179.0	181.5
	5	177.5, 179.5	180.0	177.5
120 ˚C aged	0	181.0, 186.5	172.0	180.0, 184.5
	1	174.0, 177.5, 181.5	179.5	182.5

The melting temperatures ($T_{fus,m}$) in Table 5-3 for PA11 and GO-PA11 are indicative of the thermal stability of the polymer crystalline regions. A lower pre-peak $T_{fus,m}$, 184.5 ˚C, becomes increasingly prominent for the PA11 when aged at 120 ˚C. The 184.5 ˚C pre-peak is attributed to poorly formed crystalline structures[71, 76-79]. As seen in Figure 5-8, the PA11 has the largest pre-peak at 184.5 in the first heating ramp after aging at 120 ˚C. Conversely, the poorly formed crystals are not favored in the 1-GO-PA11 and there is an additional intermediate melting peak at $T_{fus,m}$ 187.0 ˚C. The highest $T_{fus,m}$ of 191.5 ˚C indicates that the annealed GO-PA11 has the most stable crystalline structure. We attribute this increase in the annealed crystalline melt temperature after aging to intermolecular attractive interactions between the GO sheets and the polyamide matrix as will be shown from the ATR-IR spectra.

After the first heating ramp on the DSC, the polymer sample melts and its thermal history erased. With controlled cooling, the heat of re-crystallization (ΔH_c) can be characterized. The ΔH_c values compare the integrated crystalline region formation in PA11 and GO-PA11. The decrease in the ΔH_c for GO-PA11 compared to PA11 indicates that the chain mobility during cooling is inhibited by the inclusion of GO nanoparticles.

The GO-PA11 has a higher ΔH_c onset temperature ($T_{c,o}$) and lower ΔH_c value than PA11, Table 5-4. The unaged PA11 has a $T_{c,o}$ of 167 ˚C that increases to 170 (+2%) and 172 (+3%) ˚C after aging at 100 and 120 ˚C. The increase in $T_{c,o}$ after aging correlates to lower molecular weights. For a polyamide, crystalline regions

form more quickly at lower molecular weights due to increased mobility and ease of alignment of the shorter polymer chains[80]. Both GO-PA11 show a 9 ˚C higher $T_{c,o}$ with a broader reaction peak than unloaded PA11. The 1-GO-PA11 samples initially have a 175 ˚C $T_{c,o}$. After aging at 100 ˚C, the $T_{c,o}$ increases to 179 (+2%) ˚C; aging at 120 ˚C increases the $T_{c,o}$ to 180 (+3%) ˚C. The increased $T_{c,o}$ of the GO-PA11 samples is evidence that the GO nano-particles are nucleating sites resulting in higher crystallization onset temperatures.

The crystalline regions in PA11 are expected to be impermeable to water molecules and therefore hydrolysis would take place solely in the molecularly mobile amorphous regions. Since GO-PA11 has a lower crystalline content, it might be expected that an increased percentage of amide bonds in the amorphous regions would result in an increase in hydrolysis. However, the well dispersed 1-GO-PA11 shows a 50% higher M_{me} than the PA11, Figure 5-2.

Similarly, when PA11 is plasticized with N-n-butylbenzenesulfonamide (BBSA), the BBSA increases the amorphous content in PA11 and the plasticized PA11 exhibits a higher equilibrium molecular weight than neat PA11[48, 81]. The function of BBSA is to hydrogen bond with amide bonds and prevent intermolecular hydrogen bonding between amide bonds resulting in lower crystallinity.

From the amide bond hydrolysis elementary mechanisms for base hydrolysis Figure 5-5, acid hydrolysis Figure 5-6, and water assisted hydrolysis Figure 5-7,

it is clear that both the availability of water molecules and hydrogen bonding are required for amide hydrolysis. Thus the BBSA's disruption of inter-chain hydrogen bonding also inhibits hydrolysis. Changes in the hydrogen bonding behavior in 1-GO-PA11 is another proposed possible explanation for GO inhibiting the hydrolysis process, in addition to its large immobile nano-sheet structure that inhibits polymer chain and water mobility.

Infrared spectroscopy probes the PA-11 inter-molecular interactions, and hydrogen bonding behavior at the amide bonds. Figure 5-9 shows the FTIR spectra for PA11 and 1-GO-PA11, unaged and aged. The characteristic peaks are: 1158 cm^{-1}, an interaction of the N-H stretch and O=C-N deformation; 1539 cm^{-1}, the amide II characteristic peak a C-N stretch; 1635 cm^{-1}, the amide I characteristic peak a carbonyl oxygen stretch; 2851 cm^{-1}, symmetric C-H aliphatic vibration; 2919 cm^{-1}, asymmetric C-H aliphatic vibration; and 3304 cm^{-1}, the stretching of the amide N-H bond.

Hydrogen bonding in the PA11 matrix is an intermolecular interaction between the amide hydrogen and the carbonyl oxygen of a neighboring amide bond. Skrovanek, Painter [47] first studied the use of FTIR to detect hydrogen bonding interactions within a PA11 polymer. Skrovanek, Painter [47] found de-convoluting the 1635 cm^{-1} peak of the carbonyl oxygen revealed three peaks that could be characterized at 1635, 1654, and 1684 cm^{-1}. The 1635 cm^{-1} sub-peak is a lower energy carbonyl vibration correlated to aligned hydrogen bonding. The 1654 cm^{-1} peak is un-aligned amorphous hydrogen bound carbonyl oxygens. And, the 1684

cm^{-1} peak is correlated with carbonyl oxygen groups that are free of hydrogen bonding. Following the work of Skrovanek, Painter [47], the amide bond 1635 cm^{-1} peak of the carbonyl oxygen was de-convoluted to probe the hydrogen bonding interactions at the amide bond. Through deconvolution of the 1635 cm^{-1} amide C=O, no difference was observed at the carbonyl oxygen peaks for PA11 and GO-PA11: further details can be found in the supplementary material.

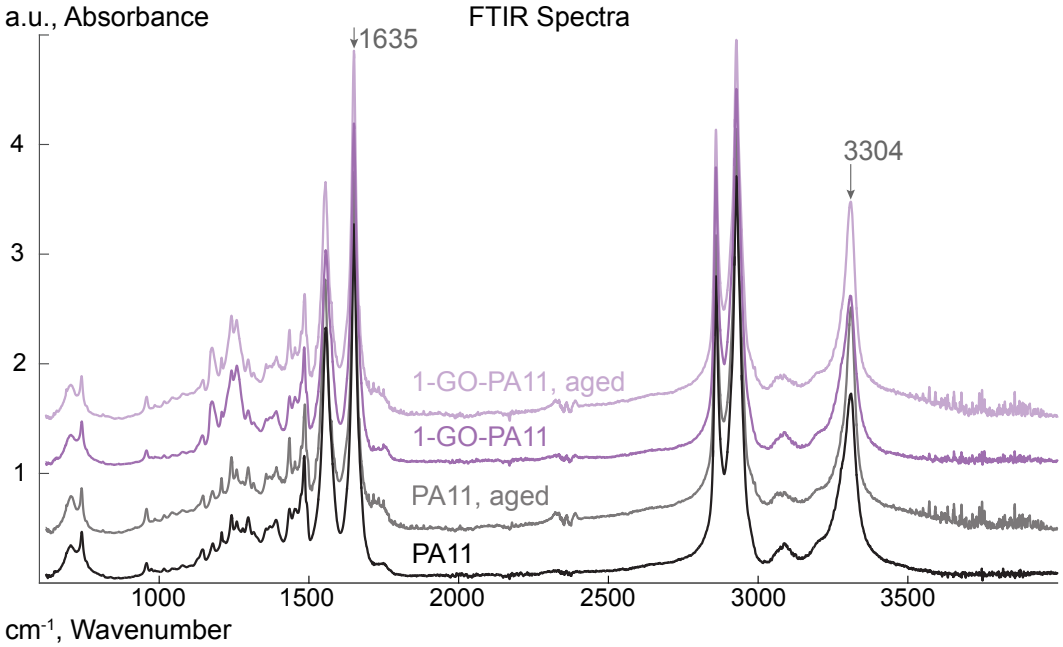

Figure 5-9: Attenuated total reflectance fourier tranform infrared spectra of PA11 & 1-GO-PA11, and aged PA11 & aged 1-GO-PA11.

Figure 5-10 plots the half height peak widths of the 3305 cm^{-1} N-H stretching peak for the PA11 and 1-GO-PA11, unaged and aged. The peak widths are associated with the distribution of hydrogen bonding orientations of the amide bond hydrogen. With aging, the PA11 shows a decline in the distribution of hydrogen bonding orientations; from 54 to 34 ±2 cm^{-1}. The 1-GO-PA11 shows less decline in the 3304 cm^{-1} peak widths; from 54 to 39 ±2 cm^{-1}. The broader distribution of hydrogen bonding orientations in the GO-PA11 has also been correlated previously to the lower overall crystallinity content[47].

In aged 1-GO-PA11, the N-H stretch has a broader distribution than aged PA11, Figure 5-10. Further 1-GO-PA11 has an increased intensity at the 1158 cm^{-1} peak - an interaction of the N-H stretch and O=C-N deformation. These results show that the GO with C=O groups present on the surface[82] are interacting with the N-H amide hydrogen of polyamide. This interaction reduces the molecular mobility of the PA11 chain and thereby reducing the rate of hydrolysis and rate of the crystallization.

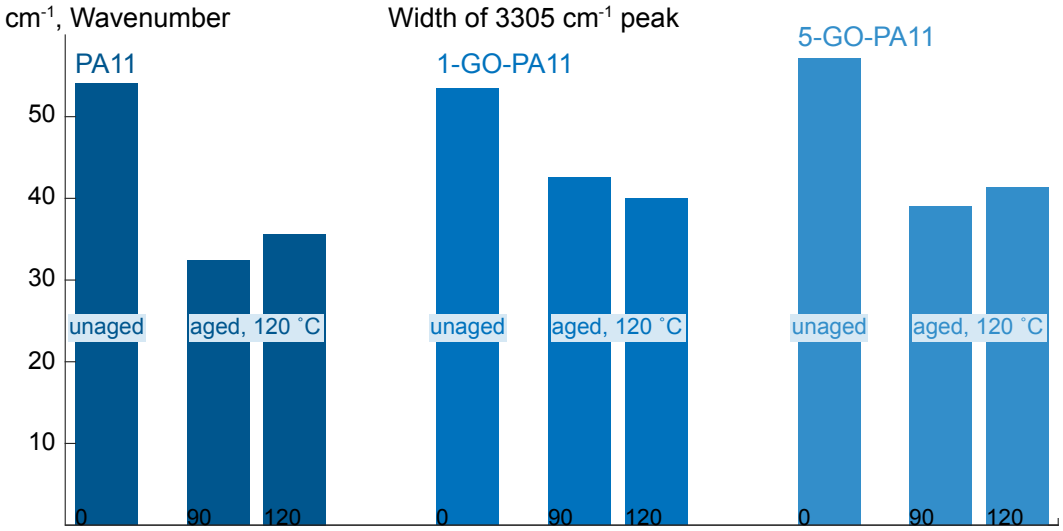

Figure 5-10: The peak widths centered at 3305 cm^{-1} for PA11, 1-GO-PA11, and 5-GO-PA11 and grouped by unaged and aged at 120 ˚C for 90 days.

In summary, the large immobile GO, a 2-dimensional sheet in the amorphous phase, inhibits molecular mobility and competes for hydrogen bonding with polyamide's amide hydrogens. Both of these effects inhibit amide hydrolysis of the amide bond. It is the decrease in chain mobility and water molecules, and hydrogen bonding interactions between GO and the N-H bonds of the polymer chains, that leads to a lower hydrolysis rate for the well dispersed 1-GO-PA11, Table 5-1. These two effects of GO's large sheet shape and its surface functional groups interacting with the polymer chain, were also shown to similarly reduce polymer chain mobility in polyimide[83].

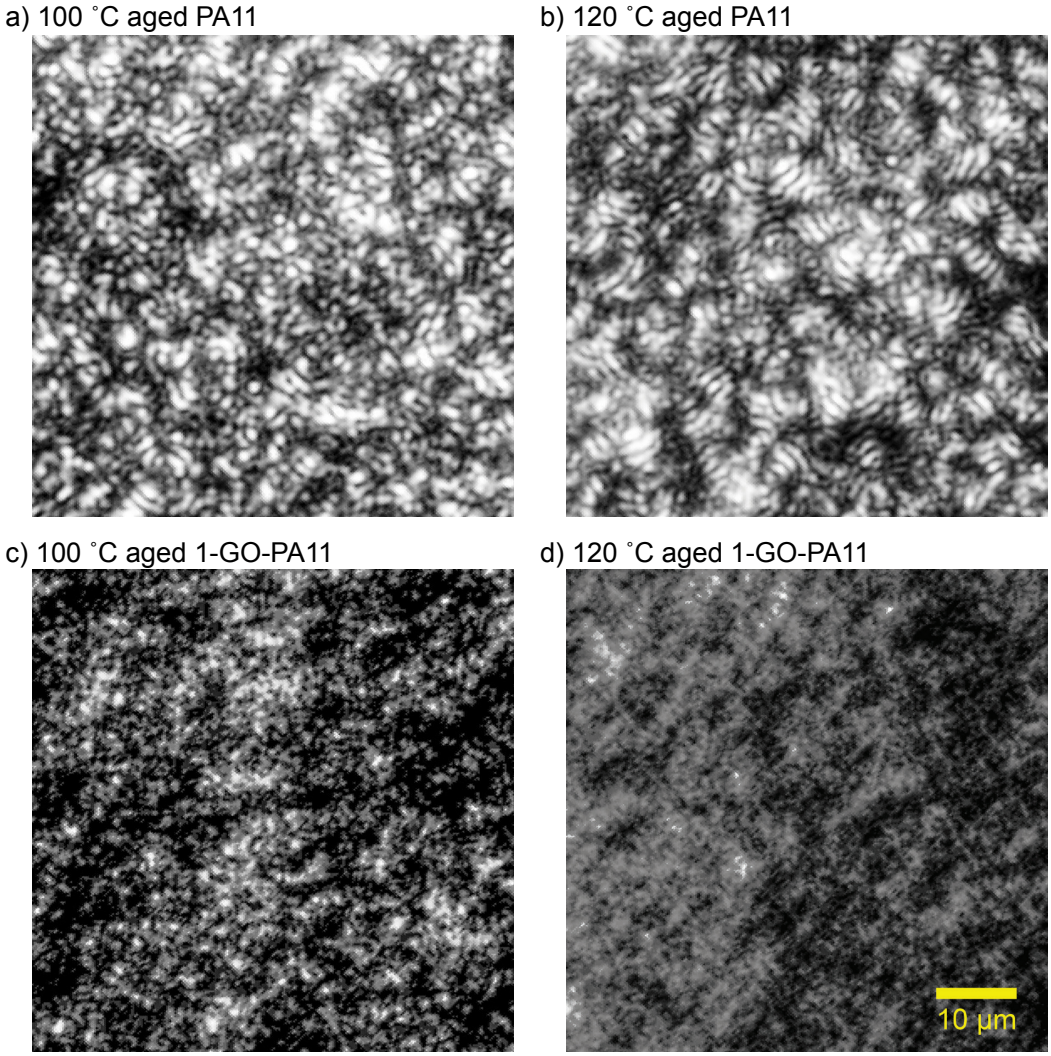

Figure 5-11: 60 x 60 µm cross polarized transmission optical microscopy images of 100 ˚C and 120 ˚C aged PA11 and 1-GO-PA11.

A transmission optical microscope was used in cross-polarization mode to observe the birefringence of the crystalline regions within PA11 and 1-GO-PA11. Figure 5-11 showed that well dispersed GO within the polymer matrix alters the micro-crystalline morphology of PA11. The 1-GO-PA11 showed less birefringence than PA11. The aged PA11 showed the most birefringence, and broader bands of birefringence, banded spherulites, for both the 100 and 120 ˚C, with widths of 0.94 ±0.27 and 1.03 ±0.15 μm respectively. This is associated with bundling of laminar stacks and higher crystallinity[70, 76]. The larger bundled laminar stacks in aged PA11 are absent in the aged 1-GO-PA11 optical images. The bundles of laminar stacks in 100 and 120 ˚C aged 1-GO-PA11 appear much thinner with widths of 0.71 ±0.18 and 0.67 ±0.07 μm respectively. Zhang, Yu [77] reported a similar crystalline behavior in montmorillonite-PA11 nanocomposites. These smaller crystalline domains agree with the lower crystallinity DSC results for 1-GO-PA11 in Table 5-2.

The optical images of 5-GO-PA11 show that GO was highly agglomerated, Figure 5-3. In 5-GO-PA11, the GO sheets are in contact with each other. This aggregation resulted in no effect on the M_{me} compared with the finely dispersed GO in the 1-GO-PA11 nanocomposite.

5.4 Summary and Conclusion

A concentration of 0.1 wt% GO in PA11 produced a 50 % increase over PA11's equilibrium molecular weight when aged in water at 100 and 120 ˚C, respectively. No improvement was observed in the 0.5 wt% GO-PA11 due to GO agglomeration. Fitting the previously reported kinetic model to aging results showed an increase in equilibrium molecular weight, when the GO particles were well dispersed. This was due to a reduction in the model's hydrolytic rate constant relative to that of re-polymerization.

GO-PA11's decreased ability to crystallize showed that the presence of GO decreased molecular mobility within the nano-particle polymer system. Based on the heat of fusion, both as prepared nanocomposites decreased the amount of PA11 crystallinity slightly. Additionally, the heat of fusion for all three aged materials were nearly comparable after the second heat suggesting that there was no affect upon crystallinity. There was a big effect for the aged samples. On aging at both 100 ˚C and 120 ˚C, the GO-PA11 had significantly less crystallinity demonstrating a reduction in the rate of annealing. After heating above the melting temperature and cooling, the GO again inhibited the rate of crystallization, but the materials were nearly comparable suggesting no effect on the crystallinity. The decrease in the annealing rate of crystallization in the aged samples is attributed to GO's large immobile nano thickness sheet structure, which inhibited chain mobility within the polymer nanocomposite.

ATR-FTIR spectra showed that the graphene oxide's surface C=O groups hydrogen bond with the polyamide's N-H groups. This interaction further inhibits polymer mobility.

In summary these two factors, the large immobile nano thin GO sheets and the intermolecular interaction between the GO's surface C=O groups with the polyamide's N-H groups, significantly reduced the mobility in the GO-polymer resulting in a reduction in the rate of crystallization and most importantly the rate of degradation by hydrolysis.

5.5 References

[5_1] MEYER, A., JONES, N., LIN, Y. & KRANBUEHL, D. 2002. Characterizing and Modeling the Hydrolysis of Polyamide-11 in a pH 7 Water Environment. Macromolecules, 35, 2784-2798.

[5_2] API 2003. Technical Report 17TR2, The Ageing of PA-11 in Flexible Pipes. Washington, DC: American Petroleum Institute.

[5_3] POTTS, J. R., DREYER, D. R., BIELAWSKI, C. W. & RUOFF, R. S. 2011. Graphene-based polymer nanocomposites. Polymer, 52, 5-25.

[5_4] USUKI, A., KOJIMA, Y., KAWASUMI, M., OKADA, A., FUKUSHIMA, Y., KURAUCHI, T. & KAMIGAITO, O. 1993. SYNTHESIS OF NYLON 6-CLAY HYBRID. Journal of Materials Research, 8, 1179-1184.

[5_5] BUNCH, J. S., VERBRIDGE, S. S., ALDEN, J. S., VAN DER ZANDE, A. M., PARPIA, J. M., CRAIGHEAD, H. G. & MCEUEN, P. L. 2008. Impermeable Atomic Membranes from Graphene Sheets. Nano Letters, 8, 2458-2462.

[5_6] LEENAERTS, O., PARTOENS, B. & PEETERS, F. M. 2008. Graphene: A perfect nanoballoon. Applied Physics Letters, 93, 193107-4.

[5_7] DHAND, V., RHEE, K. Y., JU KIM, H. & HO JUNG, D. 2013. A Comprehensive Review of Graphene Nanocomposites: Research Status and Trends. Journal of Nanomaterials, 2013, 1-14.

[5_8] KIM, H., ABDALA, A. A. & MACOSKO, C. W. 2010a. Graphene/Polymer Nanocomposites. Macromolecules, 43, 6515-6530.

[5_9] MITTAL, V. 2014. Functional Polymer Nanocomposites with Graphene: A Review. Macromolecular Materials and Engineering, 299, 906-931.

[5_10] YOO, B. M., SHIN, H. J., YOON, H. W. & PARK, H. B. 2014. Graphene and Graphene Oxide and Their Uses in Barrier Polymers. Journal of Applied Polymer Science, 131, 39628-39651.

[5_11] DREYER, D. R., PARK, S., BIELAWSKI, C. W. & RUOFF, R. S. 2010. The chemistry of graphene oxide. Chemical Society Reviews, 39, 228-240.

[5_12] BRODIE, B. C. 1859. On the Atomic Weight of Graphite. Philosophical Transactions of the Royal Society of London, 149, 249-259.

[5_13] KUILA, T., KHANRA, P., MISHRA, A. K., KIM, N. H. & LEE, J. H. 2012. Functionalized-graphene/ethylene vinyl acetate co-polymer composites for improved mechanical and thermal properties. Polymer Testing, 31, 282-289.

[5_14] TERRONES, M., MARTÍN, O., GONZÁLEZ, M., POZUELO, J., SERRANO, B., CABANELAS, J. C., VEGA-DÍAZ, S. M. & BASELGA, J. 2011. Interphases in Graphene Polymer-based Nanocomposites: Achievements and Challenges. Advanced Materials, 23, 5302-5310.

[5_15] STAUDENMAIER, L. 1898. Verfahren zur Darstellung der Graphitsäure. Berichte der deutschen chemischen Gesellschaft, 31, 1481-1487.

[5_16] HOFMANN, U. & KÖNIG, E. 1937. Untersuchungen über Graphitoxyd. Zeitschrift für anorganische und allgemeine Chemie, 234, 311-336.

[5_17] HUMMERS JR, W. S. & OFFEMAN, R. E. 1958. Preparation of Graphitic Oxide. Journal of the American Chemical Society, 80, 1339.

[5_18] KOVTYUKHOVA, N. I., OLLIVIER, P. J., MARTIN, B. R., MALLOUK, T. E., CHIZHIK, S. A., BUZANEVA, E. V. & GORCHINSKIY, A. D. 1999. Layer-by-Layer Assembly of Ultrathin Composite Films from Micron-Sized Graphite Oxide Sheets and Polycations. Chemistry of Materials, 11, 771-778.

[5_19] MARCANO, D. C., KOSYNKIN, D. V., BERLIN, J. M., SINITSKII, A., SUN, Z., SLESAREV, A., ALEMANY, L. B., LU, W. & TOUR, J. M. 2010. Improved Synthesis of Graphene Oxide. ACS Nano, 4, 4806-4814.

[5_20] ZHAO, J., PEI, S., REN, W., GAO, L. & CHENG, H.-M. 2010. Efficient Preparation of Large-Area Graphene Oxide Sheets for Transparent Conductive Films. ACS Nano, 4, 5245-5252.

[5_21] ROBINSON, J. T., ZALALUTDINOV, M., BALDWIN, J. W., SNOW, E. S., WEI, Z., SHEEHAN, P. & HOUSTON, B. H. 2008. Wafer-scale Reduced Graphene Oxide Films for Nanomechanical Devices. Nano Letters, 8, 3441-3445.

[5_22] ADELNIA, H., GUDARZI, M. M. & GAVGANI, J. N. 2013. Intumescent flame retardant polyurethane/reduced graphene oxide composites with improved mechanical, thermal, and barrier properties. Journal of Materials Science, 49,

243-254.

[5_23] KIM, H., MIURA, Y. & MACOSKO, C. W. 2010b. Graphene/Polyurethane Nanocomposites for Improved Gas Barrier and Electrical Conductivity. Chemistry of Materials, 22, 3441-3450.

[5_24] KIM, H. & MACOSKO, C. W. 2009. Processing-property relationships of polycarbonate/graphene composites. Polymer, 50, 3797-3809.

[5_25] LIU, H., KUILA, T., KIM, N. H., KU, B.-C. & LEE, J. H. 2013a. In situ synthesis of the reduced graphene oxide–polyethyleneimine composite and its gas barrier properties. Journal of Materials Chemistry A, 1, 3739-3746.

[5_26] PARK, O.-K., KIM, S.-G., YOU, N.-H., KU, B.-C., HUI, D. & LEE, J. H. 2014. Synthesis and properties of iodo functionalized graphene oxide/polyimide nanocomposites. Composites Part B, 56, 365-371.

[5_27] STANKOVICH, S., DIKIN, D. A., DOMMETT, G. H. B., KOHLHAAS, K. M., ZIMNEY, E. J., STACH, E. A., PINER, R. D., NGUYEN, S. T. & RUOFF, R. S. 2006. Graphene-based composite materials. Nature, 442, 282-286.

[5_28] ZHENG, D., TANG, G., ZHANG, H.-B., YU, Z.-Z., YAVARI, F., KORATKAR, N., LIM, S.-H. & LEE, M.-W. 2012. In situ thermal reduction of graphene oxide for high electrical conductivity and low percolation threshold in polyamide 6 nanocomposites. Composites Science and Technology, 72, 284-289.

[5_29] ZHU, J., LIM, J., LEE, C.-H., JOH, H.-I., KIM, H. C., PARK, B., YOU, N.-H. &

LEE, S. 2014. Multifunctional polyimide/graphene oxide composites via in situ polymerization. Journal of Applied Polymer Science, 131, 40177-40184.

[5_30] DING, P., SU, S., SONG, N., TANG, S., LIU, Y. & SHI, L. 2014. Highly thermal conductive composites with polyamide-6 covalently-grafted graphene by an in situ polymerization and thermal reduction process. Carbon, 66, 576-584.

[5_31] JI, W.-F., CHANG, K.-C., LAI, M.-C., LI, C.-W., HSU, S.-C., CHUANG, T.-L., YEH, J.-M. & LIU, W.-R. 2014. Preparation and comparison of the physical properties of PMMA/thermally reduced graphene oxides composites with different carboxylic group content of thermally reduced graphene oxides. Composites Part A, 65, 108-114.

[5_32] CHEN, W.-Q., LI, Q.-T., LI, P.-H., ZHANG, Q.-Y., XU, Z.-S., CHU, P. K., WANG, X.-B. & YI, C.-F. 2015. In situ random co-polycondensation for preparation of reduced graphene oxide/polyimide nanocomposites with amino-modified and chemically reduced graphene oxide. Journal of Materials Science, 50, 3860-3874.

[5_33] HUANG, H.-D., REN, P.-G., XU, J.-Z., XU, L., ZHONG, G.-J., HSIAO, B. S. & LI, Z.-M. 2014. Improved barrier properties of poly(lactic acid) with randomly dispersed graphene oxide nanosheets. Journal of Membrane Science, 464, 110-118.

[5_34] MITTAL, V., CHAUDHRY, A. U. & LUCKACHAN, G. E. 2014. Biopolymer - Thermally reduced graphene nanocomposites: Structural characterization and

properties. Materials Chemistry and Physics, 147, 319-332.

[5_35] RAMANATHAN, T., ABDALA, A. A., STANKOVICH, S., DIKIN, D. A., HERRERA-ALONSO, M., PINER, R. D., ADAMSON, D. H., SCHNIEPP, H. C., CHEN, X., RUOFF, R. S., NGUYEN, S. T., AKSAY, I. A., PRUD'HOMME, R. K. & BRINSON, L. C. 2008. Functionalized graphene sheets for polymer nanocomposites. Nature Nanotechnology, 3, 327-331.

[5_36] COMPTON, O. C., KIM, S., PIERRE, C., TORKELSON, J. M. & NGUYEN, S. T. 2010. Crumpled Graphene Nanosheets as Highly Effective Barrier Property Enhancers. Advanced Materials, 22, 4759-4763.

[5_37] ETMIMI, H. M., MALLON, P. E. & SANDERSON, R. D. 2013. Polymer/graphite nanocomposites: Effect of reducing the functional groups of graphite oxide on water barrier properties. European Polymer Journal, 49, 3460-3470.

[5_38] JIN, J., RAFIQ, R., GILL, Y. Q. & SONG, M. 2013. Preparation and characterization of high performance of graphene/nylon nanocomposites. European Polymer Journal, 49, 2617-2626.

[5_39] KIM, H. & MACOSKO, C. W. 2008. Morphology and Properties of Polyester/Exfoliated Graphite Nanocomposites. Macromolecules, 41, 3317-3327.

[5_40] CHEN, J.-T., AN, Q.-F., LO, S.-C., LEE, K.-R., ZHONG, Y.-Z., LAI, J.-Y., HU, C.-C. & FU, Y.-J. 2014. Enhancing polymer/graphene oxide gas barrier film properties by introducing new crystals. Carbon, 75, 443-451.

[5_41] YOUSEFI, N., GUDARZI, M. M., ZHENG, Q., LIN, X., SHEN, X., JIA, J., SHARIF, F. & KIM, J.-K. 2013. Highly aligned, ultralarge-size reduced graphene oxide/polyurethane nanocomposites: Mechanical properties and moisture permeability. Composites Part A, 49, 42-50.

[5_42] LI, Y., UMER, R., SAMAD, Y. A., ZHENG, L. & LIAO, K. 2013. The effect of the ultrasonication pre-treatment of graphene oxide (GO) on the mechanical properties of GO/polyvinyl alcohol composites. Carbon, 55, 321-327.

[5_43] RAFIQ, R., CAI, D., JIN, J. & SONG, M. 2010. Increasing the toughness of nylon 12 by the incorporation of functionalized graphene. Carbon, 48, 4309-4314.

[5_44] YUAN, D., WANG, B., WANG, L., WANG, Y. & ZHOU, Z. 2013. Unusual toughening effect of graphene oxide on the graphene oxide/nylon 11 composites prepared by in situ melt polycondensation. Composites Part B, 55, 215-220.

[5_45] GLOVER, A. J., SCHNIEPP, H. C., KRANBUEHL, D. E., CAI, M. & OVERDEEP, K. R. 2011. In SituReduction of Graphene Oxide in Polymers. Macromolecules, 44, 9821-9829.

[5_46] CHEN, J., RADKE, W. & PASCH, H. 2003. Analysis of Polyamides by Size Exclusion Chromatography and Laser Light Scattering. Macromolecular Symposia, 193, 107-118.

[5_47] SKROVANEK, D. J., PAINTER, P. C. & COLEMAN, M. M. 1986. HYDROGEN-BONDING IN POLYMERS .2. INFRARED TEMPERATURE STUDIES OF NYLON-11. Macromolecules, 19, 699-705.

[5_48] HOCKER, S., RHUDY, A. K., GINSBURG, G. & KRANBUEHL, D. E. 2014. Polyamide hydrolysis accelerated by small weak organic acids. Polymer, 55, 5057-5064.

[5_49] JACQUES, B., WERTH, M., MERDAS, I., THOMINETTE, F. & VERDU, J. 2002. Hydrolytic ageing of polyamide 11. 1. Hydrolysis kinetics in water. Polymer, 43, 6439-6447.

[5_50] LAIDLER, K. J. 1987. Chemical Kinetics, New York, NY, Harper & Row.

[5_51] ZAHN, D. 2004a. Car-Parrinello molecular dynamics simulation of base-catalyzed amide hydrolysis in aqueous solution. Chemical Physics Letters, 383, 134-137.

[5_52] XIONG, Y. & ZHAN, C. G. 2006. Theoretical studies of the transition-state structures and free energy barriers for base-catalyzed hydrolysis of amides. Journal of Physical Chemistry A, 110, 12644-12652.

[5_53] BENDER, M. L. & THOMAS, R. J. 1961. Concurrent Alkaline Hydrolysis and Isotopic Oxygen Exchange of a Series of p-Substituted Acetanilides. Journal of the American Chemical Society, 83, 4183-4189.

[5_54] BROWN, R. S., BENNET, A. J. & SLEBOCKATILK, H. 1992. Recent

Perspectives Concerning the Mechanism of H3O+ Promoted and OH- Promoted Amide Hydrolysis. Accounts of Chemical Research, 25, 481-488.

[5_55] POLLACK, R. M. & BENDER, M. L. 1970. Alkaline Hydrolysis of Para Nitroacetanilide and Para Fromylacetanilide. Journal of the American Chemical Society, 92, 7190-7194.

[5_56] BAGNO, A., LOVATO, G. & SCORRANO, G. 1993. Thermodynamics of Protonation and Hydration of Aliphatic Amides. Journal of the Chemical Society-Perkin Transactions 2, 1091-1098.

[5_57] FERSHT, A. R. 1971. Acyl-Transfer Reactions of Amides and Esters with Alcohols and Thiols - Reference System for Serine and Cysteine Proteinases - Concerning N Protonation of Amides and Amide-Imidate Equilibria. Journal of the American Chemical Society, 93, 3504-3515.

[5_58] MARTIN, R. B. 1972. O-Protonation of Amides in Dilute Acids. Journal of the Chemical Society-Chemical Communications, 793-794.59. Kresge AJ, Fitzgera.Ph, and Chiang Y. Journal of the American Chemical Society 1974;96(14):4698-4699.

[5_59] ZAHN, D. 2004b. On the Role of Water in Amide Hydrolysis. European Journal of Organic Chemistry, 2004, 4020-4023.

[5_60] PAN, B., RICCI, M. S. & TROUTT, B. L. 2011. A Molecular Mechanism of Hydrolysis of Peptide Bonds at Neutral pH Using a Model Compound. Journal

of Physical Chemistry B, 115, 5958-5970.

[5_61] DUAN, P. G., DAI, L. Y. & SAVAGE, P. E. 2010. Kinetics and mechanism of N-substituted amide hydrolysis in high-temperature water. Journal of Supercritical Fluids, 51, 362-368.

[5_62] SCHOWEN, R. L., JAYARAMA.H, KERSHNER, L. & ZUORICK, G. W. 1966a. Solvent Isotope Effects in Amide Hydrolysis. Journal of the American Chemical Society, 88, 4008-4012.

[5_63] SCHOWEN, R. L., JAYARAMAN, H. & KERSHNER, L. 1966b. Catalytic efficiencies in amide hydrolysis. The two-step mechanism. 88, 3373-3375.

[5_64] ZAHN, D. 2003. Theoretical study of the mechanisms of acid-catalyzed amide hydrolysis in aqueous solution. Journal of Physical Chemistry B, 107, 12303-12306.

[5_65] YANG, Z., HUANG, S. & LIU, T. X. 2011. Crystallization Behavior of Polyamide 11/Multiwalled Carbon Nanotube Composites. Journal of Applied Polymer Science, 122, 551-560.

[5_66] KOLESOV, I., KACI, M., LEBEK, W., MILEVA, D., BENHAMIDA, A., FOCKE, W. & ANDROSCH, R. 2013. Crystallization of a polyamide 11/organo-modified montmorillonite nanocomposite at rapid cooling. Colloid and Polymer Science, 291, 2541-2549.

[5_67] CAPSAL, J.-F., POUSSEROT, C., DANTRAS, E., DANDURAND, J. &

LACABANNE, C. 2010. Dynamic mechanical behaviour of polyamide 11/Barium titanate ferroelectric composites. Polymer, 51, 5207-5211.

[5_68] LACRAMPE, M.-F., PRASHANTHA, K. & KRAWCZAK, P. 2013. Highly dispersed polyamide-11/halloysite nanocomposites: Thermal, rheological, optical, dielectric, and mechanical properties. Journal of Applied Polymer Science, 130, 313-321.

[5_69] PANAITESCU, D. M., FRONE, A. N. & NICOLAE, C. 2013. Micro- and nano-mechanical characterization of polyamide 11 and its composites containing cellulose nanofibers. European Polymer Journal, 49, 3857-3866.

[5_70] MAGO, G., KALYON, D. M. & FISHER, F. T. 2011. Nanocomposites of Polyamide-11 and Carbon Nanostructures: Development of Microstructure and Ultimate Properties Following Solution Processing. Journal of Polymer Science Part B-Polymer Physics, 49, 1311-1321.

[5_71] MA, Y. L., HU, G. S., REN, X. L. & WANG, B. B. 2007. Non-isothermal crystallization kinetics and melting behaviors of nylon 11/tetrapod-shaped ZnO whisker (T-ZnOw) composites. Materials Science and Engineering a-Structural Materials Properties Microstructure and Processing, 460, 611-618.

[5_72] WU, M., YANG, G., WANG, M., WANG, W., ZHANG, W.-D., FENG, J. & LIU, T. 2008. Nonisothermal crystallization kinetics of ZnO nanorod filled polyamide 11 composites. Materials Chemistry and Physics, 109, 547-555.

[5_73] ZHANG, G., LI, Y. & YAN, D. 2003. Polymorphism in Nylon-11/Montmorillonite Nanocomposite. Journal of Polymer Science Part B: Polymer Physics, 42, 253-259.

[5_74] LIU, T.-X., CHEN, D., PHANG, I. Y. & WEI, C. 2013b. Studies on crystal transition of polyamide 11 nanocomposites by variable-temperature X-ray diffraction. Chinese Journal of Polymer Science, 32, 115-122.

[5_75] ZHANG, Q. Z., MO, Z. S., LIU, S. Y. & ZHANG, H. F. 2000. Influence of annealing on structure of Nylon 11. Macromolecules, 33, 5999-6005.

[5_76] ZHANG, Q., YU, M. & FU, Q. 2004. Crystal morphology and crystallization kinetics of polyamide-11/clay nanocomposites. Polymer International, 53, 1941-1949.

[5_77] LATKO, P., KOLBUK, D., KOZERA, R. & BOCZKOWSKA, A. 2016. Microstructural Characterization and Mechanical Properties of PA11 Nanocomposite Fibers. Journal of Materials Engineering and Performance, 25, 68-75.

[5_78] KAWAGUCHI, A., IKAWA, T., FUJIWARA, Y., TABUCHI, M. & MONOBE, K. 1981. POLYMORPHISM IN LAMELLAR SINGLE-CRYSTALS OF NYLON-11. Journal of Macromolecular Science-Physics, B20, 1-20.

[5_79] FORNES, T. D. & PAUL, D. R. 2003. Crystallization behavior of nylon 6 nanocomposites. Polymer, 44, 3945-3961.

[5_80] JARRIN, J., DRIANCOURT, A., BRUNET, R. & PIERRE, B. 1998. Durability of polyamide 11 for offshore flexible pipe applications. MERL Oilfield engineering with polymers. London, UK.

[5_81] OH, Y. J., YOO, J. J., KIM, Y. I., YOON, J. K., YOON, H. N., KIM, J. H. & PARK, S. B. 2014. Oxygen functional groups and electrochemical capacitive behavior of incompletely reduced graphene oxides as a thin-film electrode of supercapacitor. Electrochimica Acta, 116, 118-128.

[5_82] HOCKER, S., HUDSON-SMITH, N., SCHNIEPP, H. C. & KRANBUEHL, D. E. 2016. Enhancing polyimide's water barrier properties through addition of functionalized graphene oxide. Polymer, 93, 23-29.

5.6 Supplementary Data

Hydrogen bonding in the PA11 matrix is an intermolecular interaction between the amide hydrogen and the carbonyl oxygen of a neighboring amide bond. Skrovanek, Painter [47] first studied the use of FTIR to detect hydrogen bonding interactions within a PA11 polymer. Skrovanek, Painter [47] found de-convoluting the 1635 cm^{-1} peak of the carbonyl oxygen revealed three peaks that could be characterized at 1635, 1654, and 1684 cm^{-1}. The 1635 sub-peak is a lower energy carbonyl vibration correlated to aligned hydrogen bonding. The 1654 peak is un-aligned amorphous hydrogen bound carbonyl oxygens. And, the 1684 peak is correlated with carbonyl oxygen groups that are free of hydrogen bonding. Following the work of Skrovanek, Painter [47] the amide bond 1635 cm^{-1} peak of the carbonyl oxygen was de-convoluted to probe the hydrogen bonding interactions at the amide bond. Through deconvolution of the 1635 cm^{-1} amide C=O, no difference was observed at the carbonyl oxygen peaks for PA11 and GO-PA11.

Attenuated Total Reflectance Fourier Transform Infrared Spectroscopy (ATR-FTIR) spectra was taken using an IR Tracer-100 Shimadzu FTIR with a MIRacle 10 Single Reflectance ATR accessory, a resolution of 2 cm^{-1}, and averaged from 32 scans between 600 to 4000 cm^{-1}. After adjusting to a common baseline and normalizing to peak 2851 cm^{-1}, the work of Skrovanek, Painter [47] was followef to de-convolute the 1635 cm^{-1} carbonyl oxygen peak using MagicPlot Student 2.5.1 software and measure the relative concentration of free and hydrogen bound

amide oxygen groups characterized at 1635, 1654, and 1684 cm^{-1} peak positions. The heights of the de-convoluted peaks were used to compare the relative concentration of hydrogen bound carbonyl oxygen groups.

We normalized each spectra using a multi-point baseline and then normalized the spectrum to the symmetric aliphatic C-H stretch at 2851 cm^{-1}. The deconvolutions were performed between 1590 and 1800 cm^{-1} using MagicPlot Student 2.5.1 software, Figure 5-15 - Figure 5-23. Two additional peaks were observed near 1725 and 1618 cm^{-1}.

Figure 5-12, Figure 5-13, and Figure 5-14 are bar plots of the peak heights for the best fit de-convoluted 1684, 1654, and 1635 peaks respectively. The 1635 peaks are lower energy carbonyl vibrations correlated to stronger oriented hydrogen bonding. The 1654 peak is un-aligned amorphous hydrogen bound amide bond carbonyl oxygen. The 1684 peak is correlated with carbonyl oxygen groups that are free of hydrogen bonding. Figure 5-14 shows that from our de-convolution fits, the PA11 and 1-GO-PA11 have the nearly the same content of free carbonyl acid groups before and after aging, no change in the hydrogen bonding behavior at the carbonyl amide oxygen. Instead we saw an effect at the amide N-H peak, 3305 cm^{-1}.

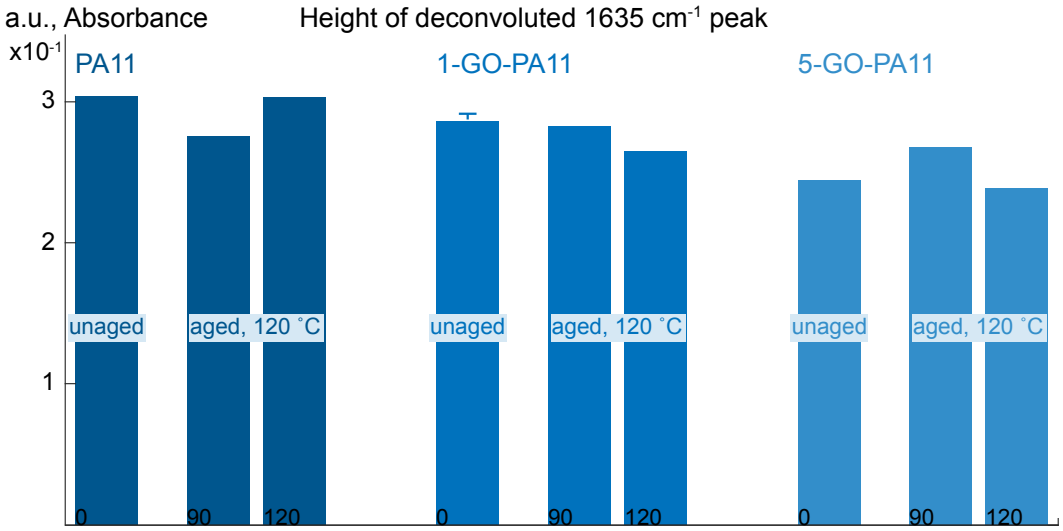

Figure 5-12: The deconvoluted peak heights centered at 1635 cm^{-1} are grouped based on material; PA11, 1-GO-PA11, and 5-GO-PA11; then by unaged and aged at 120 ˚C for 90 and 120 days.

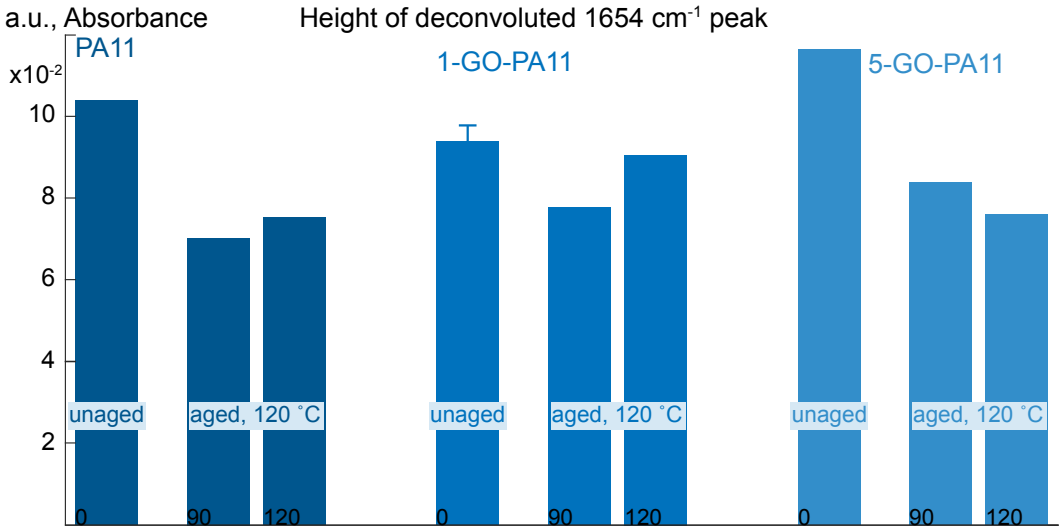

Figure 5-13: The deconvoluted peak heights centered at 1654 cm^{-1} are grouped based on material; PA11, 1-GO-PA11, and 5-GO-PA11; then by unaged and aged at 120 ˚C for 90 and 120 days.

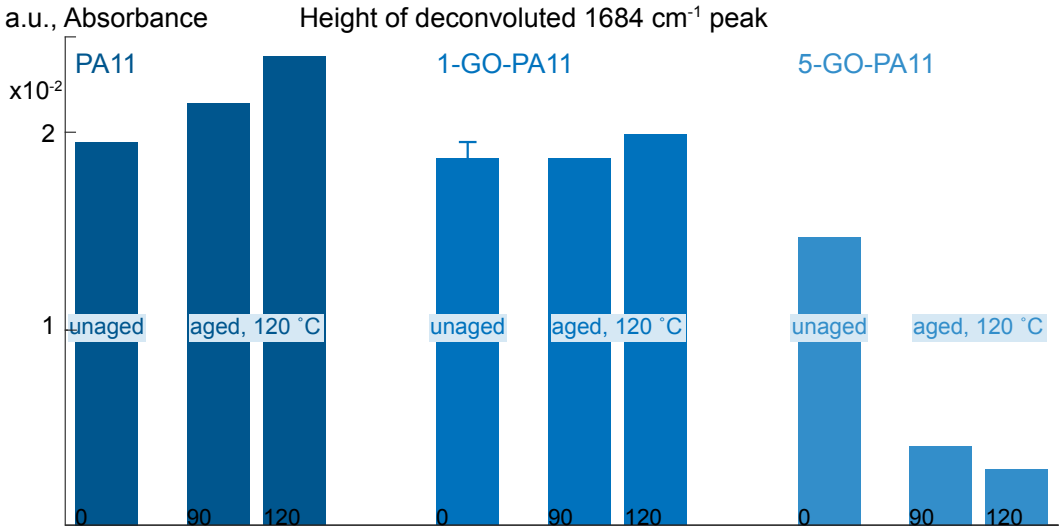

Figure 5-14: The deconvoluted peak heights centered at 1684 cm^{-1} are grouped based on material; PA11, 1-GO-PA11, and 5-GO-PA11; then by unaged and aged at 120 ˚C for 90 and 120 days.

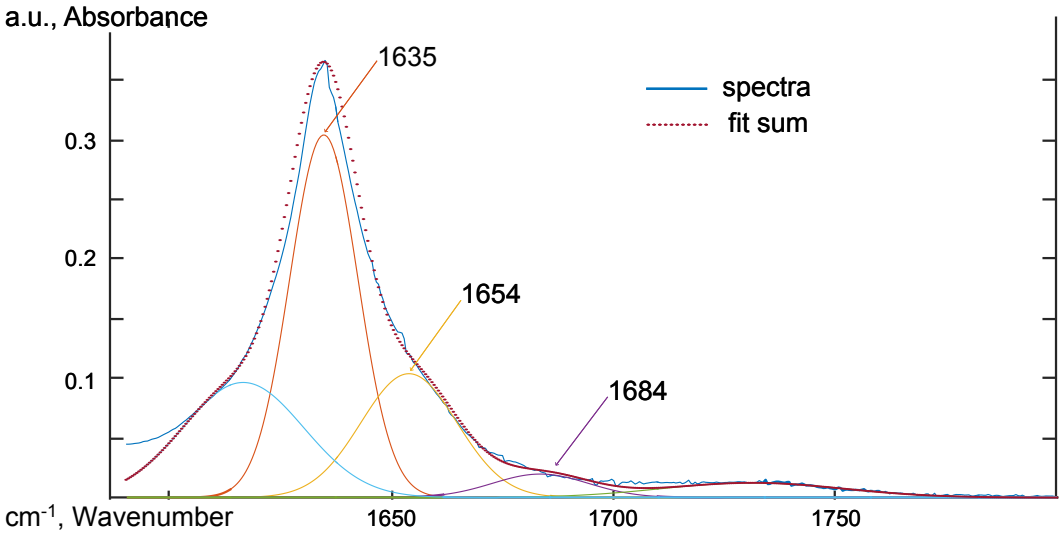

Figure 5-15: PA11, ATR-FTIR spectra between 1590 and 1800 cm^{-1} de-convoluted using Gaussian peak shapes at 1635, 1654, and 1684 cm^{-1}.

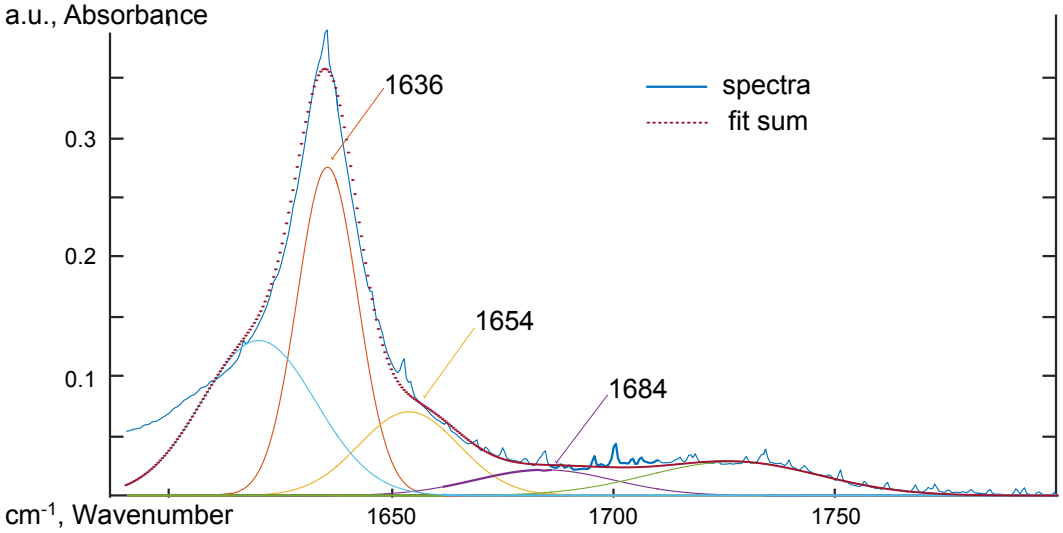

Figure 5-16: PA11 aged 90 days at 120 ˚C, ATR-FTIR spectra between 1590 and 1800 cm^{-1} de-convoluted using Gaussian peak shapes at 1635, 1654, and 1684 cm^{-1}.

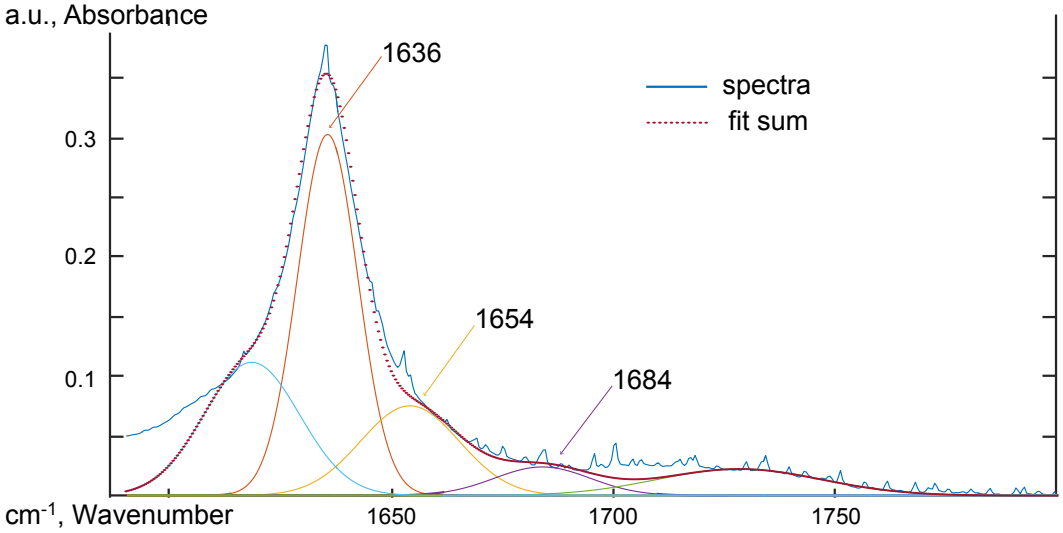

Figure 5-17: PA11 aged 120 days at 120 ˚C, ATR-FTIR spectra between 1590 and 1800 cm^{-1} de-convoluted using Gaussian peak shapes at 1635, 1654, and 1684 cm^{-1}.

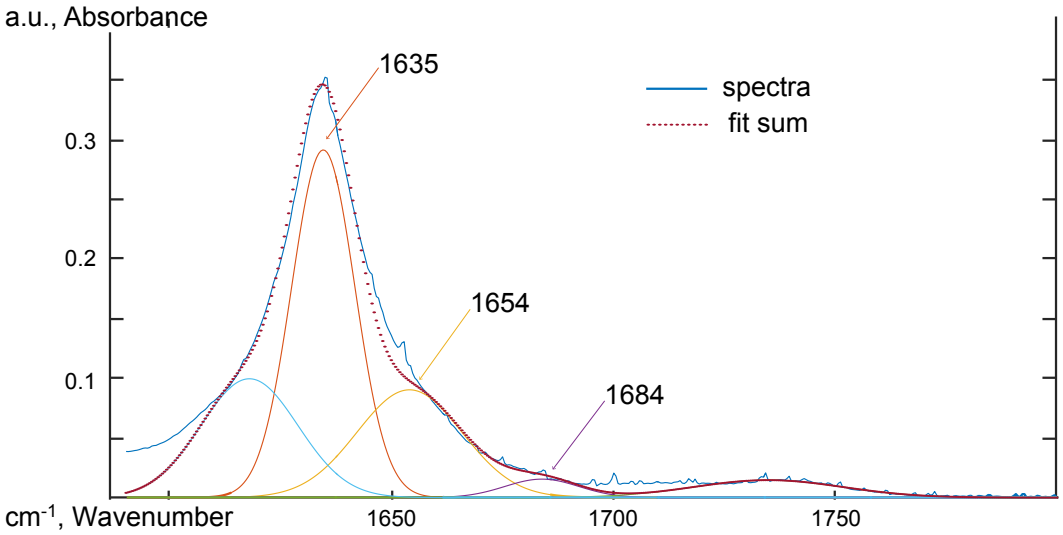

Figure 5-18: 1-GO-PA11, ATR-FTIR spectra between 1590 and 1800 cm^{-1} deconvoluted using Gaussian peak shapes at 1635, 1654, and 1684 cm^{-1}.

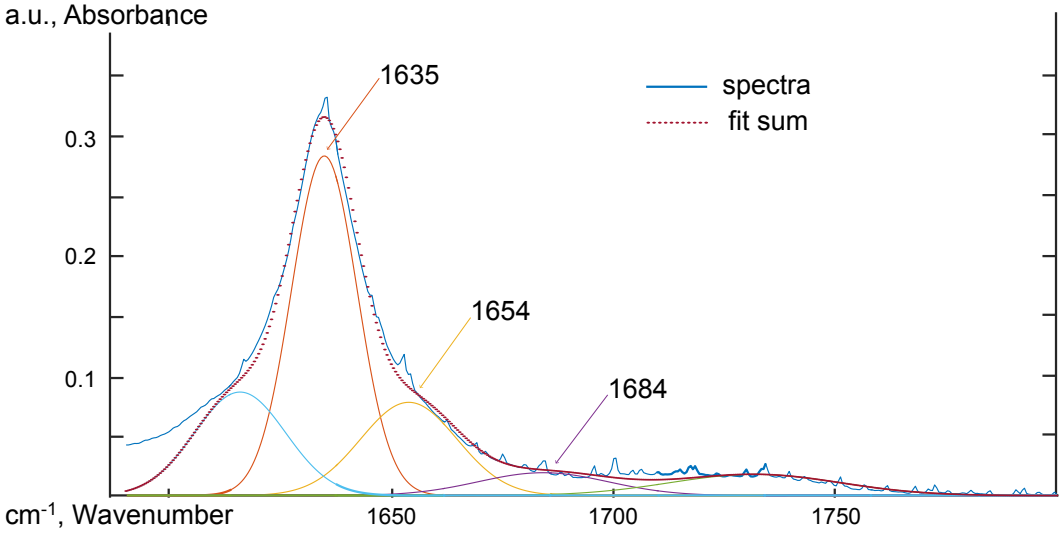

Figure 5-19: 1-GO-PA11 aged for 90 days at 120 ˚C, ATR-FTIR spectra between 1590 and 1800 cm^{-1} de-convoluted using Gaussian peak shapes at 1635, 1654, and 1684 cm^{-1}.

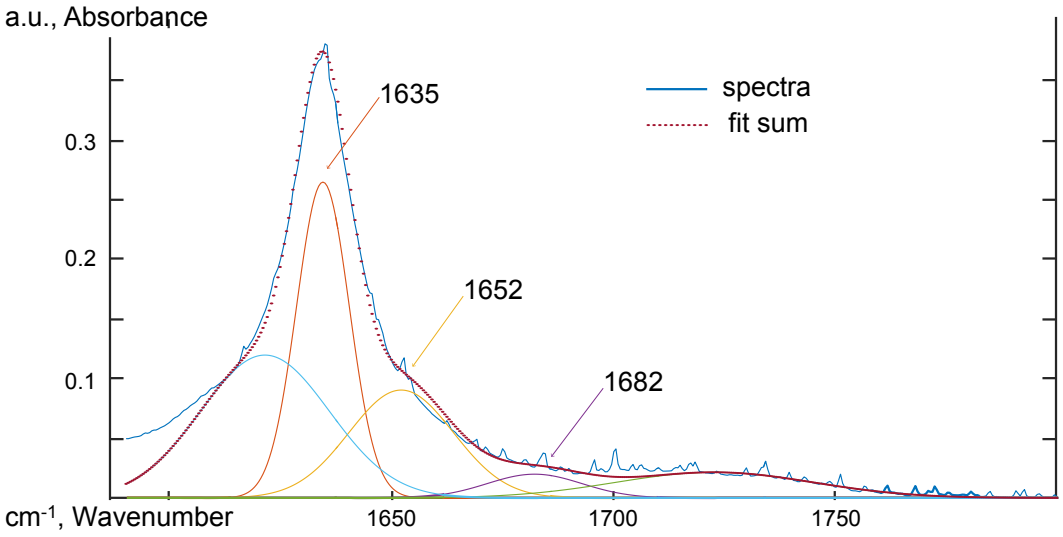

Figure 5-20: 1-GO-PA11 aged 120 days at 120 ˚C, ATR-FTIR spectra between 1590 and 1800 cm^{-1} de-convoluted using Gaussian peak shapes at 1635, 1654, and 1684 cm^{-1}.

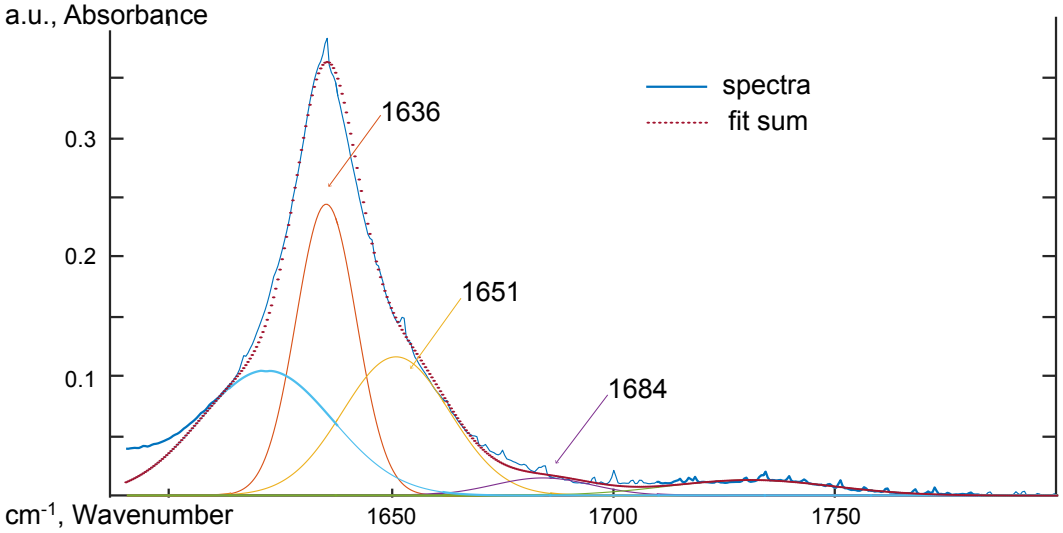

Figure 5-21: 5-GO-PA11, ATR-FTIR spectra between 1590 and 1800 cm^{-1} deconvoluted using Gaussian peak shapes at 1635, 1654, and 1684 cm^{-1}.

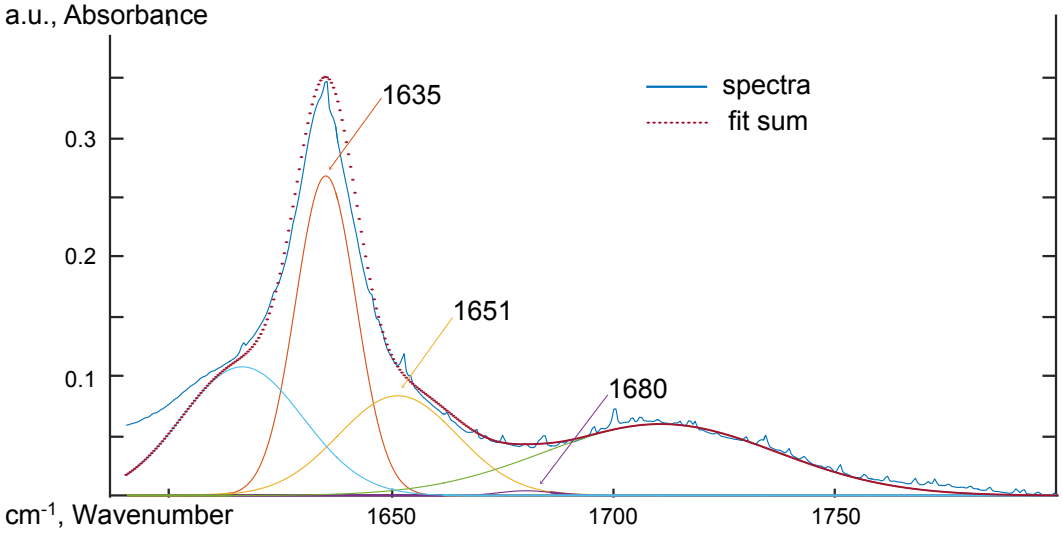

Figure 5-22: 5-GO-PA11 aged 90 days at 120 ˚C, ATR-FTIR spectra between 1590 and 1800 cm^{-1} de-convoluted using Gaussian peak shapes at 1635, 1654, and 1684 cm^{-1}.

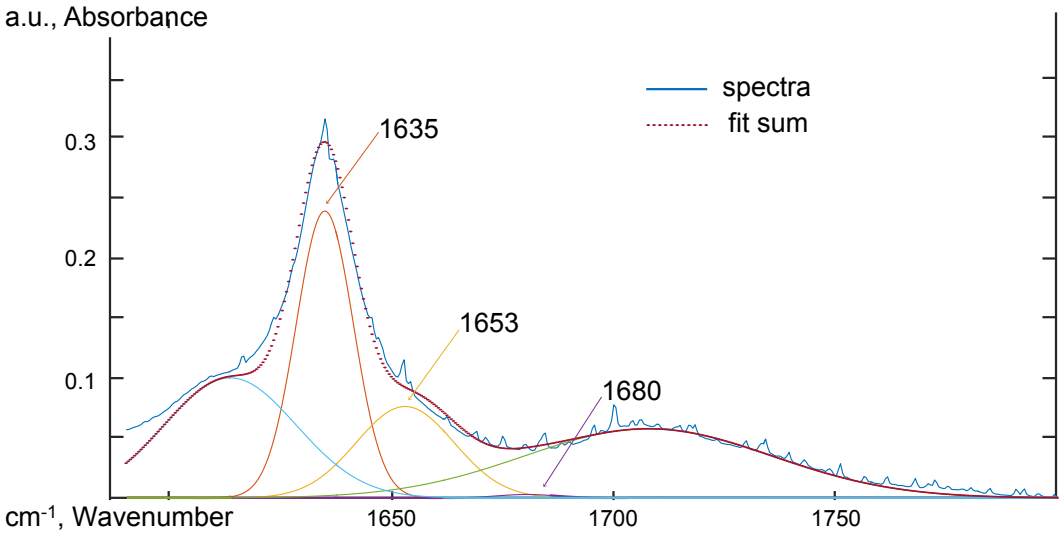

Figure 5-23: 5-GO-PA11 aged 120 days at 120 ˚C, ATR-FTIR spectra between 1590 and 1800 cm^{-1} de-convoluted using Gaussian peak shapes at 1635, 1654, and 1684 cm^{-1}.

Chapter 6

Enhancing Polyimide's Water Barrier Properties through Addition of Functionalized Graphene Oxide

6.1 Introduction

Polyimides (PI) are a family of high-performance polymers that derive excellent mechanical strength, thermal resistance, and chemical resistance from their stable and stiff imide bonds. As a result, polyimides can be found in a wide array of industrial applications such as electric motors, jet engine blades, aircraft wire, and molded pistons and seals. Recent aerospace applications of PI films include the Mars Explorers Curiosity and Spirit [1], the European Space Agency's Rosetta space probe [2], and the sun shield of NASA's James Webb Space Telescope [3]. In all of the PI applications, efficiency can be improved by using less material to effect the same utility. Additionally, in some cases, the use of PI can enable new applications or technologies in extreme environments, e.g. outer space. In a global effort to make better and enabling materials, many different fillers and nano-fillers have been researched for polyimide composites and nano-composites. In recent years, graphene has been researched as a nano-filler to make polyimide nanocomposites with new and advantageous properties.

Research in graphene-PI nanocomposites has been motivated by lending graphene's extremely high modulus of 1 TPa, ultimate strength of 130 GPa, gas impermeable honeycomb network, and high electrical and thermal conductivity [4] to the polymer matrix. A challenge in creating graphene-polymer nanocomposites is graphene's extremely hydrophobic and chemically unreactive pristine carbon-honeycomb structure. It is difficult to disperse graphene single layer nano-sheets into the polar solvents typically used for polymerization and synthesis.

The increased interest in graphene's exceptional properties has revitalized interest in an analogous polar compound, graphene oxide (GO). GO has the same honeycomb structure as graphene but with oxygen-containing functional groups on the surface of the planar structure. These oxygen-containing functional groups are ketones, 6-membered lactol rings, alcohols, epoxides and hydroxyl groups [4]. First produced in 1859 by Brodie [5] and later by Hummers Jr. and Offeman [6], graphitic oxide can be dispersed into water or organic solvents commonly used in polymer precursor resins to create GO-polymer composite materials [4]. A wide range of GO-polymer nanocomposites have been researched previously for polyurethanes, nylons, and many other polymers including several PI systems, with as many variations on GO synthesis, functionalization, and composite fabrication technique [4, 7-17]. Many GO-PI works show improvements in Young's modulus [18-20], tensile strength [18, 20], gas barrier properties [19, 21], electrical conductivity [19, 20, 22], and decreases in thermal stability [19, 22].

Regarding tensile modulus and strength improvements published on loading GO into PI, Wang, Yang [23] used loadings of 0.3 to 5 wt% and found a maximum 1400 % increase in tensile modulus and a 990 % increase in tensile strength for GO sheets functionalized with 4-4' oxydianiline (ODA) in a PI of the monomers 3,3,4,4-benzophenonetetracarboxylic dianhydride (BTDA) and ODA. Tseng, Liao [24] used very low loadings of GO in a PI of bicyclo[2.2.2]oct-7-ene-2,3,5,6-tetracarboxylic dianhydride and ODA, between 0.001 and 0.01 wt% to effect 66 % improvement in the tensile modulus while maintaining optical transparency. Shi,

Li [18] found an increase of tensile strength by 29 % and Young's modulus by 25 % with an addition of 0.12 wt% GO in a PI system comprised of 4,4'-bisphenol A dianhydride, 4-4'-oxydiphthalic anhydride and diaminophenyl methane. Zhu, Lim [19] found an increase of the Young's modulus by 282 % in a 30 wt% GO-PI system comprised of the monomers pyromellitic dianhydride and ODA. Park, Kim [20] found an increase of 172 % in the modulus and an 64 % increase in tensile strength with the addition of 0.5 wt% of surface functionalized GO in PI system compromised of pyromellitic dianhydride and ODA. Qian, Wu [25] with a PI of 3,3,4,4-Biphenyl teracarboxylic dianhydride and ODA monomers showed a 79 % improvement in the tensile strength and a 132 % increase in the tensile modulus are achieved by adding 1.5 wt% 3-aminopropyltriethoxysilane functionalized GO. Wang, Lan [26] loaded 3 wt% amino functionalized GO into PI of 3,3,4,4-Biphenyl teracarboxylic dianhydride and p-phenylenediamine monomers to effect 63 % increase in modulus and 55 % increase in the tensile strength. Over the past few years, papers have reported on the increased effect on mechanical performance properties by functionalizing the surface of GO. A few papers have focused on comparing the effect of different functionalizing procedures on the improvement on performance properties, primarily in epoxies[27-30] and in polyimides[20, 31-33].

Regarding gas barrier properties of GO loaded PI films: Zhu, Lim [19] determined that incorporation of GO nano-sheets from 1 to 30 wt%, reduced the oxygen transmission rate through the PI film with a maximum reduction of 93 %. Lim, Yeo [31] report a reduction in oxygen permeability of a factor of 95 %

at 0.5 wt% and a reduction of >99% at 5 wt%. Park, Kim [20] using 2 wt% iodo-functionalized GO found a 73 % decrease of water vapor transmission in their PI system. Tseng, Liao [24] at the very low GO loadings of 0.001 to 0.01 wt% found a maximum of 90% decreased water vapor transmission rate in the GO-PI nano-composite. Kwon and Chang [34] investigated the gas permeability of GO-PI and organically modified hectorite clay, and functionalized hexadecylamine-graphene sheets. They found that from 3 to 20 wt% loadings of functionalized hexadecylamine-graphene sheets in PI of 4,4-biphthalic anhydride (BPA) and bis(4-aminophenyl) sulfide (APS), the oxygen transmission decreased 48 % to 92 %, respectively. From this brief literature review of GO-PI and functionalized GO-PI nanocomposite it is clear that the gas or water vapor permeability and tensile properties are improved, but the properties vary according to the polyimide used and the surface chemistry of the graphene oxide.

In order to understand the molecular interactions between the polymer and GO that lead to gas permeability and tensile improvements, two types of GO-PI composite films are synthesized with very low 0.01, 0.03, 0.06, and 0.1 wt% GO loadings. The loading of 0.01 wt% is a factor of ten lower GO-PI loading than the commonly used particle loadings in polymers. The two types of GO-PI composites synthesized differ in their GO surface chemistry. The first type uses as produced GO and then was thermally reduced during in-situ PI synthesis at 300 ˚C [33]. In the second type, GO was reacted with the ODA monomer to make ODAGO prior to being added to the polyamic acid resin and thermally imidized at 300 ˚C to

become ODAGO-PI.

The differing effect on performance properties of functionalized versus un-functionalized is explored for the first time at these very low concentrations through water vapor barrier, water uptake, and tensile measurements on both types of composites. The variation in improvement of the GO composite's properties presents a systematic comparison of the effect of functionalized GO on composite properties. The results show the important fact that large improvements can be found in the performance properties at these much lower loadings of GO, as low as 0.01 wt%, and that use of functionalized GO produces significantly greater improvements than the widely used as-produced GO. Additionally, the effect of hydrogen bonding between the nano-sheets and the polymer matrix was identified. This bonding stiffens the polymer chains, decreasing gas permeability and increasing the tensile modulus beyond the usual effect of GO's high aspect ratio sheet structure and high modulus.

6.2 Experimental

6.2.1 GO Synthesis and Dispersion

GO was obtained by the synthesis procedure of Hummers[6]. Dry GO flakes were massed and added to a flask of DMAc. This mixture was bath sonicated in water using a Fisher Scientific FS110D sonicator for 30 minutes to result in a homogenous GO-DMAc dispersion. To perform topographical characterization of the exfoliated flake height, a Laurell WS-400Bz-6NPP-Lite Spin Processor was used to disperse samples of each dispersion onto freshly cleaved muscovite mica substrates (Ted Pella, PELCO®, Grade V5). Then, two atomic force microscopes (Bruker, MultiMode and NT-MDT, NTEGRA) were used to perform dynamic-mode scans of the substrates, obtaining height data on individual flakes.

6.2.2 Functionalization of GO Particles with ODA

Under nitrogen, an ODA-DMAc solution was added to a GO-DMAc dispersion at a ratio of 15 mmol ODA per gram of GO. The ODA reacted with the GO under a nitrogen flush 60 °C reflux for 24 hours to yield a dispersion of functionalized GO, designated ODAGO.

6.2.3 Polyimide Synthesis

The polyimide precursor, poly(amic acid)(PAA), was prepared from the monomers benzophenone-3,3' 4,4'-tetracarboxylic dianhydride (BTDA) and 4-4' oxydianiline (ODA). Prior to use, BTDA was dried in a vacuum oven at 150 °C for 5 hours. Equimolar amounts of ODA and dry BTDA were independently dissolved into dimethylacetamide (DMAc) to make two solutions. The dissolved BTDA was added to a three-necked resin flask, followed by the ODA solution. The reaction was stirred at room temperature under nitrogen for 48 hours. The resulting poly(amic acid) resin (PAA) was obtained at 12 wt% solids in DMAc and was used for the synthesis of both unloaded and loaded PI composite films[35].

An even layer of PAA was spread into a soda lime glass petri dish and this dish of PAA was then placed into a Thermolyne 47900 Furnace to obtain a solid PI film. Thermal cure was a ramp to 100 °C with a one hour isotherm followed by a 2 hour ramp to 300 °C with a one hour isotherm, and returned back to room temperature. The PI film was easily peeled from the glass and characterized[35].

6.2.4 GO Nanocomposite Synthesis

A solvent mixing technique was used to make the ODAGO-PI and GO-PI. The GO-DMAc dispersion was mixed with the PAA to make GO-PAA. ODAGO-DMAc was mixed with the PAA to make ODAGO-PAA. GO and ODAGO were added at

0.01, 0.03, 0.06 and 0.10 wt% per PAA solids. The GO-PAA and ODAGO-PAA were spread into petri dishes and subjected to the same cure cycle used to produce the PI films.

6.2.5 Raman Spectroscopy

Raman measurements were performed on an inverted microscope (Nikon, TiU) with a laser wavelength of 632.8 nm from a HeNe laser (Research Electro-Optics, LHRP-1701) with an excitation power of 2 mW. The laser was filtered (Semrock, LL01-633-25) and focused to the sample using a 20× objective (Nikon CFI, N.A. = 0.5). Scattering from the sample was filtered (Semrock, LP02-633RS-25) and focused to the entrance slit of the spectrograph (Princeton Instruments, SP2356, 600 g mm−1 grating blazed at 500 nm). The observed Raman frequencies were calibrated using a cyclohexane standard[36].

6.2.6 Water Vapor Transmission

Water vapor transmission rates were measured using ASTM E96-95: Methods for Water Vapor Transmission of Materials. Samples were cut by hand into approximately 1.5 cm squares. Thickness dimensions of approximately 0.05 mm were measured with a iGaging EZ-Cal digital micrometer.

For each sample, a cylindrical vial was filled to approximately 75% capacity

with the desiccant Drierite with color indicator (Acros Organics). Per vial, the rim was coated with silicon vacuum grease. A square sample of the PI films was placed on top of each vial rim and the vacuum grease created a seal between the PI film and the glass to prevent water vapor passage. The vials were placed in a 70% humidity sealed environment at 23 ˚C. Following ASTM E96-95, the mass of each vial was measured over time. The rate of change of mass versus time was used to calculate our relative water vapor transmission rate. Three to seven samples were measured at each weight percent, the averages and standard deviations were reported. Measurements were also made on Kapton Type HN 25 μm film and the DuPont reported permeability value was used as a standard when the water vapor transmission rates were converted to permeability[39].

6.2.7 Water Absorption Analysis

Water absorption was determined using the procedure designated in ASTM D750- 98 standard test: Method for Water Absorption of Plastics. Polymer samples were cut into 1 × 3 cm strips with an average thickness of 50 μm. The strips were left in a 100 °C oven for an hour prior to immersing in water to remove any deposited ambient humidity. The strips were then submerged in deionized water and kept at 23 ˚C. After 24 hours, measurements were made on three to five samples and the averages and standard deviations were reported.

6.2.8 Mechanical, Tensile Testing

A TA Instruments AR 100 instrument was fitted with adjustable film grips to follow ASTM D882-73. The tensile stress/strain plots were produced to obtain Young's modulus on 5 to 15 samples. Averages and standard deviations were calculated and reported.

6.2.9 Attenuated total reflectance-Fourier transform infrared spectroscopy (ATR-FTIR)

Samples of ODAGO were prepared for ATR-FTIR by taking an aliquot of the ODAGO-DMAc dispersion and adding isopropyl alcohol drop wise until the ODAGO particles precipitated out of suspension. The precipitated dispersion was centrifuged at 5000 RPMs for 10 minutes in a Universal 320 Centrifuge. The supernatant was poured off and 5 mL of DMAc was added to dissolve any unreacted ODA. The centrifugation and DMAc washing was repeated three times. After the third wash, the ODAGO solids were removed and dried in a 55 °C vacuum oven at 23inHg for 48 hours. Dry, solid ODA-GO spectra from 600 to 4000 cm^{-1} were obtained using the IRTracer-100 Shimadzu FTIR's MIRacle 10 Single Reflectance ATR Accessor.

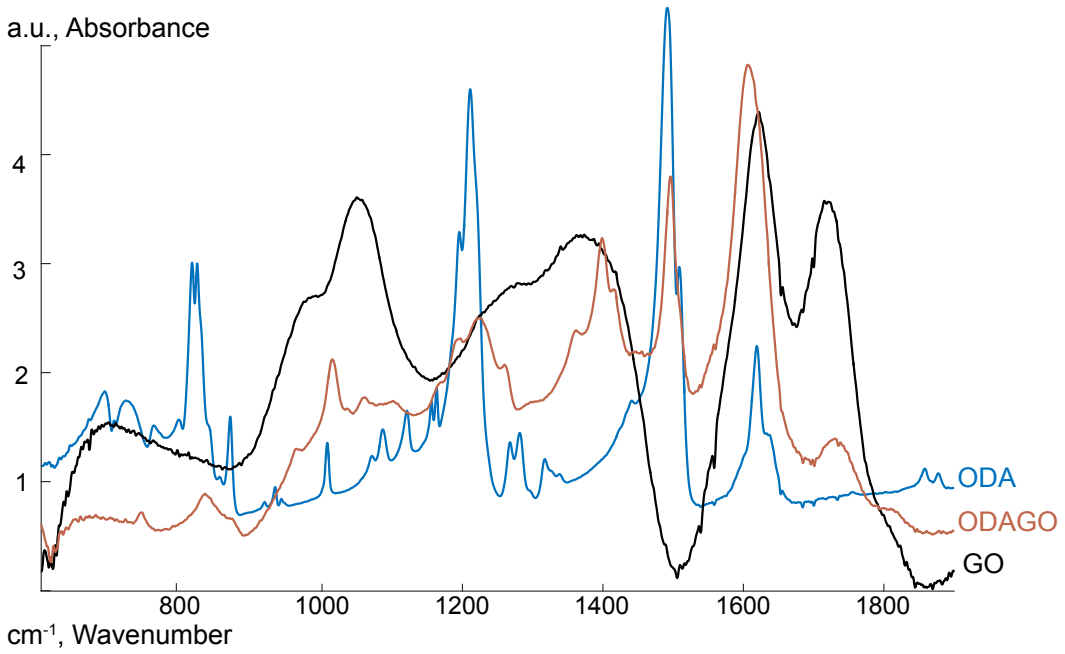

Figure 6-1: ATR-FTIR normalized absorbance spectra of ODA, ODA-GO and GO.

The spectra are shown in Figure 6-1. For the unreacted GO spectrum, characteristic peaks include 1050, 1620 and 1720-30 cm^{-1}. The 1050 cm^{-1} peak is a C-O vibration of an epoxy group. The 1620 cm^{-1} peak is the C=C stretch along the graphene plane. The 1720-1730 cm^{-1} peak is the C=O stretch. Unique to the ODAGO spectrum, the new peak at 1390 was the amide III peak that indicates amide bonds were formed in the ODAGO. In addition, there was a new peak at 743 cm^{-1}, not seen in the ODA nor in the GO, which was the N-H stretch of an amide bond. Further the alkoxide/epoxide peak in the GO spectrum at 1050 cm^{-1} was absent in the ODAGO spectrum showing the epoxide groups have reacted. On the graphene surface, the amine groups of ODA monomer were expected to react first with the epoxy groups as that peak was absent in the ODAGO, followed by reactions with the less reactive oxide groups such as C=O. The carboxylic group 1732 cm^{-1} peak in the ODAGO was reduced in height compared with the peak in the GO. In summary, the appearance of amide peaks as well as peaks absent in the ODAGO spectra compared to the reagents used for its synthesis indicate that the ODA chemically reacted with the GO and functionalization was successful.

6.2.10 Atomic Force Microscopy of GO and ODAGO Nano-sheets

High resolution atomic force microscopy (AFM) images of the GO and ODAGO sheets are shown in Figure 6-2 The range of lateral diameters for GO flakes was observed to be 300 to 1200 nm with most GO observed to be ~800 nm.

From the profile, ODAGO is approximately 0.5 nm to 1 nm thicker than GO. The functionalized surface is observed to much rougher in Figure 6-2 than GO due to the ODA monomer.

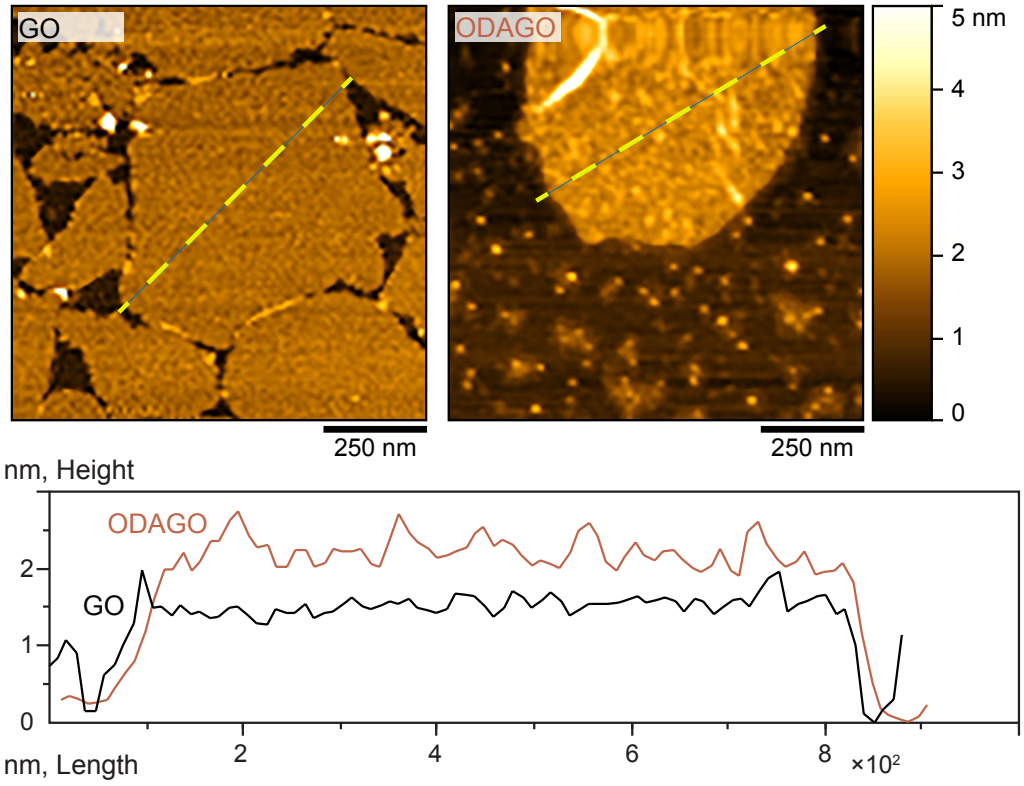

Figure 6-2: Atomic force microscope images and profiles of graphene oxide (GO) and ODA functionalized graphene oxide (ODAGO).

6.2.11 Raman Spectra

Raman measurements were performed on an inverted microscope (Nikon, TiU) with a laser wavelength of 632.8 nm from a HeNe laser (Research Electro-Optics, LHRP-1701) with an excitation power of 2 mW. The laser was filtered (Semrock, LL01-633-25) and focused to the sample using a 20× objective (Nikon CFI, N.A. = 0.5). Scattering from the sample was filtered (Semrock, LP02-633RS-25) and focused to the entrance slit of the spectrograph (Princeton Instruments, SP2356, 600 g mm^{-1} grating blazed at 500 nm). The observed Raman frequencies were calibrated using a cyclohexane standard[36].

The so-called D and G peak intensities (ID and IG) of the Raman spectra peaks of 1350 and 1600 cm^{-1} respectively, can be related to the integrity of the GO honeycomb carbon lattice. The G peak is associated with sp^2 hybridized carbon of the carbon honeycomb lattice. The D peak relates to sp^3 hybridized carbon, and is associated with defects in the graphene carbon lattice[37]. The measured I_D/I_G ratio for GO is 1.03 and the I_D/I_G ratio for ODAGO is 1.16, in Figure 6-3. Since the I_D/I_G ratios remain similar after functionalization with ODA, the Raman confirms that the impermeable GO honeycomb carbon lattice is maintained for the ODAGO nano-sheets.

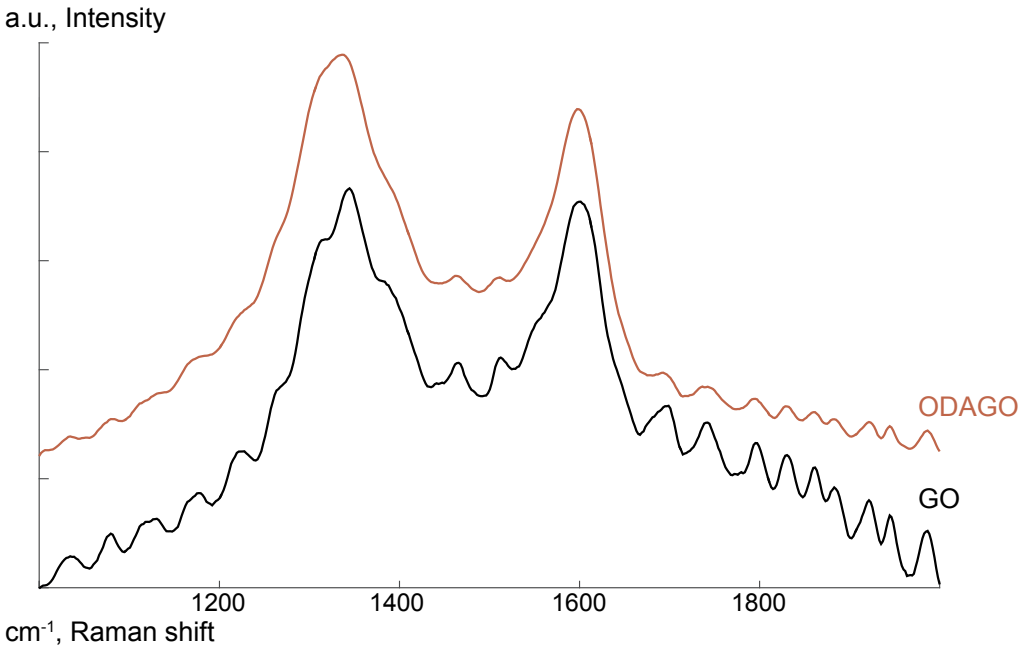

Figure 6-3: Raman Spectra of GO and ODAGO.

6.3 Results and Discussion

6.3.1 Permeability

Water vapor permeability was significantly reduced as a result of incorporation of functionalized ODAGO compared to un-functionalized GO nano-particles in the PI matrix. A plot of permeability versus PI composition is shown in Figure 6-4. The functionalized ODAGO-PI has a two to threefold greater reduction in water vapor or permeability than GO-PI samples. The ODAGO-PI composite films had a ten-fold reduction in water vapor transmission compared to the neat PI film. The 0.1 wt% ODAGO-PI films had the highest reduction in water vapor permeability, over a factor of ten compared to the unloaded PI film.

GO-PI films also reduced water vapor transmission but were less effective at preventing water vapor transmission as ODAGO-PI films. At 0.01 wt%, the GO-PI film demonstrated a 5-fold reduction of water vapor transmitted compared to the neat system. The 0.1 wt% GO-PI had a 10-fold reduction in water vapor transmission compared to the neat sample. The 0.1 wt% GO-PI had a greater permeability than 0.01 wt% ODAGO-PI but the ODAGO-PI composite achieved this reduction at a 10-fold lower loading than the GO-PI film.

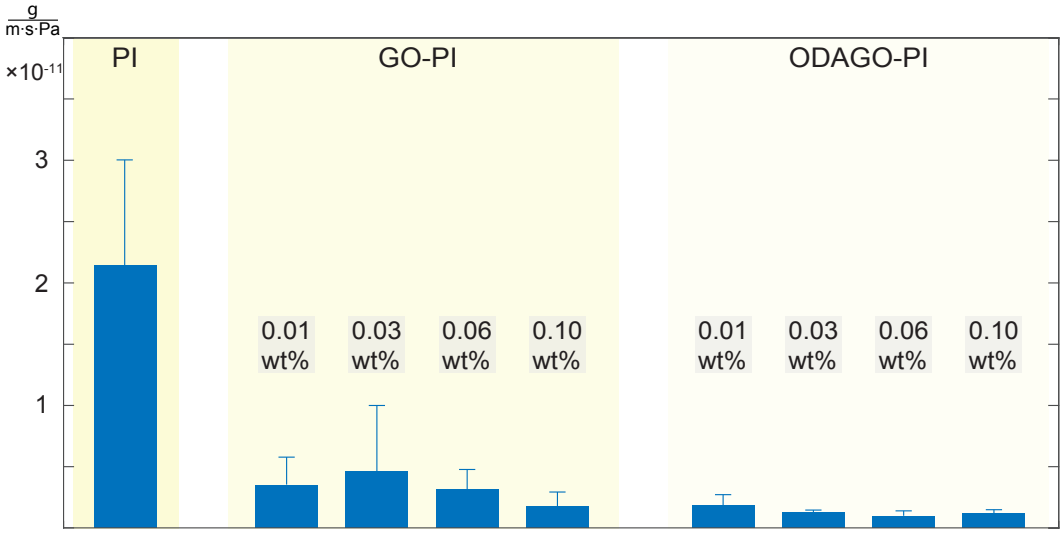

Figure 6-4: Water vapor permeability for unloaded PI, GO-PI, and ODAGO-PI films at 23 ˚C and 70% humidity.

Previous work done by Zhu et al. while studying oxygen transmission rate of a different PI film GO nanoparticle system showed a 73 % decrease of water vapor transmission by inclusion of iodo-functionalized GO sheets at 0.2 and 1 wt%. This 73 % at double to ten times the herein GO percent loading compares to the 90% reduction in ODAGO-PI. Recently, Tseng et al[24] reported a water vapor transmission reduction of 91 % at 0.01 wt% GO loading and a decrease of 83 % in water vapor transmission by inclusion of 0.0001 wt% GO in a different PI matrix. The herein results and those of Tseng show the potential for very large reductions in water vapor transmission at very low GO nanoparticle concentrations, especially when compared with previous results on gas transmission for polymer nano composites containing organo-clay[34, 40]. Most important, these results demonstrate that very low GO concentrations show a 2 to 3-fold decrease in water vapor transmission using functionalized GO compared to un-functionalized GO.

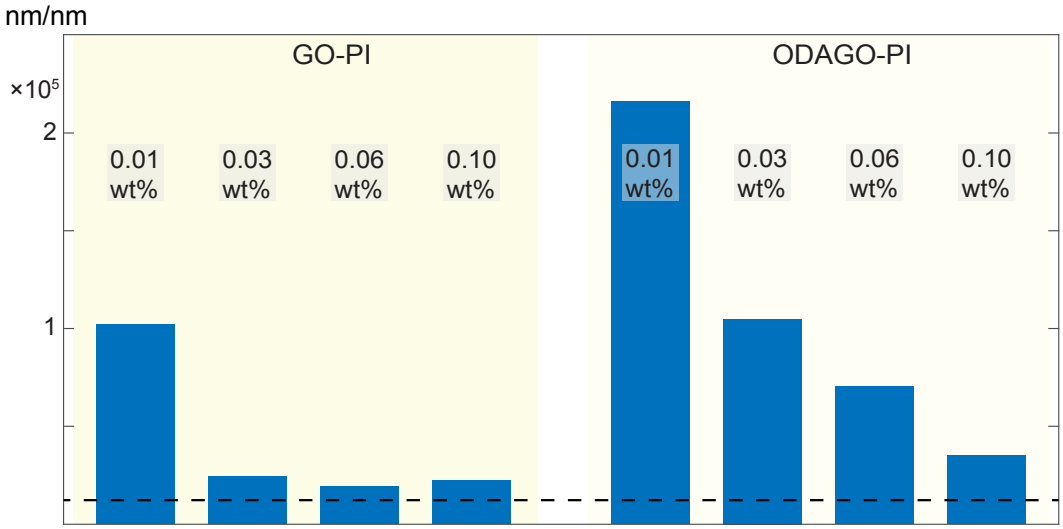

Figure 6-5: Calculated aspect ratio of the nanoparticles in the PI nanocomposites where the dashed line is for a value of 1000, an average aspect ratio for GO.

To explain and expand upon the surprising effect of the nanosheets on the water vapor permeability, the results were analyzed using the Nielsen equation for describing the tortuosity effect for a polymer filled with plate-like particles[41]. The Nielsen Equation 6-1 can be used to calculate the effective aspect ratio of the particles in the composite from the decrease in the permeability,

Equation 6-1:

$$P_c = \frac{P_f\,(1-V_f)}{1+{}^{a}/_{2} \times V_f}$$

Herein P_c is the composite permeability, P_f is the neat film permeability, V_f is the nanoparticle volume fraction, and a is the aspect ratio, where the diameter (D) of the nanoparticle is divided by the thickness (T). Figure 6-5 shows the nanoparticle aspect ratios calculated for the GO and ODA GO films. Using an approximate diameter of 800 nm and thickness of 1.5 nm for the GO and 2 nm for the ODAGO, their expected aspect ratios are 530 and 400 to compare with the Nielsen model.

The modeled aspect ratios are calculated to be much greater than the AFM measured aspect values, particularly at the lowest loadings. The ODAGO aspect ratios are higher than those for GO. The values decrease as the loading gets larger. The modeled aspect ratios appear to approach experimental AFM particle size measurements as the loading increases.

These results suggest another factor in addition to the tortuosity effect induced

by the high aspect ratio is producing the significant reduction in permeability at the weight percent of 0.01 percent. One factor known to correlate with reduction in permeability is reduction in mobility of the polymer chain. A reduction in chain mobility in a polymer can be examined by the effect of the nanoparticle on the crystalline and glass phase transitions. It has been shown that GO nanoparticles inhibit crystallization in clay polyamide polymers[42-49]. The effect has been described as due to an interaction of the nanoparticle's surface with the polymer chain resulting in a region of constrained polyamide chain mobility. Similar effects of GO on the crystallization of polyamide-11 have been observed and are a focus of ongoing work on GO's inhibiting hydrolytic degradation.

As polyimides are amorphous glassy materials, measurements of the glass transition using a 30 $^{\circ}C/_{min}$ ramp were made. The results in Figure 6-6 show an increase in T_g at the highest weight percent. The nano-sheets inhibition of chain mobility as seen by an increase in T_g and the effect of clay and GO nanoparticles on polyamide crystallization support the view that in addition to tortuosity, nanoparticles can inhibit chain mobility adding to the reduction in water vapor permeability.

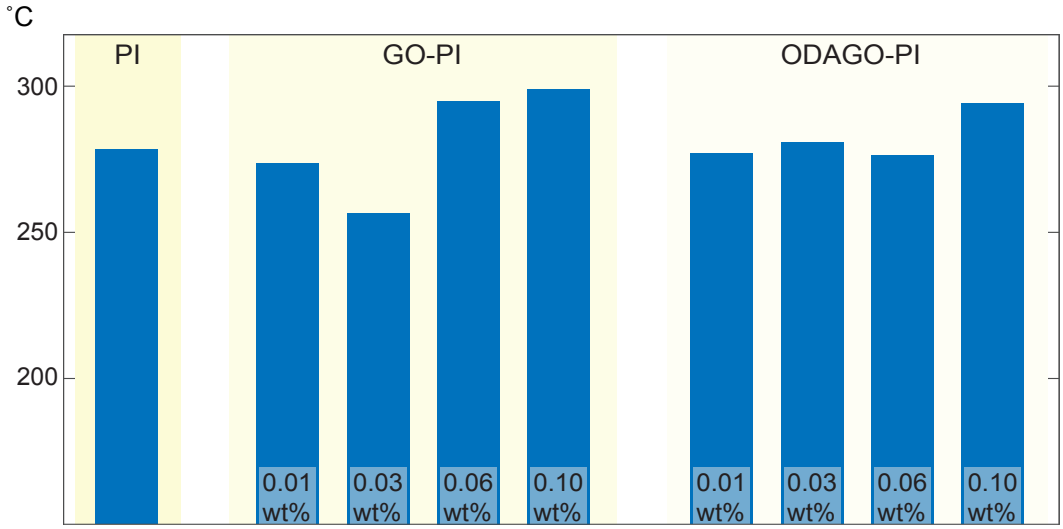

Figure 6-6: Glass transition temperatures (Tg) of PI, GO-PI, and ODAGO-PI measured using differential scanning calorimetry.

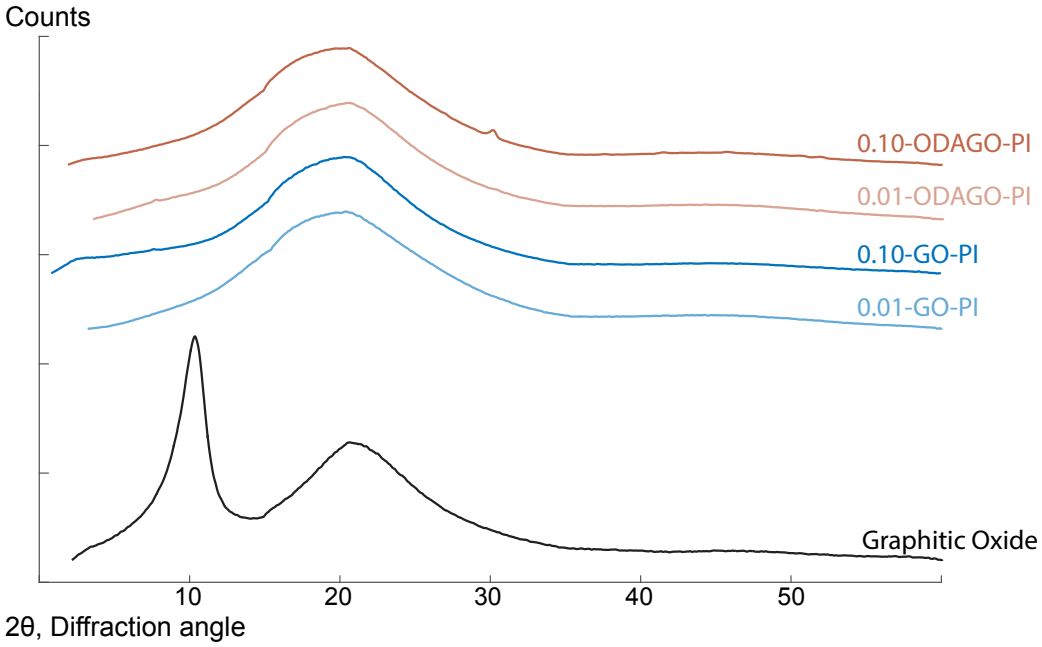

Figure 6-7: Wide anlge X-ray Diffraction, WAXRD, spectra of GO, GO-PI, and ODAGO-PI.

The WXRD pattern, Figure 6-7, for the graphitic oxide stacked GO particles had a peak at 2θ of 11.98° corresponding to a spacing of 7.38 Å, which is in agreement with literature data for stacked GO sheets. The spectra for the ODAGO PI films and the GO-PI films showed only the characteristic amorphous halo, indicating[50, 51] that the ODAGO and GO nano-particles were dispersed as single sheets at these very low loadings.

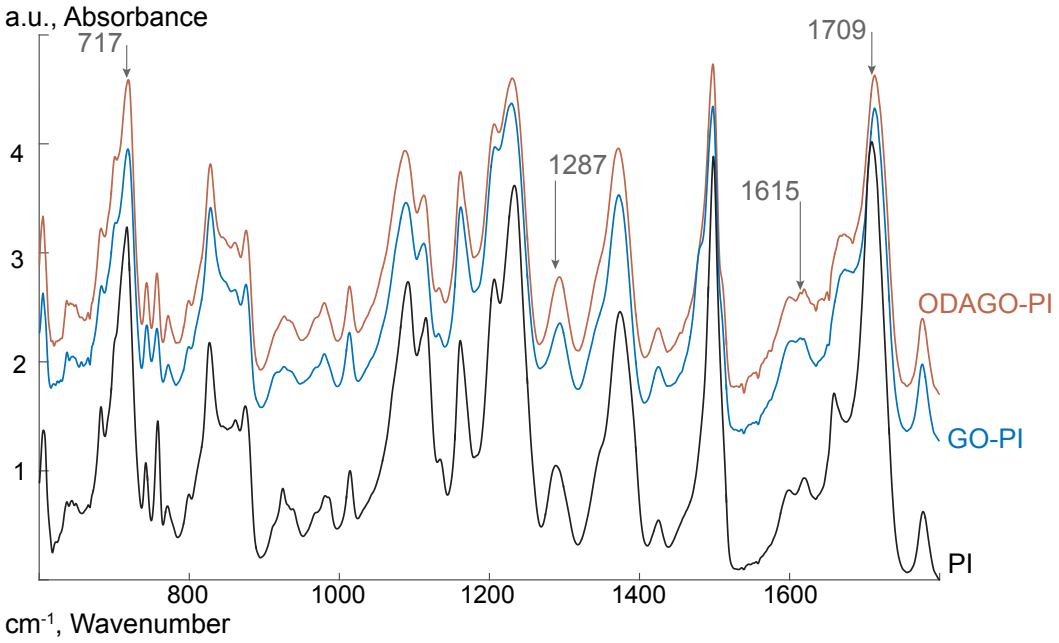

Figure 6-8: Fourier Transform Infrared Spectra of polyimide (PI); graphene oxide loaded PI (GO-PI) at 0.1 wt%; and ODA functionalized graphene oxide loaded PI (ODAGO-PI) at 0.1 wt%.

The magnitude of nanoparticles affecting chain mobility would be expected to be dependent on the intermolecular interaction of the particle's surface chemistry with the chemical structure of the polymer. Thus as another means to detect the effect of the nanoparticles on the polyimide and its resulting water vapor permeability, ATR-FTIR measurements were made on the neat PI film and compared with the GOPI and the ODAGOPI films as seen in Figure 6-8. The objective is to assess detectable interaction of the graphene nanoparticles with the polyimide matrix and differences in the interaction between the ODAGO and the GO nanosheets.

The known 1615–1620 cm^{-1} peak for graphene's sp^2 carbon structure was clearly observed in GO-PI and ODAGO-PI. Several modest shifts in the position of characteristic functional groups were observed and indicate interaction between the nanosheets and the imide bonds. The 717 cm^{-1} imide ring vibration is shifted up to 719 cm^{-1} for the GO-PI and up to 720 cm^{-1} for the ODAGO-PI. The 1287 cm^{-1} C-N imide stretch was shifted from 1287 cm^{-1} for PI to 1294 cm^{-1} for both GO-PI and ODAGO-PI. These results showed that the C-N bond vibrates at a higher frequency in the presence of ODAGO and GO. ODAGO and GO induced a stronger C-N bond. A stronger and stiffer C-N bond indicates that the GO and ODAGO interacts with the imide ring to cause the carbon-nitrogen bond to vibrate at a higher energy and make a more rigid PI chain. The symmetric imide carboxylic oxygen stretch peak increases from 1709 to 1714 cm^{-1} for both the GO-PI and ODAGO-PI, which indicates decreased hydrogen bonding[52, 53].

The neat polyimide hydrogen stretch at 3066 cm^{-1} was slightly down shifted to 3064 cm^{-1} in the GO-PI and up-shifted to 3069 cm^{-1} in the ODAGO-PI, the latter suggesting increased hydrogen interactions between the ODAGO and the PI chain than with GO and the PI chain. Finally, N-H bond stretching at 3480 cm^{-1} was upshifted to 3486 cm^{-1} for both the GO-PI and the ODAGO-PI, indicating hydrogen bond disruption. These results indicate that both the GO nanosheets and the functionalized ODAGO sheets are interacting with the imide ring and strengthening imide bonds in the polyimide. This produces a stiffer chain backbone and less polymer chain mobility. Evidence that ODAGO has a slightly larger effect than does GO on the chain's stiffness and resulting mobility is seen in the ODAGO's versus the GO's effect on the 3066 cm^{-1} shift.

6.3.2 Water Gain Analysis

Seen in Figure 6-9, all GO-PI materials demonstrated less water absorption than the unloaded, neat PI film. Additionally, the functionalized ODAGO-PI had less water absorption than the GO-PI films. When compared with the neat PI 0.01 wt%, ODAGO-PI had half the water absorption; 0.06 wt% ODAGO-PI absorbed a third as much water; and the 0.1 wt% ODAGO-PI absorbed two thirds as much water as the neat system.

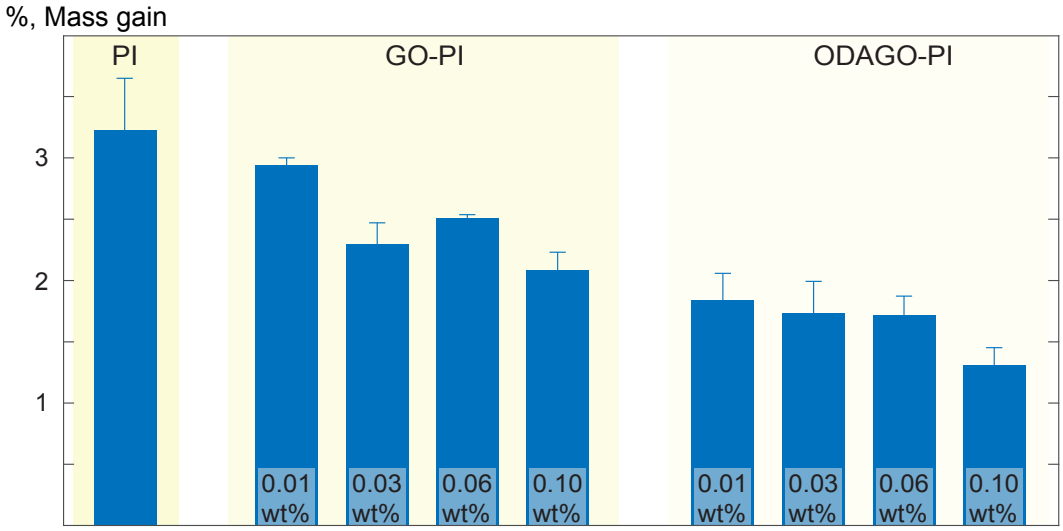

Figure 6-9: Percent water gain after 24 hours immersion in DI water for ODA-GO-PI, GO-PI and neat PI.

The GO-PI system demonstrated only a 10% reduction in water absorption compared to the neat system at 0.01 wt%. At 0.06 wt%, the GO-PI system demonstrated a 20% reduction in water absorption compared to the unloaded film. The 0.1 wt% GO-PI demonstrated a 40% reduction in water absorption compared to the unloaded film. The ODAGO loaded films demonstrate higher resistance to water absorption than films loaded with unmodified GO. Thus reacting GO with ODA is more effective in producing GO nanoparticles that improve the hydrophobic properties of the PI system.

6.4 Mechanical Properties

In Figure 6-10, Young's modulus of the PI film increased with the addition of both ODA-GO and GO nanoparticles. The Young's modulus was most effectively increased by the addition of functionalized ODAGO nanoparticles. At 0.01 wt%, ODAGO-PI had an average Young's modulus of 3.3 GPa, a 45% increase compared to the neat film. At 0.06 wt%, ODAGO-PI film exhibited a Young's modulus of 2.8 GPa, a 22 % increase. At 0.1 wt%, ODAGO-PI increased 82% to a Young's modulus of 4.1 GPa.

The increase in Young's modulus was less in the GO-PI films. At 0.01 wt% GO-PI, Young's modulus was slightly less than neat PI. At 0.03 wt% GO-PI, Young's modulus increased 16% compared to the neat PI. The 0.06 wt% GO-PI gained 11% in the Young's modulus. The 0.1 GO-PI demonstrated an increase in the Young's modulus of 27%.

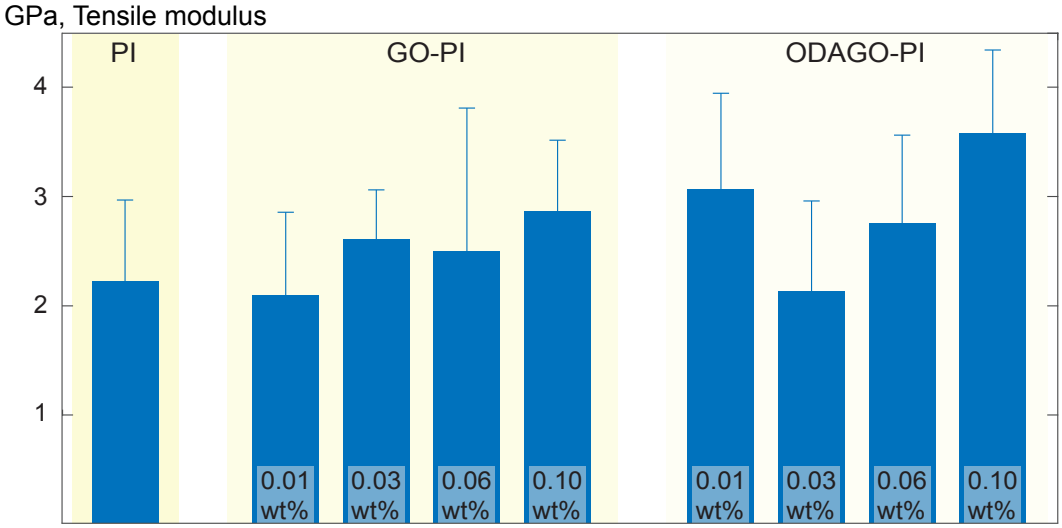

Figure 6-10: Young's modulus of ODA-GO-PI, GO-PI and neat PI films.

At low loadings, the Young's modulus increases for loaded PI are best achieved by using the functionalized nanoparticle, ODAGO. The improved effect of functionalized GO on tensile modulus is attributed to the surface chemistry of the GO being similar to the polymer and thereby increasing particle-polymer intermolecular forces resulting in an increase in chain stiffness. In 2011, Wang et al. [23] found a 6.6-fold improvement in the Young's modulus at 0.3 wt% ODAGO-PI and a 15-fold increase at 3 wt% ODAGO-PI, but using 3 to 300 times more ODAGO.

6.5 Conclusion

Significant improvement in performance properties, most significantly in reduction of water vapor transmission is possible at GO loadings of 0.01 weight percent, a factor of ten lower than the vast majority of GO results in the literature and a factor of over one hundred lower than most gas barrier results using organo-clays.

Functionalizing the surface chemistry of the GO results in up to twice the improvement in gas barrier properties compared with un-functionalized GO-PI. The key is selecting a functionalizing molecule that readily reacts with the epoxy groups on the surface of the GO and which creates strong intermolecular attractive forces between the GO surface and the polymer. The resulting increase in particle polymer interaction is shown to stiffen the chain, reduce its mobility, and

significantly enhance the tortuosity effect.

Water vapor permeability measurements to quantify gas barrier properties, water gain analysis to quantify resistance to fluids, and mechanical tensile tests all show that very low GO loadings of one part per ten thousand improve significantly these performance properties. The largest improvements occurred using ODAGO. The 0.01 wt% ODAGO-PI film demonstrated a large, 10 fold decrease in water vapor permeability. The 0.10 wt% ODAGO-PI film displayed increases of 82 % in the modulus. The 0.06 wt% functionalized GO-ODA PI film showed the largest 73 % decrease in water absorption.

A much larger aspect ratio than observed using AFM measurements was calculated based on the Nielsen equation. This is shown to occur due to the additional effect of ODAGO and GO interacting with the polymer chain backbone, increasing the polyimide chain stiffness and thus decreasing mobility. The magnitude of constrained polyimide mobility diminished with increasing nanoparticle concentration and the effective aspect ratio approached the AFM measured value at the highest concentration. The constrained mobility effect on a per particle basis was strongest at the most dilute concentration. Here, the nanosheet surface is surrounded by polyimide chains increasing particle polymer intermolecular interactions and minimizing particle–particle interaction. The nanoparticle surface interaction with the imide bond of the polyimide, constraining molecular mobility, resulted in the large unexpected reduction in water vapor diffusion, water absorption and an increase in the modulus at a very low loading of

only 0.01 wt%, one part per ten thousand, adding significantly to the nanoparticles' high aspect ratio and high modulus.

6.6 References

[6_1] DUPONT 2015a. Electronic Materials Go to Mars and Beyond. DuPont Electronic Materials.

[6_2] DUPONT 2015b. Kapton Plays Important Role on Rosetta Mission 2015.

[6_3] DUPONT 2013. NASA's Webb Telescope Sunshield made with DuPont Kapton polyimide film.

[6_4] KIM, H., ABDALA, A. A. & MACOSKO, C. W. 2010. Graphene/Polymer Nanocomposites. Macromolecules, 43, 6515-6530.

[6_5] BRODIE, B. C. 1859. On the Atomic Weight of Graphite. Philosophical Transactions of the Royal Society of London, 149, 249-259.

[6_6] HUMMERS JR, W. S. & OFFEMAN, R. E. 1958. Preparation of Graphitic Oxide. 1339.

[6_7] CHEE, W. K., LIM, H. N., HUANG, N. M. & HARRISON, I. 2015. Nanocomposites of graphene/polymers: a review. Rsc Advances, 5, 68014-68051.

[6_8] HU, K. S., KULKARNI, D. D., CHOI, I. & TSUKRUK, V. V. 2014. Graphene-polymer nanocomposites for structural and functional applications. Progress in Polymer Science, 39, 1934-1972.

[6_9] MAHESHKUMAR, K. V., KRISHNAMURTHY, K., SATHISHKUMAR, P.,

SAHOO, S., UDDIN, E., PAL, S. K. & RAJASEKAR, R. 2014. Research Updates on Graphene Oxide-Based Polymeric Nanocomposites. Polymer Composites, 35, 2297-2310.

[6_10] MITTAL, G., DHAND, V., RHEE, K. Y., PARK, S. J. & LEE, W. R. 2015. A review on carbon nanotubes and graphene as fillers in reinforced polymer nanocomposites. Journal of Industrial and Engineering Chemistry, 21, 11-25.

[6_11] MITTAL, V. 2014. Functional Polymer Nanocomposites with Graphene: A Review. Macromolecular Materials and Engineering, 299, 906-931.

[6_12] PAN, L., LIU, Y. T. & XIE, X. M. 2014. Progress in High-performance Graphene/Polymer Nanocomposites - Design of Filler/Matrix Interfacial Interactions and Their Influences. Acta Polymerica Sinica, 724-736.

[6_13] POTTS, J. R., DREYER, D. R., BIELAWSKI, C. W. & RUOFF, R. S. 2011. Graphene-based polymer nanocomposites. Polymer, 52, 5-25.

[6_14] SARAVANAN, N., RAJASEKAR, R., MAHALAKSHMI, S., SATHISHKUMAR, T., SASIKUMAR, K. & SAHOO, S. 2014. Graphene and modified graphene-based polymer nanocomposites - A review. Journal of Reinforced Plastics and Composites, 33, 1158-1170.

[6_15] TJONG, S. C. 2013. Recent progress in the development and properties of novel metal matrix nanocomposites reinforced with carbon nanotubes and graphene nanosheets. Materials Science & Engineering R-Reports, 74, 281-

350.

[6_16] YOO, B. M., SHIN, H. J., YOON, H. W. & PARK, H. B. 2014. Graphene and Graphene Oxide and Their Uses in Barrier Polymers. Journal of Applied Polymer Science, 131, 39628-39651.

[6_17] ZHANG, L., WU, J. T. & JIANG, L. 2014. Graphene and Its Polymer Nanocomposites. Progress in Chemistry, 26, 560-571.

[6_18] SHI, H., LI, Y., GUO, T. & SHI, H. 2012. In-situ preparation of transparent polyimide nanocomposite with a small load of graphene oxide. Journal of Applied Polymer Science, 128, 3163-3169.

[6_19] ZHU, J., LIM, J., LEE, C.-H., JOH, H.-I., KIM, H. C., PARK, B., YOU, N.-H. & LEE, S. 2014. Multifunctional polyimide/graphene oxide composites via in situ polymerization. Journal of Applied Polymer Science, 131, 40177-40184.

[6_20] PARK, O.-K., KIM, S.-G., YOU, N.-H., KU, B.-C., HUI, D. & LEE, J. H. 2014a. Synthesis and properties of iodo functionalized graphene oxide/polyimide nanocomposites. Composites Part B, 56, 365-371.

[6_21] CHANG, K. C. 2014. Advanced anticorrosive coatings prepared from electroactive polyimide/graphene nanocomposites with synergistic effects of redox catalytic capability and gas barrier properties. Express Polymer Letters, 8, 243-255.

[6_22] HEO, C. & CHANG, J.-H. 2013. Polyimide nanocomposites based on

functionalized graphene sheets: Morphologies, thermal properties, and electrical and thermal conductivities. Solid State Sciences, 24, 6-14.

[6_23] WANG, J.-Y., YANG, S.-Y., HUANG, Y.-L., TIEN, H.-W., CHIN, W.-K. & MA, C.-C. M. 2011. Preparation and properties of graphene oxide/polyimide composite films with low dielectric constant and ultrahigh strength via in situ polymerization. Journal of Materials Chemistry, 21, 13569-13575.

[6_24] TSENG, I. H., LIAO, Y. F., CHIANG, J. C. & TSAI, M. H. 2012. Transparent polyimide/graphene oxide nanocomposite with improved moisture barrier property. Materials Chemistry and Physics, 136, 247-253.

[6_25] QIAN, Y., WU, H. F., YUAN, D. Z., LI, X., YU, W. T. & WANG, C. Y. 2015. In situ polymerization of polyimide-based nanocomposites via covalent incorporation of functionalized graphene nanosheets for enhancing mechanical, thermal, and electrical properties. Journal of Applied Polymer Science, 132.

[6_26] WANG, C. Y., LAN, Y. F., YU, W. T., LI, X., QIAN, Y. & LIU, H. S. 2016. Preparation of amino-functionalized graphene oxide/polyimide composite films with improved mechanical, thermal and hydrophobic properties. Applied Surface Science, 362, 11-19.

[6_27] NAEBE, M., WANG, J., AMINI, A., KHAYYAM, H., HAMEED, N., LI, L. H., CHEN, Y. & FOX, B. 2014. Mechanical Property and Structure of Covalent Functionalised Graphene/Epoxy Nanocomposites. Scientific Reports, 4, 1-7.

[6_28] PARK, Y. T., QIAN, Y., CHAN, C., SUH, T., NEJHAD, M. G., MACOSKO, C. W. & STEIN, A. 2014b. Epoxy Toughening with Low Graphene Loading. Advanced Functional Materials, 25, 575-585.

[6_29] SHEN, B., ZHAI, W., TAO, M., LU, D. & ZHENG, W. 2013. Chemical functionalization of graphene oxide toward the tailoring of the interface in polymer composites. Composites Science and Technology, 77, 87-94.

[6_30] WAN, Y.-J., TANG, L.-C., GONG, L.-X., YAN, D., LI, Y.-B., WU, L.-B., JIANG, J.-X. & LAI, G.-Q. 2014. Grafting of epoxy chains onto graphene oxide for epoxy composites with improved mechanical and thermal properties. Carbon, 69, 467-480.

[6_31] LIM, J., YEO, H., GOH, M., KU, B. C., KIM, S. G., LEE, H. S., PARK, B. & YOU, N. H. 2015. Grafting of Polyimide onto Chemically-Functionalized Graphene Nanosheets for Mechanically-Strong Barrier Membranes. Chemistry of Materials, 27, 2040-2047.

[6_32] CAO, L., SUN, Q. Q., WANG, H. X., ZHANG, X. X. & SHI, H. F. 2015. Enhanced stress transfer and thermal properties of polyimide composites with covalent functionalized reduced graphene oxide. Composites Part a-Applied Science and Manufacturing, 68, 140-148.

[6_33] GLOVER, A. J., SCHNIEPP, H. C., KRANBUEHL, D. E., CAI, M. & OVERDEEP, K. R. 2011. In SituReduction of Graphene Oxide in Polymers. Macromolecules, 44, 9821-9829.

[6_34] KWON, K. & CHANG, J. H. 2015. Comparison of the properties of polyimide nanocomposites containing three different nanofillers: Organoclay, functionalized graphene, and organoclay/functionalized graphene complex. Journal of Composite Materials, 49, 3031-3044.

[6_35] SOUTHWARD, R. E., BOGGS, C. M., THOMPSON, D. W. & ST CLAIR, A. K. 1998. Synthesis of surface-metallized polyimide films via in situ reduction of (perfluoroalkanoato)silver(I) complexes in a poly(amic acid) precursor. Chemistry of Materials, 10, 1408-1421.

[6_36] ROH, J. Y., MATECKI, M. K., SVOBODA, S. A. & WUSTHOLZ, K. L. 2016. Identifying Pigment Mixtures in Art Using SERS: A Treatment Flowchart Approach. Analytical Chemistry, 88, 2028-2032.

[6_37] KUDIN, K. N., OZBAS, B., SCHNIEPP, H. C., PRUD'HOMME, R. K., AKSAY, I. A. & CAR, R. 2008. Raman Spectra of Graphite Oxide and Functionalized Graphene Sheets. Nano Letters, 8, 36-41.

[6_38] HAIN, M. S., FUKUDA, Y., RAMIREZ, C. R., WINER, B. Y., WINSLOW, S. E., PIKE, R. D. & BEBOUT, D. C. 2014. Staging Bonding between Group 12 Metal Ions and Neutral Selenium Donors: Intermolecular Interactions of Mixed N,Se Donor Ligands and Anions. Crystal Growth & Design, 14, 6497-6507.

[6_39] NEMOURS, E. I. D. P. D. 2015. Summary of Properties for Kapton Polyimide Films [Online]. http://www.dupont.com/content/dam/assets/products-and-services/membranes-films/assets/DEC-Kapton-summary-of-properties.

pdf: DuPont. Available: http://www.dupont.com/content/dam/assets/products-and-services/membranes-films/assets/DEC-Kapton-summary-of-properties.pdf [Accessed 12-Oct-2015 2015].

[6_40] PICARD, E., GÉRARD, J. F. & ESPUCHE, E. 2015. Reinforcement of the Gas Barrier Properties of Polyethylene and Polyamide Through the Nanocomposite Approach: Key Factors and Limitations. Oil & Gas Science and Technology – Revue d'IFP Energies nouvelles, 70, 237-249.

[6_41] NIELSEN, L. E. 1967. Models for the Permeability of Filled Polymer Systems. Journal of Macromolecular Science: Part A - Chemistry, 1, 929-942.

[6_42] HE, X. F., YANG, J., ZHU, L. C., WANG, B., SUN, G. P., LV, P. F., PHANG, I. Y. & LIU, T. X. 2006. Morphology and melt rheology of nylon 11/clay nanocomposites. Journal of Applied Polymer Science, 102, 542-549.

[6_43] HOMMINGA, D. S., GODERIS, B., MATHOT, V. B. F. & GROENINCKX, G. 2006. Crystallization behavior of polymer/montmorillonite nanocomposites. Part III. Polyamide-6/montmorillonite nanocomposites, influence of matrix molecular weight, and of montmorillonite type and concentration. Polymer, 47, 1630-1639.

[6_44] KOLESOV, I., KACI, M., LEBEK, W., MILEVA, D., BENHAMIDA, A., FOCKE, W. & ANDROSCH, R. 2013. Crystallization of a polyamide 11/organo-modified montmorillonite nanocomposite at rapid cooling. Colloid and Polymer Science, 291, 2541-2549.

[6_45] MA, Y. L., HU, G. S., REN, X. L. & WANG, B. B. 2007. Non-isothermal crystallization kinetics and melting behaviors of nylon 11/tetrapod-shaped ZnO whisker (T-ZnOw) composites. Materials Science and Engineering a-Structural Materials Properties Microstructure and Processing, 460, 611-618.

[6_46] MILTNER, H. E., VAN ASSCHE, G., POZSGAY, A., PUKANSZKY, B. & VAN MELE, B. 2006. Restricted chain segment mobility in poly(amide) 6/clay nanocomposites evidenced by quasi-isothermal crystallization. Polymer, 47, 826-835.

[6_47] WENG, W. G., CHEN, G. H. & WU, D. J. 2003. Crystallization kinetics and melting behaviors of nylon 6/foliated graphite nanocomposites. Polymer, 44, 8119-8132.

[6_48] ZHANG, Q., YU, M. & FU, Q. 2004. Crystal morphology and crystallization kinetics of polyamide-11/clay nanocomposites. Polymer International, 53, 1941-1949.

[6_49] ZHANG, Y. S., WANG, B. B. & HU, G. S. 2012. Isothermal Crystallization Kinetics and Melting Behavior of Polyamide 11/Silica Nanocomposites Prepared by In Situ Melt Polymerization. Journal of Applied Polymer Science, 123, 273-279.

[6_50] SCHNIEPP, H. C., LI, J.-L., MCALLISTER, M. J., SAI, H., HERRERA-ALONSO, M., ADAMSON, D. H., PRUD'HOMME, R. K., CAR, R., SAVILLE, D. A. & AKSAY, I. A. 2006. supporting information: Functionalized single graphene

sheets derived from splitting graphite oxide. The journal of physical chemistry. B, 110, 8535-9.

[6_51] MCALLISTER, M. J., LI, J.-L., ADAMSON, D. H., SCHNIEPP, H. C., ABDALA, A. A., LIU, J., HERRERA-ALONSO, M., MILIUS, D. L., CAR, R., PRUD'HOMME, R. K. & AKSAY, I. A. 2007. Single Sheet Functionalized Graphene by Oxidation and Thermal Expansion of Graphite. Chemistry of Materials, 19, 4396-4404.

[6_52] MA, X. Y., KANG, C. Q., CHEN, W. H., JIN, R. Z., GUO, H. Q., QIU, X. P. & GAO, L. X. 2016. Effect of Multiple H-Bonding on the Properties of Polyimides Containing the Rigid Rod Groups. Journal of Polymer Science Part a-Polymer Chemistry, 54, 570-581.

[6_53] LI, B. Y., PANG, Y. W., FAN, C., GAO, J., WANG, X., ZHANG, C. L. & LIU, X. Y. 2014. Influence of Hydrogen-Bonding Interaction Introduced by Filled Oligomer on Bulk Properties of Blended Polyimide Films. Journal of Applied Polymer Science, 131, 9.

Chapter 7

Conclusion and Future Directions

Macroscopic properties of polymers and in general all types of materials are innately related to their molecular structure and intermolecular properties. This dissertation offered insight into how the molecular structure, chain properties, and inter-molecular chain interactions within PA11 can be used to explain and predict improved macro level performance properties; and how the addition of graphene oxide nanosheets enhances the performance properties of PA11 and polyimide(ODA-BTDA) through those same intermolecular interactions.

In Chapter 3, it was shown that small organic acids such as acetic, propanoic, and butanoic in water significantly accelerate the rate of degradation due to hydrolysis and reduce the recombination rate. Thereby small organic acids produce a large reduction in the equilibrium molecular weight. Butanoic acid, the weakest of these acids, has the largest effect on the rate of hydrolysis and the largest effect on the reduction in the equilibrium molecular weight.

Small organic acids have a much larger effect than an HCl water environment at the same pH on the rate and extent of degradation. The fundamental molecular basis for this previously unexpected and unreported result is the similarity in structure to the polyamide and the solubility for these acids in their undissociated

state to diffuse into the solid polyamide creating acid concentrations many times that in the aging water-acid environment.

Chapter 4 utilized the small organic acid accelerated aging of Chapter 3 to decouple the effects of moleculer weight and molecular crystallinity properties affecting the ultimate strain macroscopic property of PA11. In water aging the approach to embrittlement progresses slowly with increasing crystallinity once degraded to the constant equilibrium molecular weight. Here M_m governs the ductility until the equilibrium M_m is reached. When PA11 has reached the equilibrium M_m, the brittleness of the PA11 progresses with increasing crystallinity due to annealing.

A M_m range of 35 ±5 kDa for water and 16 ±3 kDa for acid accelerated were the two areas of embrittlement for PA11 seen in this study. For the high crystallinity values of the water aged PA11, ΔH_{fus} of 70-81 J/g, the ultimate strain remains in the ductile to brittle transition below 100 % but greater than 50 %. This semi-ductile characteristic can be attributed to the relatively high M_m of 35 ±5 kDa compared with acid aged PA11 that is ductile down to 18 ±3 kDa with ΔH_{fus}, 58 J/g. Acid aged PA11 becomes brittle with less than 50 % ultimate strain and is attributed to the combination of the lower M_m, less than 15 kDa, with higher crystallinity, ΔH_{fus} of 68 – 74 J/g.

For PA11, the crystallinity (ΔH_{fus}) and M_m measurements are needed to monitor and predict, based on the aging experiments, the conditions for the onset of the

ductile to brittle transition and when embrittlement occurs. The proposed model based on the three aging experiments can be used to predict the ultimate strain of PA11 during aging and during in-situ use in the field, by measuring both the crystallinity and molecular weight.

Chapter 5 showed the results of a study to use graphene oxide (GO) to improve the degradation of PA11 and thereby retain the performance properties. A concentration of 0.1 wt% GO in PA11 produced a 50 % increase over PA11's equilibrium molecular weight when aged in water at 100 and 120 ˚C, respectively. No improvement was observed in the 0.5 wt% GO-PA11 due to GO agglomeration. A similar higher equilibrium molecular weight occurs in the plasticized commercial Besno P40 grade of PA11. Fitting the previously reported kinetic model to aging results showed an increase in equilibrium molecular weight, when the GO particles were well dispersed. This was due to a reduction in the model's hydrolytic rate constant relative that for re-polymerization.

GO-PA11's decreased ability to crystallize showed that the presence of GO decreased molecular mobility within the nano-particle polymer system. Based on the heat of fusion, both as prepared nanocomposites decreased the amount of PA11 crystallinity slightly. Additionally, the heat of fusion for all three aged materials were nearly comparable after the second heat suggesting that there was no affect upon crystallinity. There is a big effect for the aged samples. On aging at both 100 ˚C and 120 ˚C, the GO-PA11 had significantly less crystallinity demonstrating a reduction in the rate of annealing. After heating above the melting

temperature and cooling, the GO again inhibited the rate of crystallization, but the materials were nearly comparable suggesting no effect on the crystallinity. The decrease in the annealing rate of crystallization in the aged samples is attributed to GO's large immobile nano thickness sheet structure, which inhibited chain mobility within the polymer nanocomposite.

ATR-FTIR spectra showed that the graphene oxide's surface C=O groups hydrogen bond with the polyamide's N-H groups. This interaction further inhibits polymer mobility.

In summary, these two factors, the large immobile nano thin GO sheets and the intermolecular interaction between the GO's surface C=O groups with the polyamide's N-H groups significantly reduce the mobility in the GO-polymer resulting in a reduction in the rate of crystallization and most importantly the rate of degradation by hydrolysis.

Chapter 6 expanded upon the performance improvememts that small amounts of GO can have on performance properties based on amide bond interactions at very low loadings down to 0.01 wt% in polyimide. Significant improvement in performance properties, most significantly in reduction of water vapor transmission is possible at GO loadings of 0.01 weight percent, a factor of ten lower than the vast majority of GO results in the literature and a factor of over one hundred lower than most gas barrier results using organo-clays.

Functionalizing the surface chemistry of the GO results in up to twice the improvement in gas barrier properties compared with un-functionalized GO-PI. The key is selecting a functionalizing molecule that readily reacts with the epoxy groups on the surface of the GO and which creates strong intermolecular attractive forces between the GO surface and the polymer. The resulting increase in particle polymer interaction is shown to stiffen the chain, reduce its mobility, and significantly enhance the tortuosity effect.

Water vapor permeability measurements to quantify gas barrier properties, water gain analysis to quantify resistance to fluids, and mechanical tensile tests all show that very low GO loadings of one part per ten thousand improve significantly these performance properties. The largest improvements occurred using ODAGO. The 0.01 wt% ODAGO-PI film demonstrated a large, 10 fold decrease in water vapor permeability. The 0.10 wt% ODAGO-PI film displayed increases of 82 % in the modulus. The 0.06% functionalized GO-ODA PI film showed the largest 73 % decrease in water absorption.

A much larger aspect ratio than observed using AFM measurements was calculated based on the Nielsen equation. This is shown to occur due to the additional effect of ODAGO and GO interacting with the polymer chain backbone, increasing the polyimide chain stiffness and thus decreasing mobility. The magnitude of constrained polyimide mobility diminished with increasing nanoparticle concentration and the effective aspect ratio approached the AFM measured value at the highest concentration. The constrained mobility effect on

a per particle basis was strongest at the most dilute concentration. Here, the nanosheet surface is surrounded by polyimide chains increasing particle polymer intermolecular interactions and minimizing particle–particle interaction. The nanoparticle surface interaction with the imide bond of the polyimide, constraining molecular mobility, resulted in the large unexpected reduction in water vapor diffusion, water absorption and an increase in the modulus at a very low loading of only 0.01%, one part per ten thousand, adding significantly to the nanoparticles' high aspect ratio and high modulus.

Future research from this body of work may include a detailed study on the crystallinity formation and content due to the presence of GO and on the effect different crystalline forms of PA11 has on performance properties. Overall, a detailed study is needed on how the relationship between ΔH_{fus}, M_m, and ultimate strain can be affected by the addition of GO to the PA11 matrix. The aging behavior of PA11 loaded with functionalized GO using various functionalization molecules is of interest. The aging behavior of PA11 loaded with GO made from different graphitic oxide synthesis methods could be explored. Understanding how to decouple possible crosslinking effects on the performance properties of GO-polymer composites from the effects of the GO nanosheet on polymer chain mobility. Each of these interests could be coupled with functionalized GO AFM tip interactions with polyamides and polyimides.

Extending this research to boron nitride nanotubes is a research direction that is currently underway.

VITA

John-Andrew Samuel Hocker was born in Stillwater, Oklahoma. After graduating from Riverheads High School and Shenandoah Valley Regional Governor's School, he entered the College of William and Mary in Williamsburg, VA in 2004. Mr. Hocker received his degree of Bachelor of Science from the College of William and Mary May 2010. In May 2011, Mr. Hocker enrolled in William and Mary's department of Chemistry graduate program and received his Master of Science of Chemistry in May 2012. Also in May 2012, Mr. Hocker enrolled in the College of William and Mary's Applied Science graduate program.

During his enrollment in the Applied Science graduate program, Mr. Hocker was the first author on two published papers, gave two talks and a poster at the 2015 Materials Research Society Fall Meeting and Exhibition. He contributed to the authorship of 3 funded research proposals. During his research, Mr. Hocker mentored 24 students and 6 honors theses.

In September 2014, Mr. Hocker became employed as an Intern at the NASA Langley Research center where he conducts research on flexible thermal protection systems and metal matrix composites using boron nitride nanotubes. He serves as the principal investigator on the novel BNNT metal matrix composite

project. Since joining NASA in 2014, he has submitted 1 patent application, 12 presentations, and a recipient of the NASA Group Achievement Award as part of the BNNT development team and has mentored 9 students during their summer internships.